

# **Selected Problems of High-Resolution Automotive Imaging Radar**



**Yang Xiao**

School of Engineering  
University of Birmingham

This dissertation is submitted for the degree of

*Doctor of Philosophy*

January 2023

**UNIVERSITY OF  
BIRMINGHAM**

**University of Birmingham Research Archive**

**e-theses repository**

This unpublished thesis/dissertation is copyright of the author and/or third parties. The intellectual property rights of the author or third parties in respect of this work are as defined by The Copyright Designs and Patents Act 1988 or as modified by any successor legislation.

Any use made of information contained in this thesis/dissertation must be in accordance with that legislation and must be properly acknowledged. Further distribution or reproduction in any format is prohibited without the permission of the copyright holder.

*I would like to dedicate this thesis to my parents and my lovely  
grandmother.*

## **Abstract**

This thesis aims at two selected problems in the development of high-resolution automotive imaging radar: 1) The feasibility of using sub-THz for the next generation of automotive radar; 2) The development of the physics-based image segmentation approach on the automotive radar imagery.

The wide range of feasibility studies on the use of sub-THz frequencies for automotive radar have been undertaken in the Microwave Integrated Systems Laboratory (MISL) at the University of Birmingham, and the candidate is in charge of the included study on the theoretical modelling and experimental verification of the attenuation through the vehicle infrastructures which is the first part of this thesis. The importance of this work is related to the fact that automotive radar is placed within the car infrastructure. Therefore, it would be a potential show-stopper in the development of this innovation if attenuation within the car bumper or badge is prohibitively high. Both theoretical modelling and experimental measurement are conducted by considering the impact factors on the propagation properties of the sub-THz signal such as the incident angle, frequency, characteristic parameters of materials, and the thicknesses of infrastructure layers. The transmissivity of multilayered structure has been modelled and good agreement with the results of measurements was demonstrated, so that the developed approach can be used in further studies on propagation through car infrastructure. The published results on transmissivity and complex permittivity of automotive paints are valuable for researchers in either field of THz technology or automotive radar.

The image segmentation on automotive radar maps aims at identifying the passable and impassable areas for path planning in autonomous driving. Contrary to traditional radar, radar clutter is regarded as the physical meaningful information, which can deliver valuable feature information for surface characterization, and enable the full scene reconstruction of automotive radar maps. The proposed novel segmentation algorithm is a hybrid method composed of pre-segmentation based on image processing methods, and the region classification using the multivariate Gaussian distribution (MGD) classifier developed based on the statistical distribution feature parameters of radar returns of various areas. Moving target indication (MTI) is implemented for the first time based on frame-to-frame context association. The end-to-end segmentation framework is therefore achieved robustly with good segmentation performance, and automatically without human intervention.

## **Declaration**

I hereby declare that except where specific reference is made to the work of others, the contents of this dissertation are original and have not been submitted in whole or in part for consideration for any other degree or qualification in this, or any other university. This dissertation is my own work and contains nothing which is the outcome of work done in collaboration with others, except as specified in the text and Acknowledgements. This dissertation contains fewer than 65,000 words including appendices, bibliography, footnotes, tables and equations and has fewer than 150 figures.

Yang Xiao

January 2023

## Acknowledgements

Throughout the last three years of Ph.D., I indeed spent an enjoyable and valuable period, which should be the most memorable experience of my whole life. There are so many people and institutions I would like to express my greatest thanks to.

I hereby express my gratitude to the MISL lab, and the school of engineering at the University of Birmingham for providing financial support throughout my Ph.D.

I would like to express my gratitude to my supervisors: Prof. Marina Gashinova and Prof. Mikhail Cherniakov, who give me solid support and kind encouragement all the time. Thanks to them for giving me such a precious chance to work as a Ph.D. candidate in MISL, which is a great place to inspire my interest in academia. Thanks to their careful and professional suggestions which are the wealth for me to strengthen my academic thinking and skills. Thanks to them for always being considerate and understanding the difficulties I faced in the procedure of improving myself. All research works presented in this thesis would not be possible without their abundant knowledge and experience. Being a Dr. with a gene of MISL is such an honorable milestone for me, all the precious characters I learned are priceless for my future- "Be kind, be curious, and be energetic".

As a member of the MISL lab, I appreciate having this opportunity to work in such an international research environment. I would like to express my thanks to all staff of the MISL group. Thanks to my daily supervisors, Dr. Liam Daniel and Dr. Fatemeh Norouzian, who helped me a lot to improve my hands-on ability to do the practical experiment and revise my immature manuscripts with lots of patience. Thanks to Dr.

Edward G. Hoare and Dr. Emidio Marchetti, who helped me to enhance my knowledge of practical experiment operations and gave me valuable suggestions to strengthen my ideas. Thanks to my good friends Ana Stroescu, Anum Ahmed Pirkani, Muge Ozturk Bekar, Shahrzad Minooee Sabery, Xiaofei Ren, Yifan Wang, Yuming Bai, and all the other nice people I meet during my Ph.D. They provide me a great work and life environment. I also would like to say thanks to my good friend from my high school period, Dr. Jinghan Wang, who supports me in the difficult times on the way toward Ph.D. degree.

I would like to express my great appreciation to my viva committee members. Thanks to my external examiners, Dr. Dimitris Tzagkas and Dr. Shahzad Gishkori, for all the efforts to review the thesis and to make the on-site viva happen at the University of Birmingham. Thanks again to Dr. Fatemeh Norouzian for being my chairperson and providing kind support for the viva.

A great thanks to my partner, Roger Zhe Li, for being a considerable listener, a wisdom advisor, a solid supporter, and even a patient “grammar checker”. Thanks for standing by me during the most difficult time of my life. All the memories we experienced keep telling how lucky we are to meet each other at the beginning of our Ph.D., and to grow together during the special period for both of us. Unknowns are always arduous, your strong support enable a better me with lots of energy and confidence to explore a fascinating unknown future.

I also would like to express my warmest thanks to my parents who always love me, believe in me, support me and encourage me. Thanks for raising me with full of warmth and love, for nurturing me to be powerful and brave, for supporting me with all they have. May my father’s soul rest in peace. "I will see the rest of the amazing world which you have not got the chance to see, and love the world you always love."

## Publications

- Xiao Y, Norouzian F, Hoare E G, et al. Modeling and Experiment Verification of Transmissivity of Low-THz Radar Signal Through Vehicle Infrastructure[J]. IEEE Sensors Journal, 2020, 20(15): 8483-8496.
- Xiao Y, Daniel L, Gashinova M. Image segmentation and region classification in automotive high-resolution radar imagery[J]. IEEE Sensors Journal, 2020, 21(5): 6698-6711.
- Xiao Y, Norouzian F, Marchetti E, et al. Transmissivity through automotive bumpers at mm-wave and low-THz frequencies[C]//2019 20th International Radar Symposium (IRS). IEEE, 2019: 1-6.
- Xiao Y, Daniel L, Gashinova M. Feature-based classification for image segmentation in automotive radar based on statistical distribution analysis[C] 2020 IEEE Radar Conference (RadarConf20). IEEE, 2020: 1-6.
- Xiao Y, Daniel L, Gashinova M. The end-to-end segmentation on automotive radar imagery [C] 2021 European Microwave week (EuRAD 2021).
- Daniel L, Xiao Y, Hoare E, et al. Statistical image segmentation and region classification approaches for automotive radar[C]//2020 17th European Radar Conference (EuRAD). IEEE, 2021: 124-127.
- Xiao Y, Daniel L, Gashinova M. Automotive Radar Image Segmentation with Frame Fusion [C]. Accepted by Radar 2022 IET.
- Xiao Y, Cassidy S, Gashinova M. Universal Image Segmentation Framework on High-resolution Automotive Radar Map [C]. Accepted by Radar 2022 IET.

- Xiao Y, Daniel L, Gashinova M. The End-to-End Segmentation on Automotive Radar Imagery with MTI based on Frame-to-Frame Association[J]. In preparation (Intend to submit to IEEE sensors journal).
- Xiao Y, Norouzian F, Gashinova M, et al. Automotive Paint Permittivity Estimation in Low-THz frequency[J]. In preparation (Intend to submit to IEEE sensors journal).

## Oral Presentations

**2022 IET International Radar Conference (Radar 2022 IET)**      *London, UK. Feb. 2022*

Best student paper nominee.

Oral presentation on "Automotive Radar Image Segmentation with Frame Fusion ", and "Universal Image Segmentation Framework on High-resolution Automotive Radar Map".

**18th European Radar Conference (EuRAD 2021)**      *London, UK. Feb. 2022*

Oral presentation on "The end-to-end segmentation on automotive radar imagery".

**2020 IEEE radar conference**      *Florence, Italy. Sep. 2020*

Oral presentation on "Feature-based Classification for Image Segmentation in Automotive Radar Based on Statistical Distribution Analysis".

**International Radar Symposium (IRS) 2019**      *Ulm, Germany. Jun. 2019*

Oral presentation on "Transmissivity through automotive bumpers at mm-wave and low-THz frequencies".

**The Electro Magnetic Systems Interest Group (EMSIG) 2020**      *Virtual conference. Dec. 2020*

Oral presentation on "High resolution radar image segmentation for autonomous cars".

## Poster Presentations

**The Electro Magnetic Systems Interest Group (EMSIG) 2019** *Edinburgh, UK. Jun. 2019*

Poster presentation on complex permittivity measurement of automotive paints at THz

**The Electro Magnetic Systems Interest Group (EMSIG) 2018** *Birmingham, UK. Jun. 2018*

Poster presentation on transmission and reflection property of automotive components at low-THz.

## **Abbreviations**

**AD** Autonomous driving

**ADAS** Advanced driver-assistance systems

**ACC** Adaptive cruise control

**AT** Affine transformation

**BPM** Binary phase modulation

**CP** Complex permittivity

**CNN** Convolution Neural Network

**CF** Current frame

**CR** Corner reflector

**EM** electromagnetic

**E2E** End-to-end

**FCM** Fuzzy c-means

**FSEM** Fuzzy stochastic estimation maximization

**FMCW** Frequency-modulation continues-wave

**FoV** Field of view

**F2FA** Frame to frame association

**GR** General region

**GPS** Global positioning system

**HM** Hybrid method

**IMU** Inertial measurement unit

**IF** Intermediate frequency

**JSC** Jaccard similarity coefficient

**LR** Large region

**LRR** Long-range radar

**MRR** Mid-range radar

**MIMO** Multiple input multiple output

**MGD** Multi-variate Gaussian distribution

**MTI** Moving targets indication

**NRCS** Normalized radar cross section

**NRMSE** Normalized root mean square error

**OBIA** Object-based image analysis

**PNA** Programmable network analyzers

**PRI** Pulse repetition interval

**PC** Polycarbonate

**PP** Polypropylene

**PET** Polyethylene terephthalate

**PUR** Polyurethane

**PPI** Plan position indicator

**PF** Previous frame

**QS** Quasi space

**ROI** Regions of interest

**RF** Radio frequency

**RCS** Radar cross section

**RX** Receiver

**RMSE** Root mean square error

**SNR** Signal-to-noise ratio

**SAR** Synthetic aperture radar

**SFR** Stepped frequency radar

**SR** Small region

**SRR** Short-range radar

**SIMO** Single input multiple output

**TX** Transmitter

**TDM** Time division multiplexing

**TDS** Time domain spectroscopy

**UWB** Ultra-wide band

**VNA** Vector network analyzer

**WT** Watershed transformation

# Table of contents

<b>List of figures</b>	<b>xix</b>
<b>List of tables</b>	<b>xxvii</b>
<b>1 Introduction</b>	<b>1</b>
1.1 Background of Radar System . . . . .	1
1.1.1 Radar Fundamentals . . . . .	1
1.1.2 Radar Equations . . . . .	3
1.2 Background of Automotive Radar . . . . .	6
1.2.1 Basics of FMCW . . . . .	9
1.2.2 Basics of MIMO . . . . .	12
1.3 Motivations of the Research Work in the Thesis . . . . .	16
1.3.1 Sub-THz Automotive Radar . . . . .	16
1.3.2 Image Segmentation on Automotive Radar Image . . . . .	21
1.4 Outline of Work and Structure of Thesis . . . . .	22
<b>I Study on Transmissivity and Reflectivity of Low-THz signal through Vehicle Infrastructure.</b>	<b>24</b>
<b>2 Modeling and Experiment Verification of Transmissivity of Low-THz Radar Signal Through Vehicle Infrastructure</b>	<b>25</b>
2.1 Introduction . . . . .	26

---

2.2	Analytical Model . . . . .	27
2.2.1	Fresnel Equations . . . . .	27
2.2.2	Theoretical Model of Transmission of Multi-Layer Structure Medium: "General Approach" . . . . .	29
2.2.3	Modeling Results of the Transmissivity Through Headlight-Cover: Single Layer Case . . . . .	32
2.2.4	Modeling Results of the Transmissivity Through Bumper. Multi-Layer Case . . . . .	35
2.3	Measurement Methodology . . . . .	39
2.4	Experimental Results . . . . .	42
2.4.1	Measured Transmissivity through Automotive Bumper and Headlight Cover . . . . .	44
2.4.2	Measured Transmissivity through PC Sheets with Different Thicknesses . . . . .	50
2.5	Conclusions . . . . .	52
<b>3</b>	<b>Automotive Paint Permittivity Estimation in Low-THz frequency</b>	<b>54</b>
3.1	Introduction . . . . .	55
3.2	Theoretical Model . . . . .	55
3.3	Experimental Methodology . . . . .	56
3.3.1	Automotive Paint Sample Structure . . . . .	56
3.3.2	Experimental Setup using THz-TDS . . . . .	58
3.3.3	Estimation of Complex Permittivity and Thickness by using TDS Setup . . . . .	60
3.3.4	Experimental Setup using THz-VNA . . . . .	62
3.3.5	Estimation of Complex Permittivity by using VNA Setup . . . . .	64
3.4	Experimental Results . . . . .	65
3.4.1	Measured Dielectric Properties of Automotive Paints . . . . .	65

---

3.5 Application to Practical Multi-layer Automotive Structures . . . . .	71
3.6 Conclusions . . . . .	73
<b>4 Contributions on Part I</b>	<b>74</b>

## **II Image Segmentation Technique in Automotive Radar Field 76**

<b>5 Image Segmentation and Region Classification in Automotive High-Resolution Radar Imagery</b>	<b>77</b>
5.1 Introduction . . . . .	78
5.2 Automotive Radar Image Data Collection . . . . .	81
5.2.1 Radar System, Image Formation and Dataset . . . . .	81
5.2.2 Radar Image Composition and Pre-processing . . . . .	83
5.2.3 Image Format and Data Labelling . . . . .	88
5.3 Region Statistical Properties and Feature Extraction . . . . .	89
5.3.1 Methodology for Extracting Distribution Feature . . . . .	91
5.3.2 Distribution Fitting to Region Intensity Statistics . . . . .	92
5.3.3 Distribution Fitting to Uncalibrated and Calibrated Region Power Statistics . . . . .	96
5.4 Classification Based on Statistical Distribution Features . . . . .	99
5.4.1 Classification Algorithm Based on MGD Model . . . . .	99
5.4.2 Estimation of Classification Performance . . . . .	102
5.5 Automatic Segmentation of Radar Imagery . . . . .	105
5.5.1 Image Pre-segmentation Using the Watershed Transform . . .	106
5.5.2 Region Merging Using MGD-based Classification Method .	107
5.5.3 Results of Automatic Segmentation of Automotive Radar Images	109
5.6 Conclusions . . . . .	113

---

<b>6 The End-to-End Segmentation on Automotive Radar Imagery with MTI based on Frame-to-Frame Association</b>	<b>115</b>
6.1 Introduction . . . . .	116
6.2 B-scope Radar Map Dataset . . . . .	117
6.2.1 B-scope Radar Map . . . . .	117
6.2.2 Estimation of Maximum Segmentation/Classification range. .	120
6.3 Single Frame Segmentation of the E2E Segmentation . . . . .	125
6.3.1 Step 1-Segmentation of Areas with High Power Return . . . .	126
6.3.2 Step 2-Segmentation of Remaining Low Contrast Background	129
6.4 Frame-to-frame Association . . . . .	130
6.4.1 Methodology of F2FA . . . . .	131
6.4.2 MTI using F2FA . . . . .	136
6.4.3 Segmentation Promotion based on F2FA . . . . .	140
6.5 Results of the End-to-end Segmentation . . . . .	142
6.5.1 Improvement of Segmentation Performance after using the End-to-end Segmentation Algorithm. . . . .	142
6.5.2 Analysis on the Results after MTI based on F2FA. . . . .	145
6.6 Conclusions . . . . .	147
<b>7 Contributions of Part II</b>	<b>149</b>
<b>8 Future Work</b>	<b>151</b>
<b>References</b>	<b>154</b>

# List of figures

1.1	Block diagram of typical radar system. . . . .	2
1.2	35 GHz automotive radar built by AEG-Telefunken 1974 [1]. . . . .	6
1.3	24 GHz CWS system built by EATONVORAD, 1996 [2]. . . . .	7
1.4	Applications of automotive distance sensors [3]. . . . .	8
1.5	Block diagram of FMCW radar operates at 77 GHz. . . . .	9
1.6	Waveform of FMCW radar system. . . . .	10
1.7	Angle estimation using two RX antennas [4]. . . . .	12
1.8	The phased array of SIMO configuration of $1\text{TX} \times 8\text{RX}$ [4]. . . . .	13
1.9	The phased array of MIMO configuration of $2\text{TX} \times 4\text{RX}$ [4]. . . . .	13
1.10	Example of 2-dimensional MIMO array and corresponding virtual antenna configuration. . . . .	14
1.11	Example of TDM-MIMO with two TXs. . . . .	14
1.12	Example of spatially encoded BPM-MIMO with two TXs. . . . .	15
1.13	Layout of potential automotive radar installation. . . . .	18
2.1	The boundary conditions when signal strikes at an interface. . . . .	28
2.2	The electric field in the propagation process through a multi-layer sample. . . . .	29
2.3	Simulated transmissivity as a function of incident angle (a) and thickness (b) at 77 GHz, 300 GHz and 670 GHz. . . . .	33
2.4	Simulated reflectivity as a function of incident angle (a) and thickness (b) at 77 GHz, 300 GHz and 670 GHz. . . . .	34

---

2.5	Illustration of the interference between the signals reflected by both boundaries of the medium of thickness equal to integer multiple of the half-wavelength. . . . .	35
2.6	Sketch of four-layer bumper and the range of the thickness for each layer. . . . .	36
2.7	Automotive bumpers with solid paint, metallic paint and pearlescent paint used for the experiments. . . . .	37
2.8	The simulated transmissivity (a) and reflectivity (b) of four-layer bumper with solid, metallic and pearlescent paint at 77 GHz. . . . .	38
2.9	The simulated transmissivity (a) and reflectivity (b) of four-layer bumper with solid, metallic and pearlescent paint at 300 GHz. . . . .	38
2.10	The simulated transmissivity (a) and reflectivity (b) of four-layer bumper with different kinds of paint at 670 GHz. . . . .	39
2.11	(a) The experimental setup for measuring transmissivity (the radar system shown in the setup is 670 GHz SFR); (b) Schematic diagram of the measurement setup. . . . .	40
2.12	The deviations between the simulated and measured transmissivities of sample “A” versus the possible range of real and imaginary part of permittivity at (a) 77 GHz, (b) 300 GHz and (c) 670 GHz. . . . .	45
2.13	Simulated and measured transmissivities of the automotive components as a function of incident angle using CW signal: Results in the frequency ranges of 77 GHz, 300 GHz and 670 GHz are represented in black, blue and red lines, respectively; (a)-(d) are results for bumper samples with solid paint, (e)-(f) are results for bumpers with metallic paint, (g)-(j) are results for bumpers with pearlescent paint and (k) is the result for headlight-cover. . . . .	46

---

2.14 Simulated and measured transmissivity of sample D and E vs frequency over a specific operational bandwidth: (a) (b) (c) are results for sample D at 77 GHz, 300 GHz and 670 GHz, respectively; (d) (e) and (f) are results for sample E. . . . .	47
2.15 Summary of the measured transmissivity at 0° incidence of the vehicle samples at 77 GHz, 300 GHz and 670 GHz. . . . .	48
2.16 Comparison of the simulated transmissivity of three-layer bumper and the measured transmissivity of sample B and the substrate of sample B. . . . .	49
2.17 Measured and simulated transmissivities through PC sheets with different thicknesses: (a) (b) are results at 300 GHz, and (c) (d) are results at 670 GHz. . . . .	51
2.18 The comparison of simulated and measured results as a function of medium thickness. . . . .	52
3.1 Examples of paint samples (sample A and M in Table 3.1) after drying, which are in the color of solid black and metallic blue. . . . .	57
3.2 (a) Schematic of THz-TDS experimental setup; (b) Experimental TDS setup used for measuring the CP of paints. . . . .	59
3.3 (a) Time-domain signals obtained from the TDS experiment (Electric fields of signals through sample holder and through sample K); (b) Frequency domain signals through sample $S_s(f)$ and through reference $S_r(f)$ . . . . .	60
3.4 (a) The measured $\varepsilon''$ of sample K, and (b) the corresponded QS values. .	61
3.5 Transmission measurement setup using THz-VNA. . . . .	63
3.6 Comparison of the measured transmissivity from VNA and TDS, ( $T_{mea}^{VNA}$ and $T_{mea}^{TDS}$ ), and the calculated transmissivity $T_{cal}$ which is closest to $T_{mea}^{VNA}$ . . . . .	64

---

3.7	Measured CP of solid automotive paints based on THz-TDS and THz-VNA. . . . .	66
3.8	Measured CP of pearlescent automotive paints based on THz-TDS and THz-VNA. . . . .	67
3.9	Measured CP of metallic automotive paints based on THz-TDS and THz-VNA: (a) Results of metallic paints in color of red, white, black, blue and grey; (b) Results for bright gold and silver metallic paints. . . . .	68
3.10	Measured CP of primers in color of white, red and grey and clear coat based on THz-TDS and THz-VNA setups. . . . .	69
3.11	Calclualted (a) transmissivity and (b) reflectivity of automotive paint in three-layer structure. . . . .	71
5.1	Automotive radar image set: (a) The uncalibrated radar image in dB power values, (b) corresponding optical image, (c) calibrated radar image and (d) the color coded labeled radar image. . . . .	82
5.2	(a) the experimental setup for measuring radar system response and propagation loss using a CR, and CR on ground, supported by a mat to prevent blockage by grass; (b) a radar image of the CR. . . . .	84
5.3	(a) Measured loss compared with the free space propagation model; (b) Average loss calculated from the grass and asphalt measurements and polynomial loss fit (The label of x-axis shows both range information and the corresponding grazing angles for comparison). . . . .	85
5.4	Comparison of uncalibrated and calibrated radar range profiles. . . . .	86
5.5	(a) Back scatter coefficient as a function of frequency and range for a rough asphalt surface; (b) resolution cell area as a function of range for experimental radar setup. . . . .	87
5.6	Relationship between raxels of rasterised radar images and radar map (resolution) cells. . . . .	89

5.7	The probability density histogram plots and distribution fits of I and Q components (a)-(h) and $V_{intensity}$ (i)-(l), for the four classes. . . . .	93
5.8	Results of NRMSDs between PDF fits and the density histograms of intensity values extracted from the four class region types. . . . .	94
5.9	The distribution parameters obtained from Weibull distribution fit of $V_{intensity}$ as a function of range gate. . . . .	95
5.10	(a)-(h) Density histograms and PDF fits for uncalibrated (left column) and calibrated (right column) radar map dB-power values. . . . .	96
5.11	NRMSEs of PDF fits to the density histograms of uncalibrated radar power map regions for the four classes. . . . .	97
5.12	The parameters obtained from Weibull distribution fit to uncalibrated $P_{dB}$ (a), and calibrated $P_{dB}$ ; (b) Range values indicate the upper value of a range gate. . . . .	98
5.13	Probability density histograms of extracted statistical parameters and normal PDF fits for “asphalt” class: (a) Weibull shape parameter $\lambda$ ; (b) Weibull scale parameter $k$ . . . . .	100
5.14	Comparison between the generated bi-variate ( $\lambda$ and $k$ -variates) Gaussian PDF for asphalt (colourmap indicates probability density) and the training feature parameter values (blue markers). . . . .	101
5.15	F1-score results obtained from the classification algorithm. (Legend labels F and S indicate results of first and second stages of classification and U and C correspond to the use of uncalibrated and calibrated power data respectively.) . . . . .	103
5.16	F1-score results of classification algorithm for varied amounts of training data, using combined features case $x_t^{(3)}$ . . . . .	104
5.17	Block diagram of the automatic segmentation on automotive radar image based on distribution feature extraction and MGD classification model. . . . .	106

---

5.18 The pre-segmentation results obtained using (a) uncalibrated and (b) calibrated radar images after single application of WT. ('O' indicates an over-segmented region, 'U' an under-segmented one.) . . . . .	107
5.19 (a) Ground truth optical image; (b) calibrated automotive radar image; the manually labeled image (c) and automatically segmented radar image (d). . . . .	109
5.20 The automatically segmented results of four consecutive frames of automotive radar imagery: a-d(1) are the optical images; a-d(2) are the calibrated automotive radar images and a-d(3) are the results of automatic segmentation. (Region colour coding equivalent to Fig. 5.19)	111
6.1 (a) is the PPI radar map; (b) B-scope map of the same size ( $802 \times 199$ ) of radar cells; (c) ground truth - photo. . . . .	118
6.2 The measured average power levels of un-calibrated radar data with respect to range gates and the calibration array utilized for power level calibration. . . . .	121
6.3 (a) The estimated mean NRCSSs of various areas based on the measured return power level. (b) The density histograms of NRCSSs of grass and objects. . . . .	123
6.4 The predicted return power level of various areas and the noise floor hitting ranges. . . . .	124
6.5 The predicted noise floor hitting ranges of various classes as a function of the dynamic range of the radar system. . . . .	124
6.6 Block diagrams of algorithm in Chapter 5 and the E2E segmentation..	125

---

6.7 (a) The result of pre-segmentation based on Canny edge detection; (b) The result after the classification of high-power return regions produced in pre-segmentation; (c) The result after segmentation of the remaining background which is mostly asphalt and shadows; (d) The optical imagery corresponds to the radar detected scene. . . . .	127
6.8 The estimated mean precisions of segmentation results and percentages of unknown areas as function of threshold bias $t_{bias}$ . . . . .	128
6.9 (a) The Weibull scale parameters of various areas extracted from the uncalibrated data; (b) The estimated JSC values over different indexes of threshold arrays obtained based on the validation dataset. . . . .	129
6.10 The overlapping relationship between continuous frames in the scene detection of automotive radar. . . . .	130
6.11 The layout of three kinds of driving scenarios. . . . .	131
6.12 The overlap ratios between CF and PFs versus vehicle velocity (km/h) and frame rate (n/s). (a1)-(a4) are going straight; (b1)-(b4) are cornering under the radius of 10 m; (c1)-(c4) are cornering under the radius of 20 m; (d1)-(d4) are cornering under the radius of 40 m. . . . .	132
6.13 Scene presented in optical imagery (a) and two radar frames of the B-scope radar map (b) PF and (c) CF. The manually selected keypoints and the example of region projection of grass area using AT are shown.	134
6.14 (a) Optical imagery of (b); (b) Manually labeled CF with stationary vehicles; (c) Manually labeled PF with projected region; (d) Optical imagery of (e); (e) Manually labeled CF with moving vehicle; (f) Manually labeled PF with projected region. . . . .	137
6.15 The estimated and measured overlap ratios of moving and stationary objects over CF and PFs. . . . .	138

6.16 (a) The projected regions utilized for the overlap ratio estimation of the stationary object. (b) The projected regions utilized for the overlap ratio estimation of moving objects. (c) The optical imagery of (a). (d) The optical imagery of (b). . . . .	139
6.17 The block diagram of improving segmentation performance by determining the “unknown area” based on F2FA and the corresponding optical imagery. . . . .	141
6.18 First example of segmentation result of the end-to-end segmentation algorithm and comparison with the previous method in Chapter 5. (a) is the PPI radar map; (b) is the corresponding optical imagery. (c) is the input B-scope radar map; (d) is the manually labeled map; (e) is the segmented PPI map obtained from the method in Chapter 5; (f) is the segmented PPI map obtained by the end-to-end segmentation. . . . .	143
6.19 Second example of segmentation results. (The caption representations are the same as Fig. 6.18). . . . .	144
6.20 The segmentation results after the implementation of MTI based on F2FA. 146	

# List of tables

1.1	The characteristics of automotive radars with different range measurement capability. . . . .	9
2.1	Ranges of the relative permittivity of PC at 77 GHz, 300 GHz and 670 GHz. . . . .	33
2.2	CP of materials used in simulation ( $\epsilon_r/\epsilon_i$ ). . . . .	37
2.3	Parameters for 77 GHz, 300 GHz and 670 GHz radar systems. . . . .	41
2.4	Characteristics of automotive samples. The effective permittivity ( $\epsilon_r - j\epsilon_i$ ) and transmissivity at $0^\circ$ ( $T(0^\circ)$ ). PP: Polypropylene; E/P: Ethylene / Propylene; PUR: polyurethane; PC: polycarbonate. . . . .	43
3.1	Classification of automotive paint sample and thickness ( $\mu m$ ). . . . .	57
3.2	The apertures and farfield distances of waveguides in different frequency ranges. . . . .	63
3.3	CPs of paint layers at 79 GHz [5, 6] . . . . .	65
3.4	Summary of the measured CP and the obtained standard deviation from three experiment setups. . . . .	70
5.1	79 GHz FMCW imaging radar parameters. . . . .	81
5.2	Confusion matrix after first stage of classification combined calibrated/uncalibrated features. . . . .	105

5.3	Confusion matrix after second stage of classification combined calibrated/uncalibrated features. . . . .	105
5.4	Example of original p-values and softmax normalized values and their class determination. . . . .	108
5.5	The JSCs of the automatically segmented radar images and the labeled images. . . . .	112
6.1	The feature parameters of the automotive radar system. . . . .	120
6.2	Parameters of automotive radar systems . . . . .	123
6.3	Comparison between previously published JSCs and the updated JSCs of the E2E . . . . .	143

# **Chapter 1**

## **Introduction**

### **1.1 Background of Radar System**

#### **1.1.1 Radar Fundamentals**

Radar, stands for 'RAdio Detection And Ranging', is an instrument that can be used for detecting, ranging, locating and tracking objects [7]. Distinguishing targets from background clutter is a prerequisite for detection, and fine resolutions in range and angle of arrival are critical for mapping the scene by imaging radar. Various parameters determine the resolution of radar system such as the antenna beamwidth, the signal parameters such as pulse width/bandwidth and the pulse repetition interval, and the sensitivity of the receiver. Radar includes major subsystems such as transmitter, antenna, receiver and signal processor. Fig. 1.1 shows the block diagram of the typical radar system.

The electromagnetic (EM) waves are generated by the transmitter and passed to the duplexer which connects to the antenna to radiate into space. The duplexer is a microwave switch utilized to isolate the signal transmission and reception when using the same antenna for both transmitting and receiving. The antenna forms a beam that is mechanically steered in a specific direction. Some of the reflected signals from the

target are captured at the receive antenna and processed by the receiver. At the receiver, the received and the local oscillator signals are mixed to generate the intermediate frequency (IF) signal which is subsequently amplified. The detector removes the carrier from the received signal so that the IF signal can be converted by the analog-digital converter (A/D) for further signal processing [8].

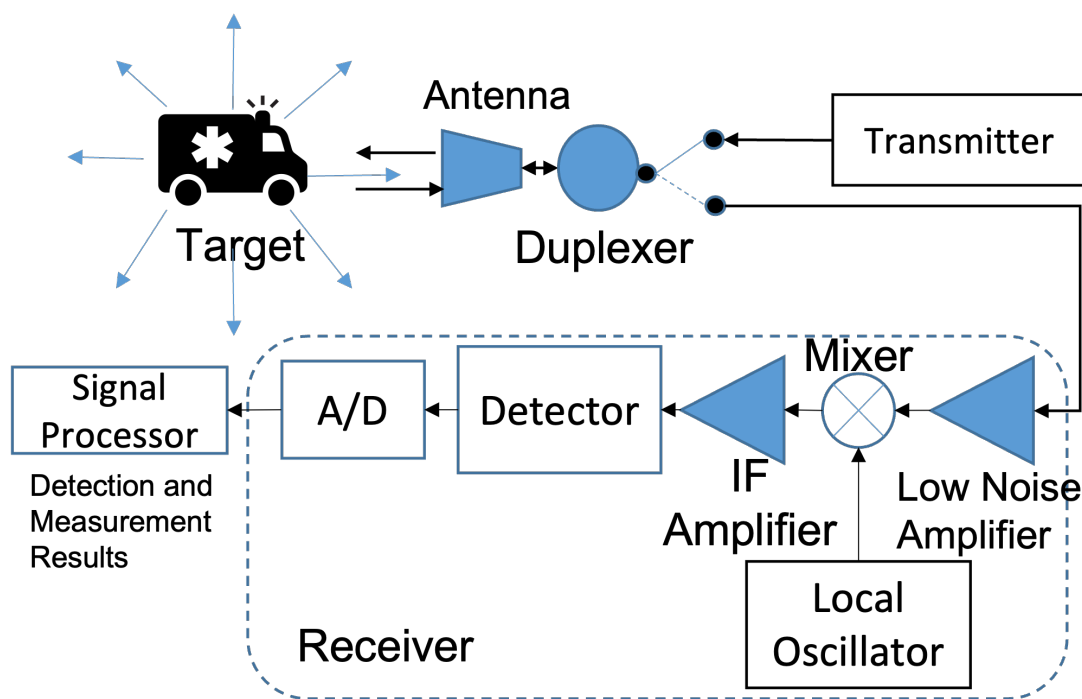


Fig. 1.1 Block diagram of typical radar system.

The details of this block diagram vary across different radar systems as per specific applications, such as air surveillance and space surveillance, surface search and battlefield surveillance, weather monitoring and forecasting, tracking, and guidance as well as astronomy and geodesy. In response to the need of various use cases mentioned above, radar systems cover a wide frequency range from a few MHz up to sub-THz. The general categorizations of radar frequency bands are:

- HF band (3 MHz-30 MHz): over-the-horizon radar, achieves object detection in very long range with low spatial accuracy and resolution;

- VHF and UHF bands (30 MHz-300 MHz and 300 MHz-1000 MHz): long-range detection, line-of-sight surveillance with low to medium resolution and accuracy, free from weather effects;
- L-band (1 GHz-2 GHz): Long-range surveillance with medium resolution and some weather effects;
- S-band (2 GHz-4 GHz): short-range surveillance, long-range tracking with medium accuracy, subject to significant weather effects in snow or heavy rain;
- C-band (4 GHz-8 GHz): short-range surveillance, long-range tracking and guidance with high accuracy, subject to increased weather effects in snow or medium rain;
- X-band (8 GHz-12 GHz): long-range tracking and guidance with high accuracy in clear weather;
- $K_u$ -,  $K$ - and  $K_a$ - bands (12 GHz-18 GHz, 18 GHz-27 GHz and 27 GHz-40 GHz): short range tracking and guidance;
- V-band, W-band, and mm-wave (sub-THz) band (40 GHz-75 GHz, 75 GHz-110 GHz and 110 GHz-1000 GHz): very short-range tracking and guidance.

The research work in this thesis concentrates on the frequency bands of W-band and mm-wave (sub-THz) band, which are the frequency bands used in existing and proposed for future automotive radar, respectively.

### 1.1.2 Radar Equations

Here, a brief introduction of two basic equations of radar systems is given, namely radar range equation and receiver noise estimation equation.

## Radar Range Equation

The radar range equation predicts the maximum detection range of actual radar equipment to satisfactory accuracy.

Assume that the radar signal is radiated by an isotropic radiator, which means the energy propagates uniformly in all directions. The transmitted power is  $P_t$ , and the signal propagates over the range of  $R$ . The power flux density, which indicates the power incident on the interception sphere surface area with a radius of  $R$ , can be represented as:

$$S_u = \frac{P_t}{4\pi R^2} \quad (1.1)$$

When considering the antenna gain of the transmitter,  $G_t$ , which indicates the focusing of the transmitted power in a particular direction, the power flux density is then defined as:

$$S_g = \frac{P_t G_t}{4\pi R^2} \quad (1.2)$$

The target detection depends not only on the power density, but also on how much power is reflected in the direction of the radar. The radar cross section (RCS)  $\sigma$  determines the amount of reflected power from the target. The signal is re-radiated by the target, and the power flux density distributed over the surface area at the receiver antenna can be represented as:

$$S_r = \frac{P_t G_t \sigma}{(4\pi)^2 R^4} \quad (1.3)$$

When considering the effective aperture area of the receiver antenna,  $A_r$ , which is related to the antenna gain of  $G_r$  and the wavelength of signal  $\lambda$  with the function of  $A_r = \frac{G_r \lambda^2}{4\pi}$ , we can give the general representation of the received power of the radar system as:

$$P_r = \frac{P_t G_t A_r \sigma}{(4\pi)^2 R^4} = \frac{P_t G_t G_r \lambda^2 \sigma}{(4\pi)^3 R^4}. \quad (1.4)$$

The classic radar equation for calculating range  $R$  can be represented as

$$R = \sqrt[4]{\frac{P_t G_t G_r \lambda^2 \sigma}{P_r (4\pi)^3}} \quad (1.5)$$

The maximum detection range  $R_{max}$  is determined by  $P_{r_{min}}$  which is the minimum power that can be detected by the receiver:

$$R_{max} = \sqrt[4]{\frac{P_t G_t G_r \lambda^2 \sigma}{P_{r_{min}} (4\pi)^3}} \quad (1.6)$$

### Receiver Noise

The minimum received power of  $P_{r_{min}}$  depends on the noise floor of the receiver,  $N$ , which can be calculated as:

$$N = kT_0BN_f \quad (1.7)$$

where  $k$  is the Boltzmann's constant which equals to  $1.38 \times 10^{-23}$  Joule/K,  $T_0$  is the absolute temperature of the receiver and expressed in K,  $B$  is the bandwidth, and  $N_f$  is the noise factor of the receiver. The quantity of  $kT_0B$  represents the minimum input noise power for an "ideal" receiver. The noise factor is the difference between the noise output of the actual receiver to the noise output of an "ideal" receiver with the same overall gain and bandwidth when the receivers are connected to matched sources at the standard noise temperature of  $T_0$ .

## 1.2 Background of Automotive Radar

Radar has been widely applied as the primary automotive sensor, which is designed to sense the surrounding environment, especially dangerous obstacles such as other vehicles causing potential collisions [9].

Currently used automotive sensors include automotive radar, LiDAR, and camera. The characteristics of different sensors can be discussed as follows: camera is the typical passive sensor which utilizes sunlight and the other light sources for radiation and gathers the emitted or reflected radiation from objects or surrounding areas. Camera can show good object size resolution but poor accuracy of range measurement and significant attenuation in bad weather [10]. Automotive radar and LiDAR are the active sensors, which emit energy to scan objects and areas and then detect and measure the radiation that is reflected or backscattered from the targets. LiDARs cover the wavelength range from 250 nm to 2000 nm as per different applications. They have great accuracy and fast-update rate, but suffer high cost and attenuation when propagating in heavy fog, rain, or snow [11]. Compared with the above two sensors, automotive radar has been identified as the most reliable driver assistance sensor, which can directly measure the range and velocity of objects with mitigated negative influence by the external environment [12].



Fig. 1.2 35 GHz automotive radar built by AEG-Telefunken 1974 [1].

The story of automotive radar starts in the early 1970s, when the idea of using it was proposed to reduce accident rates. Various frequencies were considered in the beginning of the exploration: 35 GHz, 47 GHz, 60 GHz and 94 GHz [13–16]. Germany introduces 77 GHz into automotive radar applications in the early 80s, which has now become the worldwide standard frequency band for long-range automotive radars.

Additionally, the frequency band of 24 GHz is generally utilized for the current application of blind spot detection. The solutions of blind spot detection were proposed by *Dunlop Assoc* in the early 70s using 16 GHz signal[14], and *HE Microwave* in 1995 using the 24 GHz frequency band [17]. The commercially used 24 GHz automotive radar showed up in 1992, when the *EATONVORAD CWS-System* was installed in more than 4000 buses and trucks in the US for collision warning [18]. The amount of accidents decreased significantly after involving automotive radars based on the estimation of safety performance after driving 900 million kilometers.



Fig. 1.3 24 GHz CWS system built by EATONVORAD, 1996 [2].

Nowadays, automotive radar becomes the key automotive sensor to assist the human driver with increasing demands of automotive comfort and safety features in modern vehicle manufacture [19]. Generally, automotive radar can be classified according to the detection range as: long-range radar (LRR, 150 m), mid-range radar (MRR, 80 m) and short-range radar (SRR, 30 m) [20]. Below we list a brief taxonomy of different application scenarios of automotive radar.

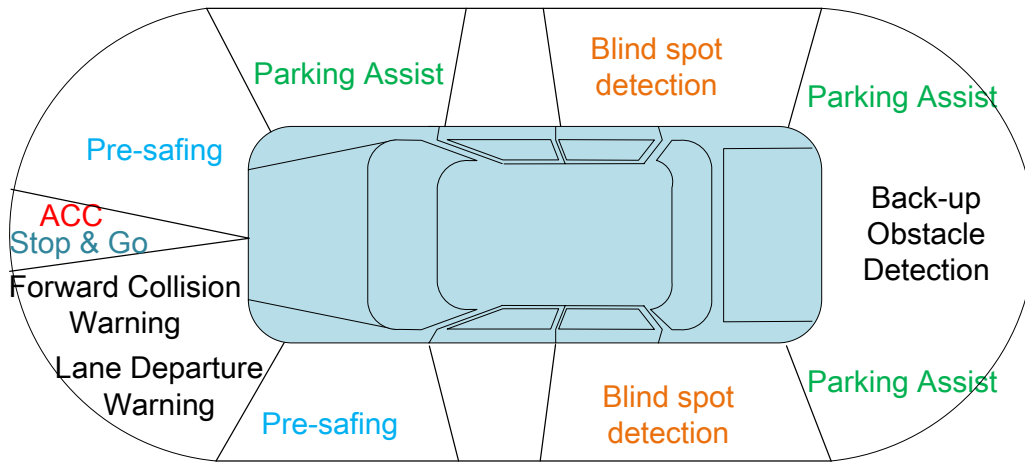


Fig. 1.4 Applications of automotive distance sensors [3].

The applications of LRR include:

- **Adaptive cruise control (ACC) systems**, which can automatically adjust the vehicle speed to maintain distance from the vehicle ahead.

The applications of MRR include:

- **Forward collision warning**, which comprises a visual and audible warning that the driver is too close to the vehicle in front.
- **Blind spot detection** detects the vehicles located to the driver's rear or side.
- **Back-up obstacle detection** detects collision with an object behind the vehicle or with a vehicle approaching from the side.

The applications of SRR include:

- **Lane departure warning** is designed to warn the driver when vehicle begins to move out from the lane.
- **Pre-safing** detects instabilities caused by sudden braking or steering that would upset the balance of a vehicle based on a series of sensors.

Table 1.1 The characteristics of automotive radars with different range measurement capability.

Radar Type	LRR	MRR	SRR
Range (m)	10-250	1-100	0.15-30
Azimuthal field of view (deg.)	$\pm 15^\circ$	$\pm 40^\circ$	$\pm 80^\circ$
Elevation field of view (deg.)	$\pm 5^\circ$	$\pm 5^\circ$	$\pm 10^\circ$

- **Parking assist**

Table 1.1 shows the characteristics of automotive radars [3], and Fig. 1.4 [3, 21] presents the diagram and the respective sensing areas of automotive radar.

In the following, we give a brief introduction to the commonly used technique of automotive radar, namely frequency-modulation continues-wave (FMCW), and multiple input multiple output (MIMO)-the major antenna configuration strategy.

### 1.2.1 Basics of FMCW

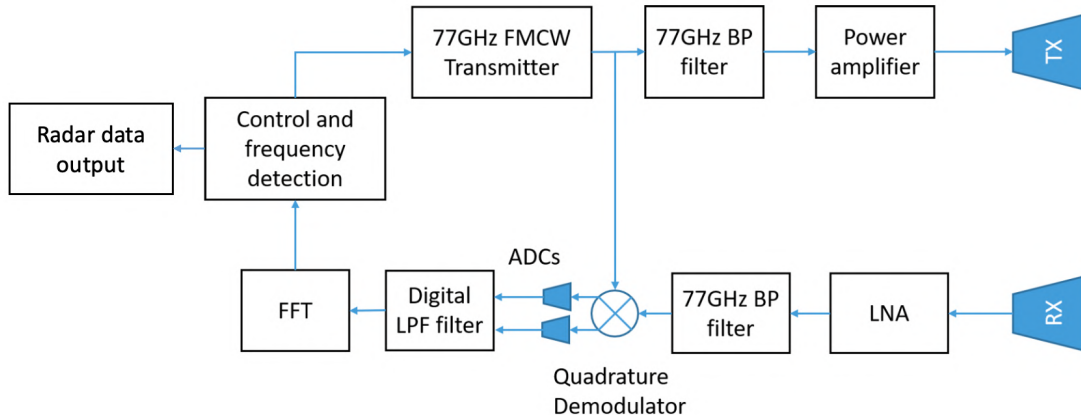


Fig. 1.5 Block diagram of FMCW radar operates at 77 GHz.

FMCW stands for "Frequency-Modulation Continues-Wave", which is a typical radar modulation waveform applied in automotive radar. It achieves the accurate distance and speed measurement by measuring the instant frequency difference between transmitted and reflected signals.

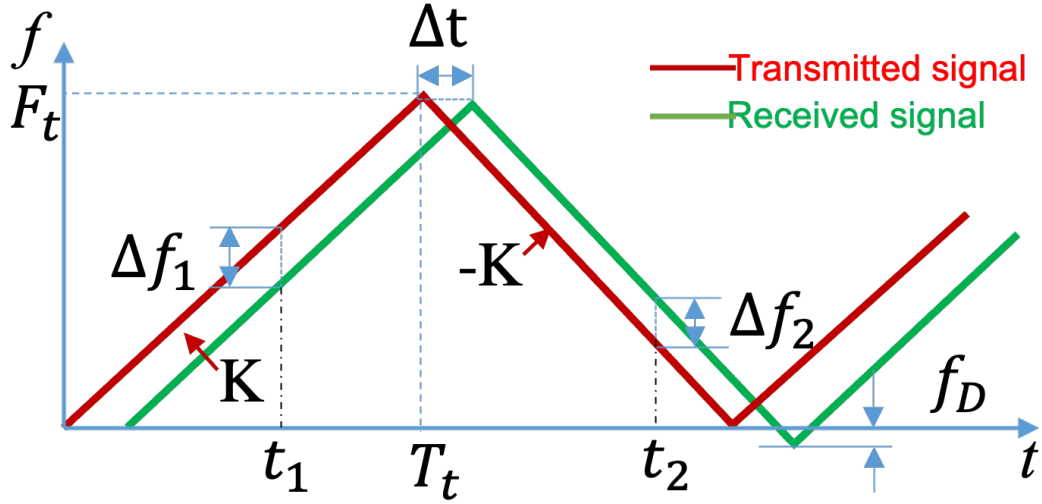


Fig. 1.6 Waveform of FMCW radar system.

The block diagram of an FMCW radar system is shown in Fig. 1.5. The FMCW modulation pattern includes sawtooth modulation, triangular modulation, square-wave modulation and stepped-wave modulation. Here, we would like to discuss the principle of distance and velocity measurement based on the triangular modulation pattern, which is shown in Fig. 1.6. The frequency of the transmitted waveform is swept linearly with the slopes of  $K$  and  $-K$  for up- and down- chirps respectively, where  $K = \frac{F_t}{T_t}$ ,  $F_t$  is the bandwidth, and  $T_t$  is the duration of a half chirp. The transmitted signal can be represented as:

$$s_t = A_t \exp(j\pi(2f_0t + Kt^2)) \quad (1.8)$$

where  $f_0$  is the carrier frequency and  $A_t$  is the magnitude of the transmitted power. The received signal reflected from the target with the time delay of  $\Delta t$  can be represented as:

$$s_r = A_r \exp(j\pi(2f_0(t + \Delta t) + K(t + \Delta t)^2 + \Phi_d)) \quad (1.9)$$

where  $A_r$  is the amplitude of the received signal and  $\Phi_d$  is the Doppler phase shift. At the receiver, the received signal (represented as green line in Fig. 1.6) is mixed with the

transmitted signal and the produced beat signal can be represented as:

$$y = A_t A_r \exp(j\pi(2f_0\Delta t + 2K\Delta t t + K\Delta t^2 + \Phi_d)) \quad (1.10)$$

The term of  $K\Delta t$  is the extracted IF signal for distance measurement. The IF signal is filtered by a low-pass filter with a cut-off frequency of  $f_{LPF}$  which depends on the bandwidth  $F_t$  of the radar system and determines the resolution of range measurement. The distance  $R$  of the target can be determined as:

$$R = \frac{c\Delta t}{2} = \frac{c\Delta f}{2K} \quad (1.11)$$

where  $c$  is the light speed. This equation is applicable for both stationary and moving cases.

When the target is moving, the velocity measurement can be achieved as follow. For the triangular modulation pattern with up- and down- chirps, the IF signal of the up-chirp can be represented as  $\Delta f_1 = K\Delta t + f_D$ , where  $f_D = \frac{2vf_0}{c}$  is the doppler frequency shift and  $v$  is the velocity of the target. The IF signal for the down-chirp is  $\Delta f_2 = K\Delta t - f_D$ . The Doppler frequency shift can be calculated by the measured IF signals at the up- and down- chirps as:

$$f_D = \frac{|\Delta f_1 - \Delta f_2|}{2} \quad (1.12)$$

and the relative velocity of the target can be further calculated as:

$$v = \frac{cf_D}{2f_0} \quad (1.13)$$

### 1.2.2 Basics of MIMO

#### Principle of the MIMO

MIMO, which stands for "Multiple Input Multiple Output", is the key technology to improve the angular resolution/spatial resolution of mm-wave radar. To explain the principle of using MIMO configurations (to improve the angular resolution), we need to start from the angle estimation basics based on phased arrays.

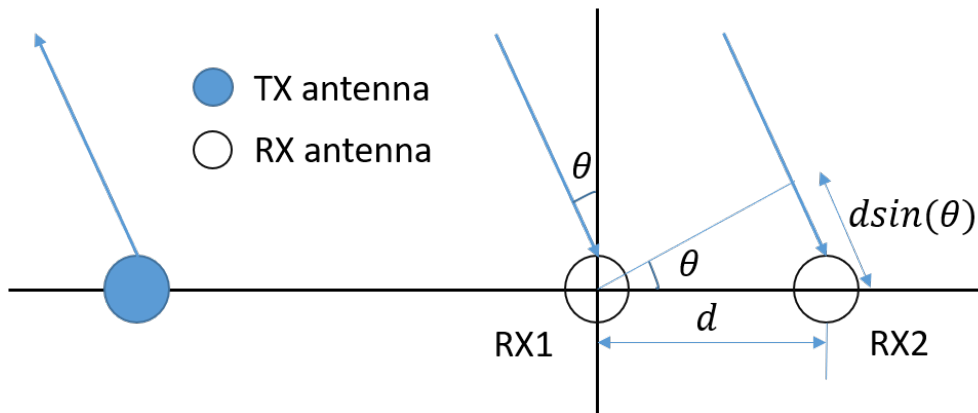


Fig. 1.7 Angle estimation using two RX antennas [4].

Fig. 1.7 shows a Single Input Multiple Output (SIMO) radar system which has one transmitter (TX) and two receivers (RXs) where two RXs have the distance of  $d$ . The signal from TX is reflected by the target and detected by RX1 and RX2. The signal received by RX2 passes a longer distance of  $dsin(\theta)$  than that for the signal to RX1, where  $\theta$  is the angle of arrival of radar signal. The phased array of RX1 and RX2 can be represented as  $[0, \varphi]$ . Here  $\varphi$  is a phase shift between RX1 and RX2 which can be denoted as  $\varphi = (\frac{2\pi}{\lambda})dsin(\theta)$  and  $\lambda$  is the wavelength of radar signals.

The  $\varphi$  is expected in the range of  $(-\pi, \pi)$ , and the field of view (FOV) of this SIMO system is therefore in the range of:  $\theta_{FOV} = \pm \sin^{-1}(\frac{\lambda}{2\pi d})$ . When the antenna distance  $d = \lambda/2$ , the field of view reaches the maximum value of  $\theta_{FOV} = \pm 90deg$ .

The angular resolution depends on  $N$ , the number of RXs, as given in the formula representation of  $\theta_{res} = \frac{\lambda}{Nd\cos(\theta)}$ . The way to improve the angular resolution is to extend the RX phased array. The SIMO configuration of  $1TX \times 8RX$  is given in Fig. 1.8 as the

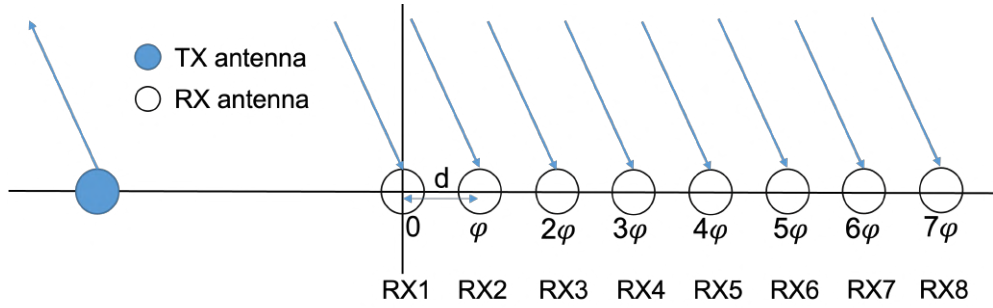


Fig. 1.8 The phased array of SIMO configuration of  $1\text{TX} \times 8\text{RX}$  [4].

example, whose phased array can be represented as  $[0, \varphi, 2\varphi, 3\varphi, 4\varphi, 5\varphi, 6\varphi, 7\varphi]$  and the angular resolution is four times improved compared to that with the configuration in Fig. 1.7. The same angular resolution of  $1\text{TX} \times 8\text{RX}$  SIMO configuration can be achieved by using the  $2\text{TX} \times 4\text{RX}$  MIMO configuration. The utilization of the concept of MIMO can benefit the efficiency of improving the angular resolution.

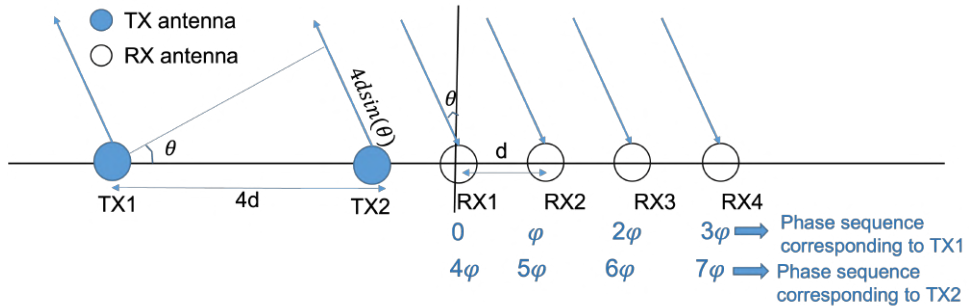


Fig. 1.9 The phased array of MIMO configuration of  $2\text{TX} \times 4\text{RX}$  [4].

The MIMO configuration of  $2\text{TX} \times 4\text{RX}$  is shown in Fig. 1.9. The phase shift sequence produced by signals from TX1 is  $[0, \varphi, 2\varphi, 3\varphi]$ . TX2 has a distance of  $4d$  with TX1 that the signal transmitted by TX2 will go through an additional path length of  $4dsin(\theta)$ . The phase shift sequence of TX2, therefore, shows the additional phase shift of  $4\varphi$  than the phased array of TX1, which can be represented as  $[4\varphi, 5\varphi, 6\varphi, 7\varphi]$ . Hence, the same phase sequence is obtained between the configurations of  $2\text{TX} \times 4\text{RX}$  and  $1\text{TX} \times 8\text{RX}$ , which means that by using the configuration of  $N \text{ TX} \times M \text{ RX}$ , the phased array in the length of  $N \times M$  can be obtained. Fig. 1.10 gives the example of

extending MIMO  $3\text{TX} \times 4\text{RX}$  configuration into a multiple dimensional virtual phased array with the length of 12.

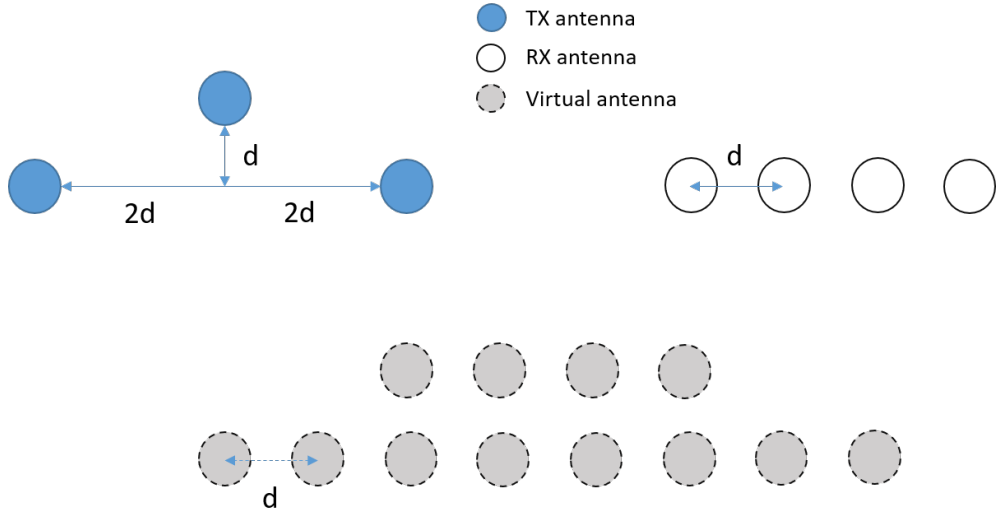


Fig. 1.10 Example of 2-dimensional MIMO array and corresponding virtual antenna configuration.

### Multiplexing Strategies for the MIMO Radar

The configuration of MIMO, which has multiple TX and RX antennas, requires RXs to separate the detected signal from different TXs. Various techniques are considered for achieving this multiplexing on MIMO, such as time division multiplexing (TDM-MIMO) and binary phase modulation (BPM).

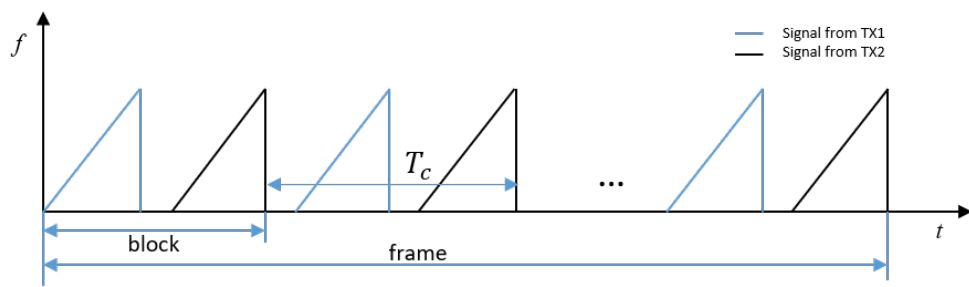


Fig. 1.11 Example of TDM-MIMO with two TXs.

The multiplexing method of TDM is the simplest approach and is widely used to achieve the signal separation of multiple TXs in MIMO. TDM-MIMO scheme

achieves the orthogonality of transmitted signals by time division. Fig. 1.11 shows the transmitted signal sequence of TDM MIMO radar with two TXs as the example, in which one frame consists of multiple blocks and each block has two consecutive transmitted signals from different TXs.

In the signal processing procedure of each RX, 2D-FFT (range-Doppler FFT) is performed on the received signal of each pair of TX and RX for further angle estimation. E.g. the MIMO systems of  $N$  TX  $\times$   $M$  RX produce  $NM$  2D-FFT matrices. Each 2D-FFT matrix corresponds to one pair of virtual antenna. The pre-detection matrix is produced by noncoherently adding the 2D-FFT matrices, and then a detection algorithm identifies peaks in this matrix that correspond to potential objects. For each object, the angle-FFT is performed on the obtained peaks across these multiple 2D-FFTs to achieve the angle of arrival estimation of that object.

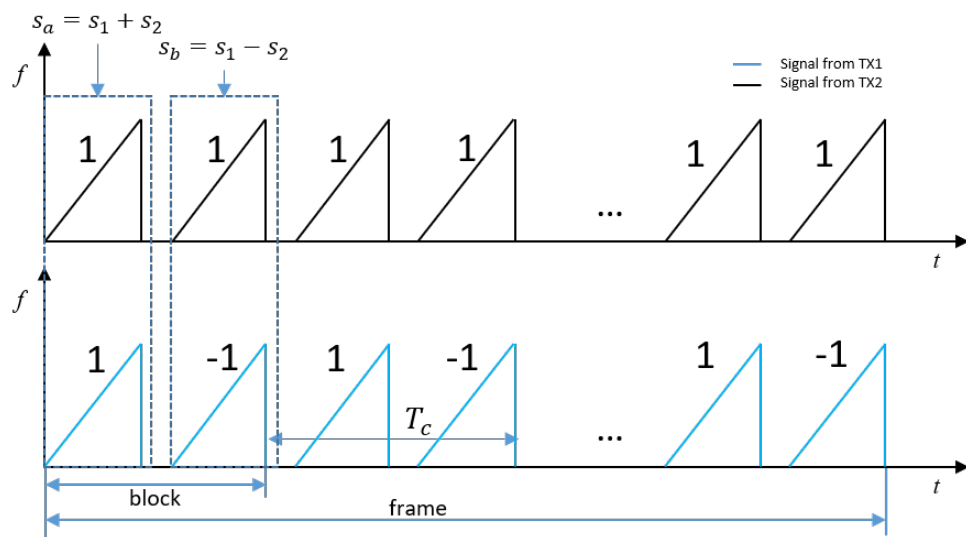


Fig. 1.12 Example of spatially encoded BPM-MIMO with two TXs.

The BPM-MIMO scheme utilizes the more complete transmission capability of radar systems than TDM-MIMO. The TX antennas are all active through the whole time slots, and are spatial encoded using BPM to allow the transmitted signals from different TXs to be sorted at the RXs. The example of signal transmission based on BPM-MIMO scheme with two TXs is shown in Fig. 1.12. For each block, the combined signals of

$s_a = s_1 + s_2$  and  $s_b = s_1 - s_2$  are produced interactively for transmission. Then at the RX, the signal from each TX can be calculated out using  $s_1 = \frac{(s_a+s_b)}{2}$  and  $s_2 = \frac{(s_a-s_b)}{2}$ . The similar method can be extended to the MIMO systems with more TXs.

Advanced automotive radars with the functions of measuring range, angle of arrival, and speed of the objects, as well as high frame update rate, are therefore achieved by implementing MIMO on mm-wave sensors.

## 1.3 Motivations of the Research Work in the Thesis

With the development of automotive radars, the acquired information is no longer restricted to single objects, but also extended to multiple objects, together with the image of the driving environment. Next generation automotive radars tend to obtain high-resolution images to show higher contrast between surfaces and clear edges of detected objects. Researchers also shift the focus from hardware related topics to system topics like identifying the passable regions based on automotive radar images. Research during my Ph.D. period relates to two problems to meet these two demands: 1) the feasibility of improving the image resolution by using sub-THz; and 2) the utilization of full scene information of automotive radar imagery for advanced driver-assistance systems (ADASs) and autonomous driving (AD). In this section, we would like to discuss the motivation of the research work given in Part I and Part II, respectively.

### 1.3.1 Sub-THz Automotive Radar

Currently, three main frequency bands used in automotive radar applications are: 24 GHz, 76-77 GHz and the recently introduced 77-81 GHz ultra-wide band (UWB) [22, 23]. Nevertheless, the increase of automotive radar frequency beyond the current bands can provide benefits [24–30] due to:

- Increase in radar image quality due to higher sensitivity to target texture; (The higher frequency of signal means stronger diffuse reflection when radiated from surfaces, and this is an important feature to differentiate surfaces and enable the segmentation work in Part II.)
- Potential increase in the radar signal bandwidth leading to improvement in range resolution;
- Reduction of antenna dimension when keeping the same angular resolution, alternatively increase in angular resolution having the same antenna dimension;
- Reduction of spectrum occupancy issues as traditional automotive bandwidths become more and more congested.

Therefore, radars operating in the sub-THz frequency bands are being investigated as advanced sensing systems for future automotive sensor application [25, 31].

The THz frequency spectrum spans the frequency range between the infrared and microwave regions, and we will define sub-THz as the frequency band between 100 GHz and 1,000 GHz (1 THz). The generally believed disadvantage of automotive radars operating at these higher frequencies is increased atmospheric attenuation and attenuation through radome material, including additional contamination from water, leaves, ice etc. The attenuation due to sensor cover and contaminants is the subject of this investigation but the latest research shows that the band around 300 GHz is potentially applicable for LRR and definitely for MRR [32–36]. However even higher frequencies could be effectively used as very high resolution automotive sensor for SSR.

The feasibility of sub-THz radar for outdoor applications, such as automotive sensor, requires detailed investigation. The study on sub-THz automotive radar in MISL, University of Birmingham is the brand-new area in radar field. A series of study on propagation property of sub-THz signal have been conducted in MISL, such

as the signal attenuation through contaminated radome and atmosphere in different weather condition [26, 31, 37]. The work shown in this thesis aims at the problem of transmissivity through vehicle infrastructures at sub-THz. The work in Chapter 2 discusses the practical aspects of sub-THz automotive radar incorporated into the infrastructure of a vehicle, and Chapter 3 presents work on complex permittivity (CP) extraction of automotive paint layers.

### Motivation of the Study on Transmissivity of Low-THz Radar Signal through Vehicle Infrastructure

Typically automotive radar is installed behind the car infrastructure by main two reasons (1) protection of the radar and (2) aesthetics of the car. [38, 39]. For instance, sensors for autonomous cruise control (ACC), blind spot detection and rear collision warning are often installed behind the front and rear bumper material.

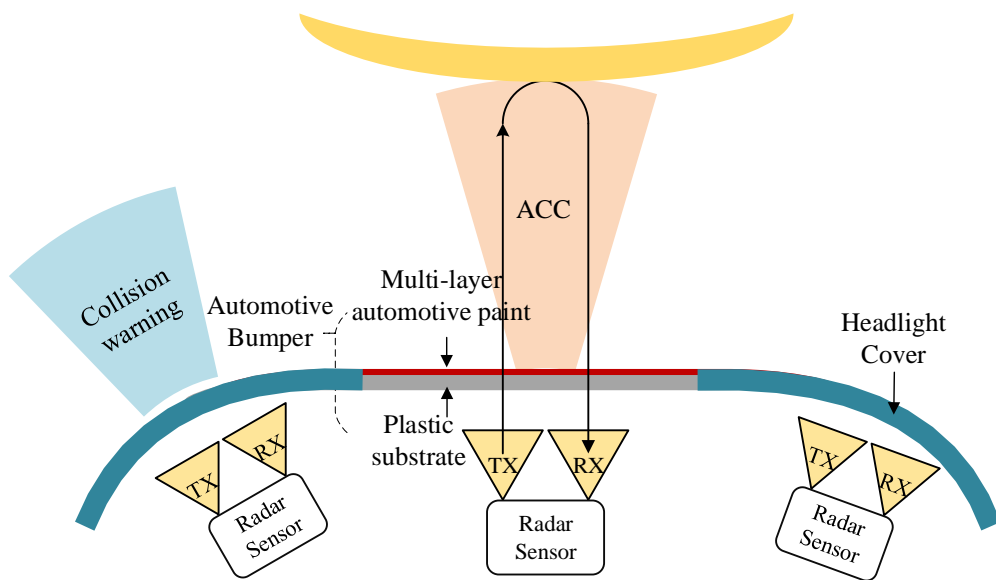


Fig. 1.13 Layout of potential automotive radar installation.

In this research, as shown in Fig. 1.13, we postulate that the radar sensors may be installed behind the bumper or headlight cover in the front of the vehicle. The sensor

signal propagation loss in the path should be included into the radar equation as:

$$P_r = \frac{P_t G_{TX} G_{RX} \sigma \lambda^2 L_{co}}{(4\pi)^3 R^4}, \quad (1.14)$$

where  $L_{co}$  is the miscellaneous propagation losses which includes contributions from atmospheric propagation loss  $L_{ap}$ , the loss due to obscurants,  $L_w$ , attenuation in the sensor cover material,  $L_m$ , including the loss from contaminants on it,  $L_c$ , and any other factors in the path,  $L_{oth}$ . This total loss can be represented as:

$$L_{co} = L_{ap} L_w L_m L_c L_{oth} \quad (1.15)$$

The atmospheric propagation attenuation  $L_{ap}$  is influenced by humidity. According to the reported values in previous works, even in heavy rain, attenuation at 300 GHz does not typically exceed 10 dB/km, which will result in less than 4 dB two-way attenuation loss in the range of 200 m. The detail information of propagation loss in weather-related obscurants are given in works [37, 40, 41]. The parameter  $L_c$  relates to attenuation in various contaminants on the radome such as water, ice, sand, diesel, gasoline and fallen leaves. Attenuation due to such contaminants have been studied and can be found in [26, 33–35, 42].

The attenuation caused by sensor covers  $L_m$  as one of the components of loss  $L_{co}$  is presented and described via the transmissivity of automotive bumpers and headlight covers. The investigation and optimization of the propagation performance of sensor covering material at 76-81 GHz has been studied in several projects, such as the KOKON project [20] and the Radar-on-Chip for Cars (RoCC) project [43–45]. Therefore, conducting this new research at sub-THz frequencies is complimentary, and necessary, for considering sub-THz radar for automotive applications. As a part of the leading sub-THz automotive radar research in MISL group at University of Birmingham, we are the first of studying the sensor cover attenuation at sub-THz frequency.

The theory in this part of research is based on Fresnel's equation and transmission line theory, which are commonly used in electromagnetic wave analysis [46]. However, utilizing this theory to estimate the performance of particular automotive component materials for sub-THz automotive radar applications has not been reported before.

The main task of this part of research is to establish an experimentally verified mathematical model of the transmission and reflection performance of potential automotive radar covers at sub-THz. This will be valuable to predict performance degradation and assist the industrial design of sensor covers.

### **Motivation of the Study on Estimation of Complex Permittivity on Automotive Paints at Low-THz**

As stated above, automotive radars are typically installed behind bumpers, grills, and badges of the vehicles for the styling and protection purposes, and such cover infrastructure must be designed to keep attenuation losses at minimum to avoid detrimental effect on signal-to-noise ratio (SNR). The reflections from the vehicle infrastructure can also contribute into increase of leakage signal between automotive radar TX and vehicle components, which results in the increase of phase noise level [47]. In addition, the multiple reflections between radar and the vehicle components may lead to an incorrect estimation of the direction of arrival of the signal from a target [48]. The estimation of all these problems needs the information of CP of automotive paint layers, which is utilized for the decoration of most of the vehicle components.

The knowledge of the CP of materials, in particularly paint layers and substrate, is crucial to evaluate impact of the radar surrounding and enclosure on sensing performance [49, 45]. The estimations of dielectric constant of automotive paints and the effects of attenuation and reflection caused by paint layers have been investigated at 79 GHz in [5, 6]. However, the estimation of CP values has not been done at sub-THz frequency band before, and we are the first of considering this.

This part of research concerns with methodology of measurement of CPs of automotive paints within the wide range of frequencies from 0.14 to 1.1 THz using both Time Domain Spectroscopy (TDS) [50] and frequency domain Vector Network Analyzer (VNA) measurements [51–53]. The measured CPs are valuable for the modelling of attenuation and reflection of multi-layer vehicle infrastructure as function of frequency.

### **1.3.2 Image Segmentation on Automotive Radar Image**

The development of radar was for decades focused on reliable detection and tracking algorithms for typical road actors such as cars and pedestrians [54]. Some elements of classification were implemented based on the characteristics of radar returns, though it could potentially provide wider scene information e.g. class of surface, traditionally referred to as clutter, which was however subject to suppression. Additionally, traditional automotive radar did not possess the capabilities to effectively define, assess and classify clutter areas.

As opposed to traditional ADASs, for AD the identification of passable areas is the key task to achieve automated path planning and obstacle avoidance [54]. One of the approaches to identify the passable region from the sensed data is to segment and classify the surfaces and objects viewed by various sensors within a scene. Therefore, radar should be able to function as “clutter mapping and surface classification” sensor.

The approach proposed in this part of research aims at image segmentation and supervised classification of automotive radar images with multiple classes to be identified, so that each pixel within the image is ultimately labelled according to a determined class. It can be defined as a hybrid method (HM) consisting of initial edge-based pre-segmentation using the image processing method and a subsequent classification and region merging process on the pre-segmented regions of interest (ROI's) based on the statistical distribution parameters extracted from radar data. These will be used as features in a multi-variate Gaussian distribution (MGD) based supervised classifier.

For effective path planning, we aim to distinguish between tarmac, other transferable surfaces and regions consisting objects. Radar scattering from specific objects and clutters will be investigated as a function of grazing angle and resolution. Several types of distribution functions which are physically meaningful for the kind of clutter in the automotive environment will be investigated, and fitting errors evaluated and compared between region classes. In the results of full segmentation, each pixel is labelled according to its class, grouped into clusters (segments) and color coded for reconstructed scene representation.

Based on the proposed single frame segmentation of automotive radar map, we conduct the first study on developing an end-to-end (E2E) segmentation algorithm on radar imagery, which is a framework without any human interventions in the whole process. The segmentation performance has been improved and the moving targets indication (MTI) has been achieved based on frame to frame association (F2FA).

## 1.4 Outline of Work and Structure of Thesis

This dissertation includes two parts of work.

In the first part, we studied the propagation property of vehicle infrastructures at sub-THz. Chapter 2 focuses on the modelling of transmissivity and reflectivity of vehicle infrastructures at sub-THz. The theoretical model has been experimentally verified and is valuable for predicting the attenuation of sub-THz signals through solid mediums with known material characteristics. Based on the fact obtained from Chapter 2 that the automotive paint layers on vehicle infrastructures show significant influence to the attenuation, we studied the CPs of various commercial automotive paints at sub-THz in Chapter 3 which are also the key parameters for the modelling. At the end of each chapter, detailed conclusions are given in the final section. The main contributions of the first part of research are summarized in Chapter 4.

In Part II, the E2E segmentation algorithm on automotive radar images is developed. Chapter 5 is the initial attempt of the full scene image segmentation implementation on automotive radar images. The radar clutter features of different area classes are estimated, and the MGD classifier is proposed for region classification. We combined the developed supervised region classification method with the image processing methods to achieve the full scene reconstruction on automotive radar maps. The E2E framework in Chapter 6 is the extended study of the method proposed in Chapter 5. F2FA is utilized to improve the segmentation performance and achieve the function of MTI. Similar to the structure of Part I, conclusions of the individual chapters are given at the end of each chapter, and the main contributions of the second part of research are summarized in Chapter 7.

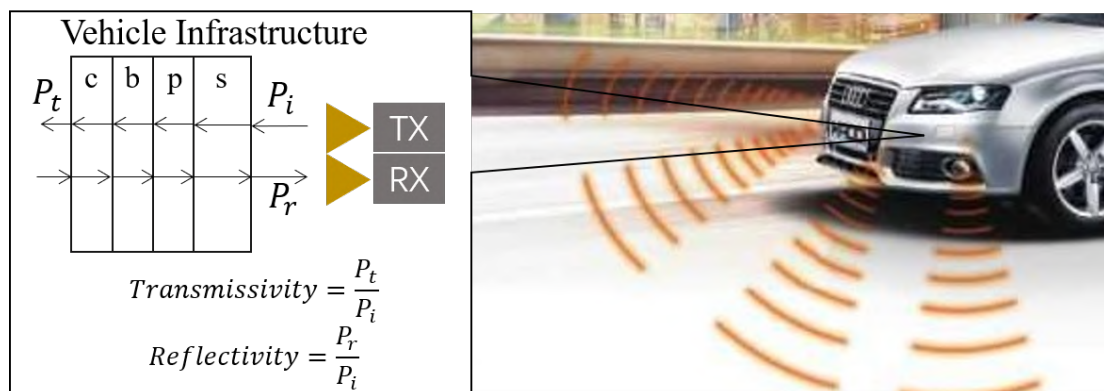
Last but not least, we discuss the potential future work of this thesis in Chapter 8.

## **Part I**

**Study on Transmissivity and  
Reflectivity of Low-THz signal through  
Vehicle Infrastructure.**

## Chapter 2

# Modeling and Experiment Verification of Transmissivity of Low-THz Radar Signal Through Vehicle Infrastructure



---

This chapter has been published as: [1] "Modeling and Experiment Verification of Transmissivity of Low-THz Radar Signal Through Vehicle Infrastructure," in IEEE Sensors Journal, vol. 20, no. 15, pp. 8483-8496, 1 Aug.1, 2020; [2] "Transmissivity Through Automotive Bumpers at mm-wave and Low-THz Frequencies," 2019 20th International Radar Symposium (IRS), 2019, pp. 1-6. Author Contributions: The authors confirm their contribution to the chapter as follows: study conception and design: Y.Xiao, F.Norouzian, M.Gashinova, M.Cherniakov; experiment operation: Y.Xiao, E.G.Hoare, E.Marchetti; data collection: Y.Xiao; analysis and interpretation of results: Y.Xiao, F.Norouzian; manuscript preparation: Y.Xiao, F.Norouzian, E.G.Hoare, M.Gashinova, M.Cherniakov.

## 2.1 Introduction

This chapter is concerned with modelling of the transmissivity of Low-Terahertz waves through automotive bumper and headlight cover material. This work is part of wider comprehensive studies on the potential of use higher frequency bands for future automotive sensors. Theoretical models for transmissivity prediction are described, the methodology of experimentation is discussed and experimental results are presented. The theoretical models of reflection and transmission of different base materials which are covered by different layers of paint are based on Fresnel theory, and the phenomena caused by the half wavelength thickness of the medium is analyzed mathematically. The experimental verification of the models have been undertaken at 300 GHz and 670 GHz, using 77 GHz as a reference frequency.

This chapter is organized as follows. In section 2.2, the theoretical models of transmission of multi-layer structures are determined based on Fresnel's theory. The transmissivity simulations of headlight-cover (one-layer structure) and bumpers (four-layer structure) are based on this model. Also, the effect of the integer half wavelength electrical thickness of the medium on transmissivity and reflectivity is analyzed mathematically. The transmissivity is simulated through bumpers with different types of paint and the effect of various types of paint is analyzed. Section 2.3 introduces the measurement methodology, using a reference frequency of 77 GHz, and at the Low-THz 300 GHz and 670 GHz frequencies. All the experimental results are shown in Section 2.4. The effective permittivities of the vehicle component samples are estimated using the free space method. The measured and simulated transmissivities of automotive materials are compared and good agreement between them is obtained. The modelling in this chapter is based on reflection and transmission coefficients for horizontal polarization, since the polarization of the antennas used in our experiments are horizontal.

## 2.2 Analytical Model

The general layout of infrastructure covering automotive sensors is shown in Fig. 1.13. We assume that the cover is a stack of planar layers consisting of base material and different paints, each with its own physical parameters and thickness.

When radiation strikes a surface between air and the cover, part of the signal is absorbed, part of it is reflected, and the remaining part is transmitted through the cover material. The ratio of the reflected power to incident power is defined as “Reflectivity”, which indicates reflections from each interfaces inside the medium, and the fraction of the incident power that is transmitted through the medium is defined as “Transmissivity” which indicates the signal reduction as a result of absorption inside and reflections from each interface [26]. The section of 2.2.1 will give the fundamental of Fresnel’s equations which describe the reflection and transmission coefficients of electromagnetic radiation incident on an interface between different optical media. In part 2.2.2, the transmissivity and reflectivity for the multi-layer medium and headlight cover are simulated at 77 GHz, 300 GHz and 670 GHz. The incident angle of the microwave signal and thickness of the medium at different frequency bands are considered as the variables of the transmissivity and reflectivity simulation. The phenomenon of periodic changes on simulated results, which will be shown in this section, is due to the interference between reflections from boundaries of the media. Transmissivity through automotive bumpers with different substrate material and various paints are investigated at 300 GHz and 670 GHz based on the CPs of automotive paints measured by TDS.

### 2.2.1 Fresnel Equations

When light or electromagnetic radiation strikes the interface between two mediums with different refractive indexes, both transmission and reflection effects may occur. The conditions of two polarization cases are shown in Fig. 2.1. The definitions of parameters in Fig. 2.1 are:  $\theta_i$  is incident angle,  $\theta_r$  is reflection angle,  $\theta_t$  is transmission angle,

$n_1$  is the refractive index of medium 1 and  $n_2$  is for medium 2. Two different linear polarization components of the incident wave, which are S polarization (presented in Fig. 2.1(a)) and P polarization (presented in Fig. 2.1(b)), correspond to two sets of Fresnel coefficients. In the *s* polarization, the electric field is normal to the incidence plane and magnetic field is in the plane of incidence. The *p* polarization refers to the opposite condition where the electric field is in the plane of incidence, and the magnetic field is normal to the plane of incidence.

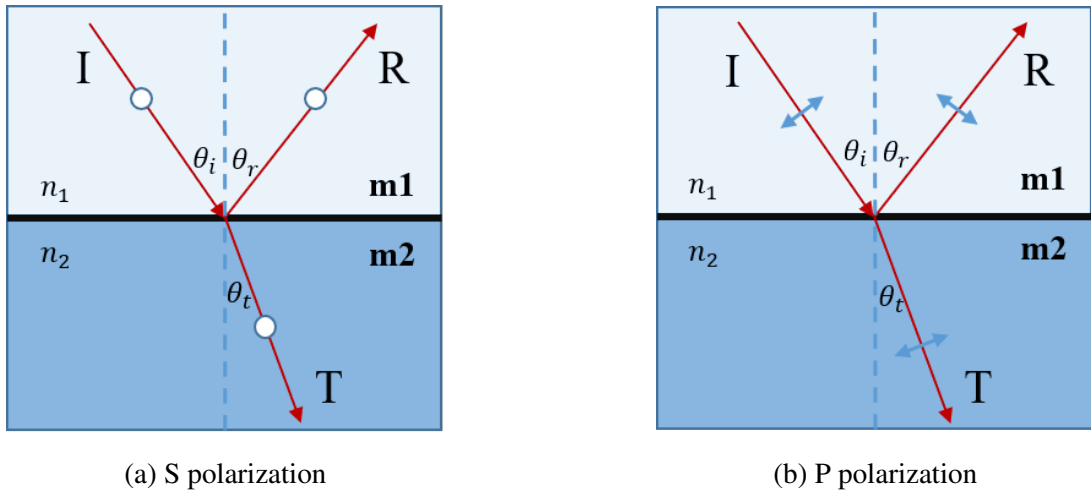


Fig. 2.1 The boundary conditions when signal strikes at an interface.

The relationship between these angles is given by the law of reflection and Snell's law:

$$\theta_i = \theta_r \quad (2.1)$$

$$n_1 \sin \theta_i = n_2 \sin \theta_t \quad (2.2)$$

The Fresnel equations for the two polarization cases are:

$$r_s = \frac{\eta_1 \cos \theta_i - \eta_2 \cos \theta_t}{\eta_1 \cos \theta_i + \eta_2 \cos \theta_t}, t_s = \frac{2 \eta_1 \cos \theta_i}{\eta_1 \cos \theta_i + \eta_2 \cos \theta_t} \quad (2.3)$$

$$r_p = \frac{\eta_2 \cos \theta_i - \eta_1 \cos \theta_t}{\eta_2 \cos \theta_i + \eta_1 \cos \theta_t}, t_p = \frac{2 \eta_1 \cos \theta_i}{\eta_2 \cos \theta_i + \eta_1 \cos \theta_t} \quad (2.4)$$

In which,  $r_s$  and  $t_s$  are the reflection coefficient and transmission coefficient of s polarized signal,  $r_p$  and  $t_p$  are the reflection coefficient and transmission coefficient of p polarized signal.  $\eta_1$  and  $\eta_2$  are the wave impedance of medium 1 and 2, which are calculated as:

$$\eta_i = \sqrt{\frac{j\omega\mu_i}{\sigma_i + j\omega\epsilon_0\epsilon_i}} \quad (2.5)$$

Here,  $\epsilon_0 = 8.854 \times 10^{-12}$  is the permittivity of free space,  $\mu_i$  and  $\epsilon_i$  are the permeability and relative permittivity of material,  $\sigma_i$  is the conductivity and  $\omega$  is the frequency. The Fresnel equations are the basic of the following theoretical model of transmissivity and reflectivity of vehicle infrastructure.

## 2.2.2 Theoretical Model of Transmission of Multi-Layer Structure

### Medium: “General Approach”

The theoretical model used to simulate transmissivity through multi-layer medium in this study are based on Fresnel’s theory and calculation of propagation matrices in [55].

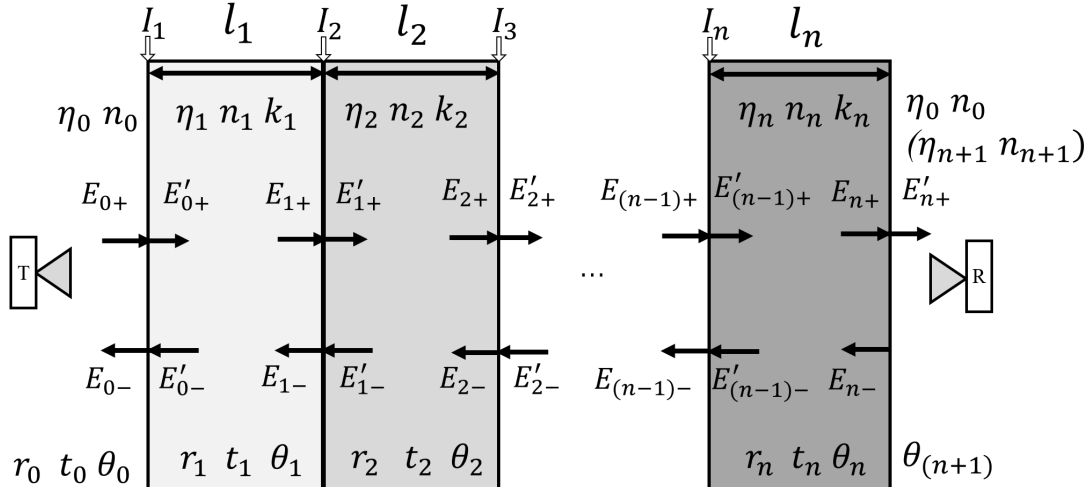


Fig. 2.2 The electric field in the propagation process through a multi-layer sample.

The propagation process through a multi-layer medium is shown in Fig. 2.2 where for simplicity only orthogonal incidence is shown. The notation of the parameters are as follow:  $E_{(i+)}$ ,  $E_{(i-)}$  and  $E'_{(i+)}$  are the incident, reflected and transmitted electric fields.

$\theta_i$  is the incident angle within each layer, defined by Snell's law.  $\eta_i$  and  $k_i$  are the wave impedance and wave number in  $i$ th layer [26],  $r_i$  and  $t_i$  are reflection and transmission coefficient of p polarization at interface  $I_{(i+1)}$ , which can be determined using Fresnel equations as in Eq. 2.3 and 2.4.

Based on the reflection and transmission coefficient and the electro-physical parameters of materials, the matrix of the electric field of the transmission process of multi-layer media is calculated by stacking the matching matrix  $\mathbf{M}_{mi}$  of each interface and the propagation matrix  $\mathbf{M}_{pi}$  of each layer of media [56]:

$$\begin{aligned} \begin{vmatrix} E_{0+} \\ E_{0-} \end{vmatrix} &= \mathbf{M}_{m0} \times \mathbf{M}_{p1} \times \mathbf{M}_{m1} \dots \mathbf{M}_{pn} \times \mathbf{M}_{mn} \begin{vmatrix} E'_{n+} \\ 0 \end{vmatrix} \\ &= \begin{vmatrix} A_{1,1} & A_{1,2} \\ A_{2,1} & A_{2,2} \end{vmatrix} \begin{vmatrix} E'_{n+} \\ 0 \end{vmatrix} \end{aligned} \quad (2.6)$$

Here matching matrix  $\mathbf{M}_{mi}$  and propagation matrix  $\mathbf{M}_{pi}$  are denoted as:

$$\mathbf{M}_{mi} = \begin{vmatrix} 1 & r_i \\ r_i & 1 \end{vmatrix} \quad (2.7)$$

$$\mathbf{M}_{pi} = \begin{vmatrix} e^{jk_1 l_1} & 0 \\ 0 & e^{-jk_1 l_1} \end{vmatrix} \quad (2.8)$$

and  $A_{i,j}$  represents the elements of the transmission matrix. The transmissivity and reflectivity are represented as:

$$T = \left| \frac{E'_{n+}}{E'_{0+}} \right|^2 = \left| \frac{1}{A_{1,1}} \right|^2, \Gamma = \left| \frac{E_{0-}}{E_{0+}} \right|^2 = \left| \frac{A_{2,1}}{A_{1,1}} \right|^2 \quad (2.9)$$

The model for the transmissivity through the automotive bumper is therefore based on general N-layer structure transmission matrix.

In a practical application, the radar signal propagates in a round trip and through the automotive components from both surfaces. For example, when a radar is installed behind the bumper, the signal will propagate from the plastic substrate to paint layer (forward path) for the first path and then from the paint layer to substrate (return path) when reflected back. Therefore, it is necessary to understand the relationship between the transmissivity of both cases theoretically.

The parameters without prime ( $\theta_i, r_i, t_i$ ) refer to "forward path" and parameters with prime ( $\theta'_i, r'_i, t'_i$ ) refer to "return path". According to Snell's law, ray angles of each interface are only determined by the refractive indices of two adjacent media. For non-magnetic materials, ray angles  $\theta'_0, \dots, \theta'_{n+1}$  in the return path will be equal to the angles  $\theta_{n+1}, \dots, \theta_0$  in the forward path. Similar as the reflection and transmission coefficients of "forward path" which are presented in Eq. 2.3 and 2.4, the coefficients in return path are denoted as:

$$r'_i = \frac{\eta_{n-i} \cos \theta_{n+1-i} - \eta_{n+1-i} \cos \theta_{n-i}}{\eta_{n-i} \cos \theta_{n+1} + \eta_{n+1} \cos \theta_{n-i}}, t'_i = \frac{2\eta_{n-i} \cos \theta_{n+1-i}}{\eta_{n-i} \cos \theta_{n+1-i} + \eta_{n+1} \cos \theta_{n-i}} \quad (2.10)$$

Therefore, comparing with reflection and transmission coefficient for forward path, we can obtain the equal relationships:  $r'_i = -r_{n-i}$  and  $\prod_{i=0}^n t_i = \prod_{i=0}^n t'_i$ . The propagation matrix of both forward path and return path for three-layer structure can be represented as Eq. 2.11 and Eq. 2.12:

$$\begin{aligned} \begin{vmatrix} E_{0+} \\ E_{0-} \end{vmatrix} &= \frac{1}{t_0 t_1 t_2 t_3} \begin{vmatrix} 1 & r_0 \\ r_0 & 1 \end{vmatrix} \times \begin{vmatrix} e^{j\varphi_1} & 0 \\ 0 & e^{-j\varphi_1} \end{vmatrix} \times \begin{vmatrix} 1 & r_1 \\ r_1 & 1 \end{vmatrix} \dots \times \\ &\quad \begin{vmatrix} e^{j\varphi_3} & 0 \\ 0 & e^{-j\varphi_3} \end{vmatrix} \times \begin{vmatrix} 1 & r_3 \\ r_3 & 1 \end{vmatrix} \begin{vmatrix} E'_{3+} \\ 0 \end{vmatrix} = \begin{vmatrix} A_{1,1} & A_{1,2} \\ A_{2,1} & A_{2,2} \end{vmatrix} \begin{vmatrix} E'_{3+} \\ 0 \end{vmatrix} \end{aligned} \quad (2.11)$$

$$\begin{aligned} \begin{vmatrix} E_{0+} \\ E_{0-} \end{vmatrix} &= \frac{1}{t_0 t_1 t_2 t_3} \begin{vmatrix} 1 & -r_3 \\ -r_3 & 1 \end{vmatrix} \times \begin{vmatrix} e^{j\varphi_3} & 0 \\ 0 & e^{-j\varphi_3} \end{vmatrix} \times \begin{vmatrix} 1 & -r_2 \\ -r_2 & 1 \end{vmatrix} \dots \times \\ &\quad \begin{vmatrix} e^{j\varphi_1} & 0 \\ 0 & e^{-j\varphi_1} \end{vmatrix} \times \begin{vmatrix} 1 & -r_0 \\ -r_0 & 1 \end{vmatrix} \begin{vmatrix} E'_{3+} \\ 0 \end{vmatrix} = \begin{vmatrix} A'_{1,1} & A'_{1,2} \\ A'_{2,1} & A'_{2,2} \end{vmatrix} \begin{vmatrix} E'_{3+} \\ 0 \end{vmatrix} \end{aligned} \quad (2.12)$$

Here,  $\varphi_i = k_i l_i \cos \theta_i$ . After extending the propagation matrix (Eq. 2.11 and 2.12), the transmissivity equation for both two cases ( $T$  and  $T'$  are the transmissivity for forward and return path respectively) are the same as shown in Eq. 2.13 below:

$$T = T' = \left| \frac{A}{B} \right|^2 \quad (2.13)$$

where  $A = t_0 t_1 t_2 t_3 e^{-j\varphi_1} e^{-j\varphi_2} e^{-j\varphi_3}$ ,  $B = 1 + r_0 r_1 e^{-j2\varphi_1} + r_1 r_2 e^{-j2\varphi_2} + r_0 r_2 e^{-j2\varphi_1} e^{-j2\varphi_2} + r_2 r_3 e^{-j2\varphi_3} + r_0 r_1 r_2 r_3 e^{-j2\varphi_1} e^{-j2\varphi_3} + r_1 r_3 e^{-j2\varphi_2} e^{-j2\varphi_3} + r_0 r_3 e^{-j2\varphi_1} e^{-j2\varphi_2} e^{-j2\varphi_3}$ . Therefore, we can draw the conclusion that when a signal travels through the multi-layer sample in two opposite directions, the transmissivities are the same, the transmissivity value in a round trip can be obtained directly by just doubling transmissivity of one way through the medium. Hence all the results obtained in this study are directly applicable for radar scenario, i.e. two-way propagation.

### 2.2.3 Modeling Results of the Transmissivity Through Headlight-Cover: Single Layer Case

Headlight covers of vehicles are made of various materials of which polycarbonate (PC) is currently the most common one. The simulated transmissivity through a headlight-cover based on the one-layer propagation matrices model is presented in this section. The values of PC material at 77 GHz, 300 GHz and 670 GHz were obtained in [57–59] and are summarized in Table. 2.1. The imaginary part of refractive index is calculated using the measured absorption coefficient of PC material as described in [58, 59].

Table 2.1 Ranges of the relative permittivity of PC at 77 GHz, 300 GHz and 670 GHz.

Frequency	77 GHz	300 GHz	670 GHz
$\epsilon'$	2.98-3.59	2.55-2.99	2.5-3.1
$\epsilon''$	0.02-0.053	0.039-0.052	0.058-0.066

The transmissivity (Fig. 2.3) and reflectivity (Fig. 2.4) of PC as a function of incident angle and the thickness of the medium are simulated for all the three frequencies. Error bars represent the uncertainty of transmissivity in the range of permittivity of PC as shown in Table 2.1. The actual thickness of headlight-cover sample cut from the vehicle is 3.2 mm, which is used as the thickness parameter when simulating transmissivity and reflectivity as a function of incident angle. Transmissivity and reflectivity as function of thickness are simulated for  $0^\circ$  incidence.

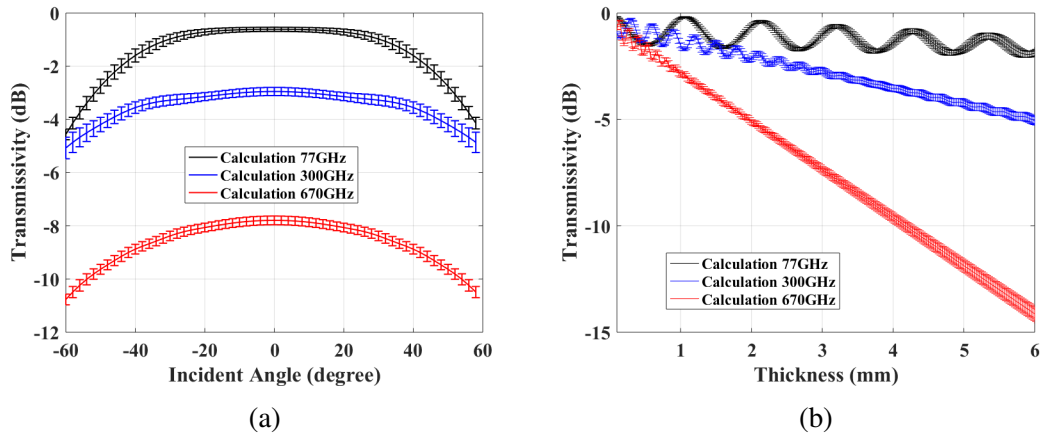


Fig. 2.3 Simulated transmissivity as a function of incident angle (a) and thickness (b) at 77 GHz, 300 GHz and 670 GHz.

Fig. 2.3(a) illustrates that the simulated transmissivity through the headlight-cover at normal incidence is at approximately -0.6 dB, -3 dB and -8 dB at 77 GHz, 300 GHz and 670 GHz, respectively. At incident angles of  $\pm 60^\circ$ , the transmissivity is decreased by 4 dB, 2 dB and 3 dB at 77 GHz, 300 GHz and 670 GHz respectively. Fig. 2.3(b) shows how transmissivity changes with thickness. For example, transmissivity decreases about

-2 dB, -5 dB and -14 dB when the thickness increases from 0.1 mm to 6 mm at 77 GHz, 300 GHz and 670 GHz, respectively.

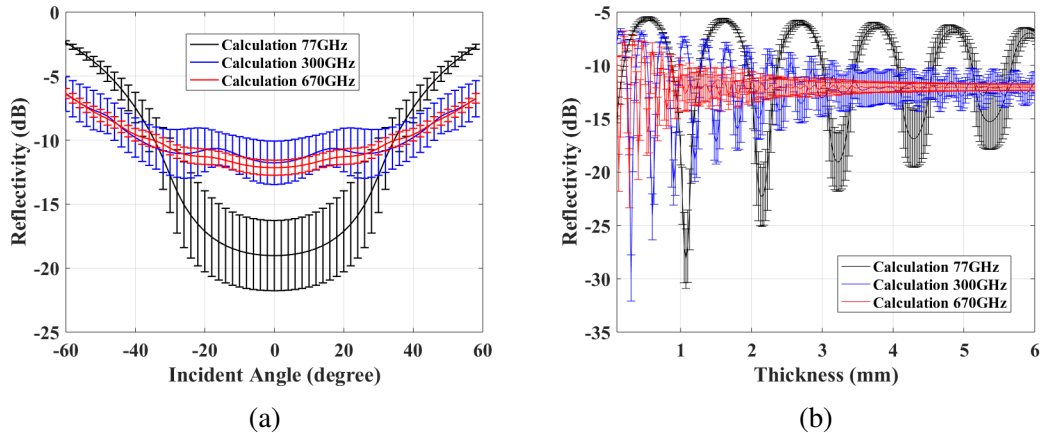


Fig. 2.4 Simulated reflectivity as a function of incident angle (a) and thickness (b) at 77 GHz, 300 GHz and 670 GHz.

Simulated values of transmissivity indicate periodic oscillations with amplitudes getting smaller with increase of frequency and/or thickness. Simulated reflectivity in Fig. 2.4(b) shows similar trend where the depth of amplitude minima decreases with increased thickness.

Such oscillations relates to the changing ratios of half wavelength and thickness of the propagation layer as explained below. Let us consider idealized and realistic scenarios of interference of two reflected waves from two interfaces of a single layer with the thickness equal to integer multiple of  $\lambda_0/(2n)$  ( $n$  is the refractive index of the medium,  $\lambda_0$  is the wavelength in vacuum) as shown in Fig. 2.5, where signal 1 (solid line) and signal 2 (dashed line) correspond to the reflected signals from the first and second interfaces. In the ideal case (no attenuation inside the layer), they entirely cancel each other. The power of the reflected signal is zero this case and transmissivity shows a maximum value. However, in the realistic case the reflected signal 2 from the second boundary cannot totally cancel out the reflected signal from the first interface due to the attenuation inside the medium. Therefore, when the attenuation in the medium increases with increase of frequency, the amplitude of interference signal is bigger,

indicating incomplete cancellation. Therefore, at the values of thickness corresponding to multiples of the half-wavelength the reflectivity will have reduced depth of the nulls with the increase of frequency.

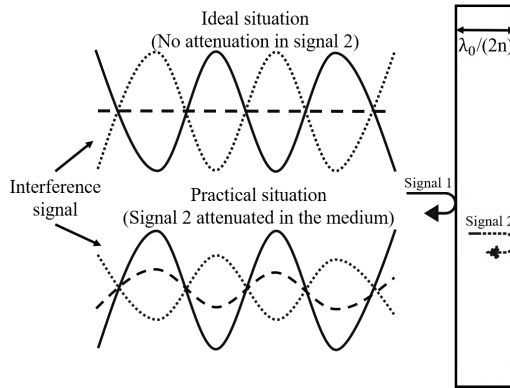


Fig. 2.5 Illustration of the interference between the signals reflected by both boundaries of the medium of thickness equal to integer multiple of the half-wavelength.

To prove this phenomenon mathematically, we can simplify the transmissivity equation for one-layer medium Eq. 2.9 as in Eq. 2.14:

$$\begin{aligned} T &= \left| \frac{t_0 t_1 e^{-jk_1 l_1}}{1 + r_0 r_1 e^{-2jk_1 l_1}} \right|^2 \\ &= \left| \frac{2\eta_1\eta_0}{(\eta_1^2 + \eta_0^2) j \sin(k_1 l_1) + 2\eta_1\eta_0 \cos(k_1 l_1)} \right|^2 \end{aligned} \quad (2.14)$$

where  $\eta_0$  and  $\eta_1$  are intrinsic impedances of wave in the medium and free space, respectively. They are defined as  $\eta_i = \sqrt{\frac{j\omega\mu_i}{\delta_i + j\omega\epsilon_0\epsilon_i}}$ , in which  $\mu_0 = 4\pi \times 10^{-7}$ ,  $\epsilon_0 = 8.854 \times 10^{-12}$  for free space and  $\mu_1$  and  $\epsilon_1$  are the permeability and relative permittivity of material,  $\delta_i$  is the conductivity and  $\omega$  is the frequency.

## 2.2.4 Modeling Results of the Transmissivity Through Bumper.

### Multi-Layer Case

Typically, modern bumpers are composed of three main elements: fascia, energy absorber and bumper beam [60, 61]. In this research, only the outside bumper fascia

is considered as an obstacle for the radar signal propagation, which consists of the plastic substrate and paint layers. The layer structure of bumper and the thickness range for each layer are shown in Fig. 2.6. The materials of the substrate were reported to be Polypropylene (PP) and PC/Polyethylene terephthalate (PET) in [38] and [5], respectively. The plastic substrate is usually made of a combination of thermoplastic polymer, carbon black and talc. The CP of substrate layer depends on the composition of materials.

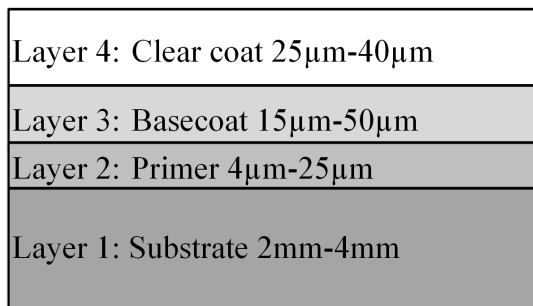


Fig. 2.6 Sketch of four-layer bumper and the range of the thickness for each layer.

Three kinds of automotive paints commonly used in vehicles: solid paint, metallic paint and pearlescent paint. Generally, automotive paints include primer, basecoat and clear coat. The primer layer ensures better adhesion of paint, the base coat layer is for color application and clear coat layer is used for protecting the paint from scratches and bad weather.

The bumper samples used in this experiment cut from vehicle components which were provided by Jaguar Land Rover (JLR). Three automotive bumper samples with white solid paint, gold metallic paint and red pearlescent paint are shown in Fig. 2.7 as the example.

In this analytical section, we would like to understand the attenuation effects caused by various paint layers. To ensure that the only variable in this analysis is the paint layer, the substrate material is assumed to be PC, which is a commonly used vehicle plastic. The simulation structure consists of four layers: the substrate and the paint layers of

primer, basecoat and clear coat. The permittivity parameters of PC are shown in Table 2.1.



Fig. 2.7 Automotive bumpers with solid paint, metallic paint and pearlescent paint used for the experiments.

Table 2.2 CP of materials used in simulation ( $\epsilon_r/\epsilon_i$ ).

Material	77 GHz	300 GHz	670 GHz	Thickness
Plastic substrate	2.98/0.1	2.75/0.045	2.8/0.062	4 mm
Primer	9/0.06	5.29/0.08	5.15/0.12	25 $\mu m$
Clear coat	3.5/0.1	2/0.07	2.7/0.09	40 $\mu m$
Solid base coat	9.99/0.907	3.07/0.1	2.99/0.14	50 $\mu m$
Metallic base coat	5.99/1.609	4.94/0.2	5.14/0.6	50 $\mu m$
Pearlescent base coat	3.22/0.007	2.77/0.12	2.65/0.06	50 $\mu m$

The permittivity values of primer, base coat, and clear coat used in transmissivity and reflectivity simulation are presented in Table 2.2. The 77 GHz values are obtained from previous work in [5, 62]. For Low-THz frequency range (300 GHz and 670 GHz), permittivity has been measured using the TDS setup at the University of Birmingham. TDS is a spectroscopic technique and utilize a short pulses of THz frequency radiation with a wideband spectrum, which is used widely to extract permittivity of large variety of materials [58, 63, 64]. For each simulation, the only variable of this simulation is the CP of material of base coat paint layer, which is extracted from solid, metallic and pearlescent paints respectively. CP of plastic substrate, primer and clear coat are the same at each frequency. According to the measured permittivity values, as well as those reported in [5], metallic paint, as expected, has a higher imaginary part of permittivity

compared with solid and pearlescent paint because of the metal concentration. The simulated transmissivity and reflectivity of the bumper with three different kinds of base coat paint layer at 77 GHz, 300 GHz and 670 GHz are represented in Fig. 2.8, 2.9, 2.10, respectively.

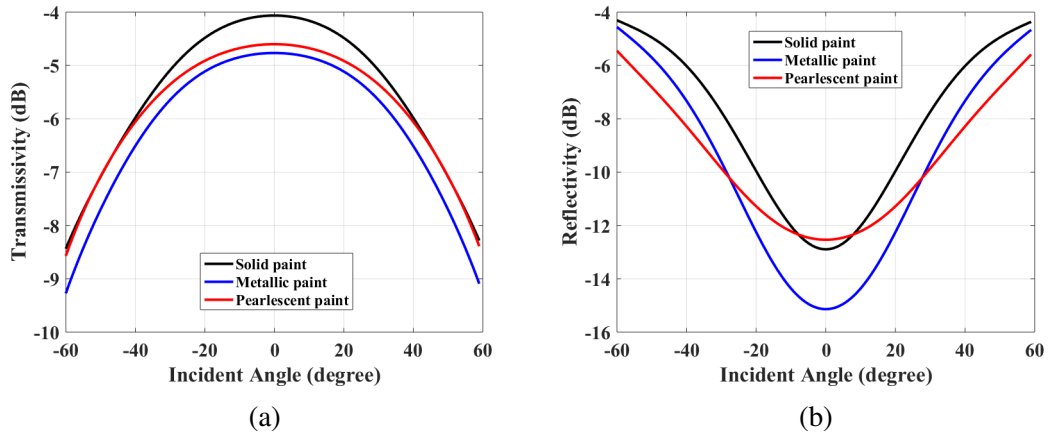


Fig. 2.8 The simulated transmissivity (a) and reflectivity (b) of four-layer bumper with solid, metallic and pearlescent paint at 77 GHz.

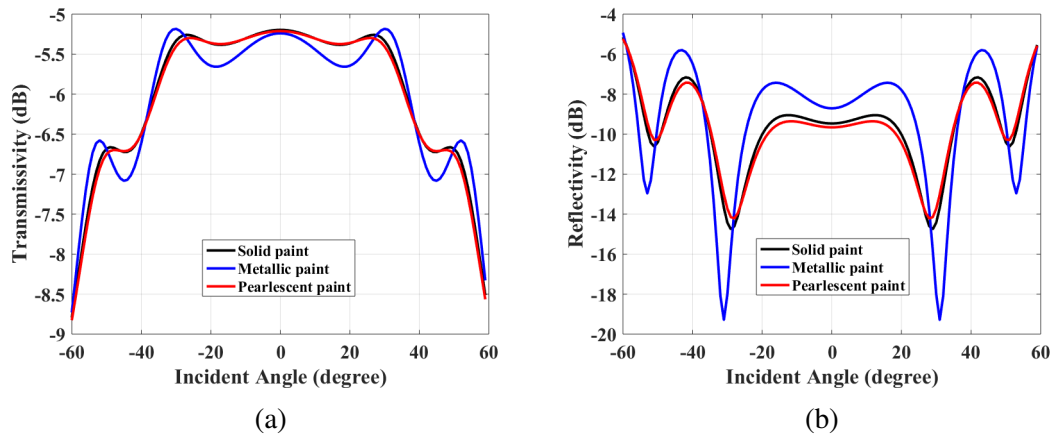


Fig. 2.9 The simulated transmissivity (a) and reflectivity (b) of four-layer bumper with solid, metallic and pearlescent paint at 300 GHz.

According to Eq. 2.14, the amplitude of the minimum and maximum values of transmissivity and reflectivity are also influenced by the real part of permittivity, higher  $\epsilon_{re1}$  values cause larger variations in the amplitude of transmissivity and reflectivity. This conclusion can be observed in the simulation result of metallic paint which has a

higher real part of permittivity at 300 GHz. In addition, the metallic paint with higher dielectric loss factor also causes higher attenuation at both frequencies.

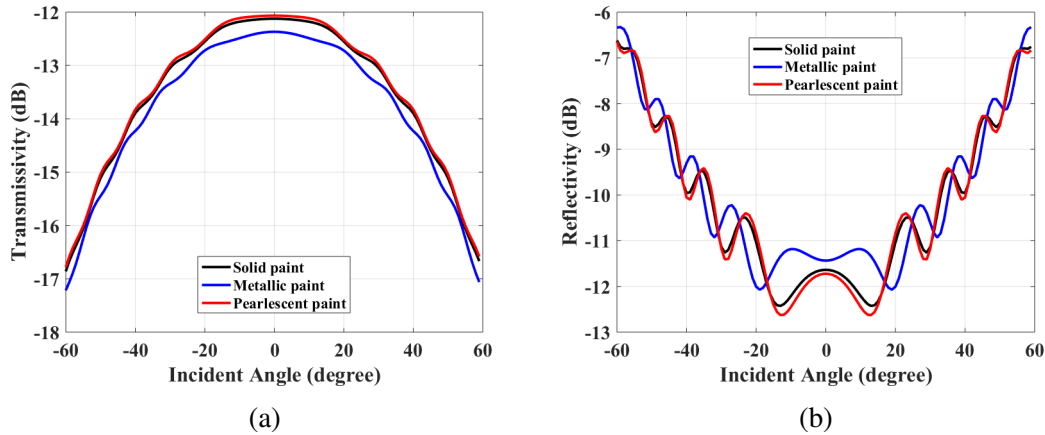


Fig. 2.10 The simulated transmissivity (a) and reflectivity (b) of four-layer bumper with different kinds of paint at 670 GHz.

## 2.3 Measurement Methodology

The methodology to measure transmissivity through various samples at three frequencies is explained in this section. To obtain the transmissivity value, the transmitted signal strength through the automotive component samples is normalized by the transmissivity through free space in the below experiments. Fig. 2.11(a) is a photo of the experimental setup for measuring transmissivity, Fig. 2.11(b) is the measurement layout for the single path transmission measurement setup, which is commonly used for transmissivity measurement [39]. In the main configuration the up and down-converters are positioned separately on two tables. The distance between receiver and transmitter is 1.4 m, and antennas of up and down converter are aligned vertically and horizontally. The antennas are placed 0.7 m above the floor level. The sample is fixed on a low reflectivity sample holder positioned on a rotating platform which can change the incident angle in 1° increments. The reflectivity of the sample holder has been measured as -33 dB and -21.2 dB at 300 GHz and 670 GHz, respectively. To ensure that most of the energy

illuminates the material, the sample is positioned closer to transmitter to make sure that the sample is larger than the footprint of the illuminating beam. The beamwidth is defined by 3 dB main lobe of the radiation pattern. Extra attention has been paid to make sure the samples are orthogonal to the antennas horizontal baseline. The Low-THz wave absorber [65] is placed in front of the wall closest to the antennas to minimize reflections from the surrounding.

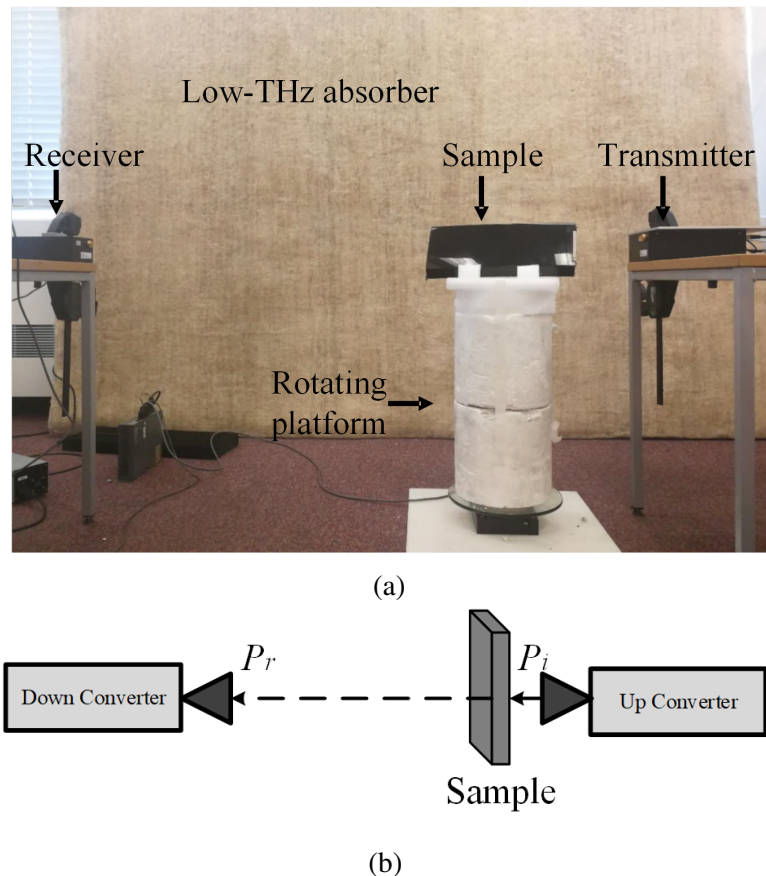


Fig. 2.11 (a) The experimental setup for measuring transmissivity (the radar system shown in the setup is 670 GHz SFR); (b) Schematic diagram of the measurement setup.

The distance between sample and transmitter is set to be 0.4 m at all frequencies to guarantee that the experiment is conducted in far-field region. In real applications, the sensor covers will be closer to the antennas, so that the near-field effects may be expected. However, in this study far field set-up is considered to provide a reference for

validation of the modelling results. The near field effects and corresponding corrections to the modelling are subject of further research.

All measurements are made at three frequencies: two stepped frequency radars (SFRs) with the sweep frequency of 282 GHz-298 GHz and 656 GHz-672 GHz, and one FMCW radar system with the frequency coverage of 76 GHz-81 GHz using standard gain horn antennas.

The SFR systems are based on the KEYSIGHT Programmable Network Analyzers (PNA) and the up and down converters designed by VivaTech in collaboration with University of Birmingham [66]. The signal from the PNA is up-converted into frequency of  $F_t$  and transmitted through the bumper sample under measurement.  $S_{21}$  parameter of the down converted signal is measured to obtain the transmissivity value. A 10 MHz reference signal is provided from a Rubidium oscillator to phase lock the converters and PNA. The 77 GHz FMCW radar system is designed by ELVA-1 in collaboration with University of Birmingham [67]. All the frequency, power and antenna parameters are shown in Table 2.3 for all the radar systems.

Table 2.3 Parameters for 77 GHz, 300 GHz and 670 GHz radar systems.

Frequency	77 GHz	300 GHz	670 GHz
Radar classification	FMCW	SFR	SFR
Frequency Bandwidth	76-81 GHz	282-298 GHz	656-672 GHz
PNA output power $P_p$	x	-15 dBm	-15 dBm
Transmitted power $P_t$	15 dBm	3 dBm	-10 dBm
Antenna Gain	20 dB	20 dB	24 dB
Azimuth/Elevation Beam width (-3 dB)	10°	10°	10°
$F_p$	CW experiment	x	7 GHz
	Bandwidth experiment	x	2-18 GHz
$F_t$	CW experiment	77-77.1 GHz	289 GHz
	Bandwidth experiment	76-81 GHz	656-665 GHz

Three variable parameters are considered in this study to evaluate transmissivity: incident angle of signal, frequency and thickness of medium. The influence of the initial two variables are explored by measuring the transmissivity of bumpers and headlight-cover as a function of incident angle and frequency as the thickness remains constant.

However, to investigate the third variable, PC sheets with thicknesses ranging from 2 mm to 6 mm are measured. A CW signal is used to measure transmissivity versus incident angle and thickness, and bandwidth signal is used to understand the frequency dependence. As shown in Table 2.3,  $F_t$  for the CW experiment at 77 GHz the bandwidth is 100 MHz since this is the minimum operational bandwidth of the FMCW radar.

## 2.4 Experimental Results

In this section, the measured and simulated transmissivity of car bumper and headlight cover material, as well as PC sheets of different thicknesses, are shown as a function of incident angle and frequency. Bumper samples with three kinds of paints and one piece of headlight-cover are measured to determine the transmissivities of these vehicle components. The effective permittivity is obtained using the free space method [68] based on the measured transmissivity as function of incident angle. The effective permittivity is used for modelling the transmissivity versus frequency bands. Various thicknesses of PC sheets are used to replicate common plastic material used as headlight covers.

Table 2.4 Characteristics of automotive samples.

The effective permittivity ( $\epsilon_r - j\epsilon_i$ ) and transmissivity at  $0^\circ$  ( $T(0^\circ)$ ).

PP: Polypropylene; E/P: Ethylene / Propylene; PUR: polyurethane; PC: polycarbonate.

Sample	Paint Classification	Size( $m^2$ )	D(mm)	Plastic	77 GHz ( $\epsilon_r', \epsilon_r'', T(0^\circ)$ )			300 GHz ( $\epsilon_r', \epsilon_r'', T(0^\circ)$ )			670 GHz ( $\epsilon_r', \epsilon_r'', T(0^\circ)$ )		
					$\epsilon_r'$	$\epsilon_r''$	$T(0^\circ)$	$\epsilon_r'$	$\epsilon_r''$	$T(0^\circ)$	$\epsilon_r'$	$\epsilon_r''$	$T(0^\circ)$
A	Solid black	0.057	2.87	PP,E/P	4.02	0.035	-0.5 dB	2.48	0.025	-1.9 dB	3.36	0.02	-2.8 dB
B	Solid white	0.076	3.72	PP,E/P	4.34	0.03	-0.7 dB	3	0.021	-2.1 dB	4.26	0.022	-3.0 dB
C	Solid white	0.045	3.33	PP,E/P	5.38	0.042	-1.5 dB	2.78	0.036	-2.4 dB	3.37	0.038	-4.1 dB
D	Solid white	0.095	3.02	PP,E/P	4.29	0.022	-2.0 dB	3.76	0.033	-2.7 dB	3.24	0.019	-2.0 dB
E	Metallic gold	0.078	3.15	PP,E/P	5.65	0.025	-1.0 dB	3.68	0.043	-3.1 dB	2.3	0.043	-5.8 dB
F	Metallic grey	0.09	3.26	PP,E/P	4.58	0.003	-2.0 dB	4.8	0.051	-2.7 dB	5.00	0.042	-6.0 dB
G	Pearlescent red	0.04	3.25	PP,E/P	3.5	0.026	-1.0 dB	2.91	0.039	-2.5 dB	3.00	0.04	-5.0 dB
H	Pearlescent red	0.038	3.33	PP,E/P	5.73	0.023	-0.2 dB	3.5	0.024	-1.3 dB	3.6	0.036	-4.6 dB
I	Pearlescent green	0.065	3.27	PP,E/P	3.49	0.029	-0.6 dB	2.54	0.024	-1.3 dB	2.65	0.014	-3.0 dB
J	Pearlescent white	0.074	3.34	PUR	6.95	0.04	-5.8 dB	2.63	0.12	-7.4 dB	3.74	0.186	-20 dB
K	Headlight cover	0.057	3.2	PC	3.55	0.019	-0.4 dB	2.6	0.043	-2.4 dB	2.52	0.058	-7.9 dB

### 2.4.1 Measured Transmissivity through Automotive Bumper and Headlight Cover

Ten bumper samples and one headlight-cover have been used in experimentation. The material information is presented in Table 2.4, samples A to K.

The multi-layer transmissivity model requires the exact knowledge of permittivity of materials and the thickness of each layer. The exact refractive index of each layer of paint on the samples, at Low-THz frequencies, are unknown and in addition the thicknesses of the paint layers are difficult to measure without knowing the exact refractive indexes of the materials [69]. Consequently, a model of the transmissivity through a four-layer bumper cannot be directly established at this stage. Therefore, a one-layer structure, with the effective permittivity of the whole sample, is used to model transmissivity through the bumper material. The effective permittivities of the bumper samples are calculated using the measured transmissivity and used for further modelling.

There are two common methods to characterize the permittivity of the samples: (i) TDS is used for THz frequency (usually more than 300 GHz), and (ii) the free-space method [68] which uses a VNA is used for lower frequencies [51]. In this study, the effective relative permittivity is determined using the method described in [26], by minimization of the deviation between the measured and simulated transmissivity results. The deviation,  $Dev$ , between the simulated transmissivity  $T_c$  and the measured transmissivity  $T_m$ , is obtained as:

$$Dev(\epsilon'_r, \epsilon''_r) = \left| \frac{\sum_{i=1}^N T_m(\theta_i) - T_c(\theta_i, \epsilon'_r, \epsilon''_r)}{N} \right| \quad (2.15)$$

in which,  $N$  is the number of considered incident angles,  $\theta_i$  is the incident angle of the microwave signal which is in range of  $-60^\circ$  to  $60^\circ$ ,  $\epsilon'_r$  and  $\epsilon''_r$  are the real and imaginary parts of the complex effective permittivity.

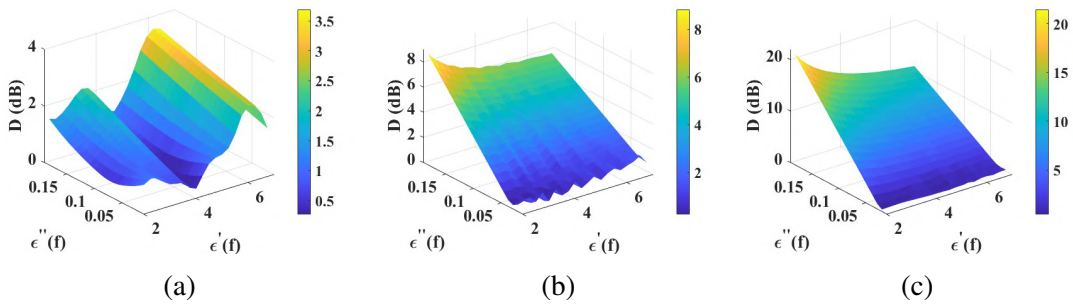


Fig. 2.12 The deviations between the simulated and measured transmissivities of sample “A” versus the possible range of real and imaginary part of permittivity at (a) 77 GHz, (b) 300 GHz and (c) 670 GHz.

Therefore, the effective permittivity is obtained by searching the minimum value of  $Dev$  integrated over the whole range of the incident angles in the defined possible range of effective permittivity values. The calculated  $Dev$  of sample A is shown in Fig. 2.12 as an example. The detail of the calculation process is represented in work [26]. The calculated effective permittivity of sample A which corresponds to the minimum deviations are  $4.02-0.035i$ ,  $2.48-0.025i$  and  $3.36-0.019i$  at 77 GHz, 300 GHz and 670 GHz, respectively. All the effective permittivities of the samples fall into the range of  $\epsilon'_r$ : 2-7,  $\epsilon''_r$ : 0.01-0.19 at three frequency bands of 77 GHz, 300 GHz, and 670 GHz.

The effective permittivity for all samples is calculated using the technique described above. The experimental and simulated results as a function of incident angle at 77 GHz, 300 GHz and 670 GHz are illustrated in Fig. 2.13. The cases ((a)-(k)) correspond to different samples explained in Table 2.4. The property information of all the samples, measured effective permittivity and measured transmissivity at normal incidence at the three frequencies under study is summarized in Table 2.4.

In Fig. 2.14, the measured and simulated transmissivities of all samples as a function of frequency within a specific operational bandwidth are shown. Due to similar observed trends for all samples, only results for two extreme samples D (metallic paint) and E (solid paint) are presented here. The effective permittivity used in this simulation is obtained from the measured transmissivity versus incident angle. Good agreement between the simulated and measured results as a function of frequency is achieved.

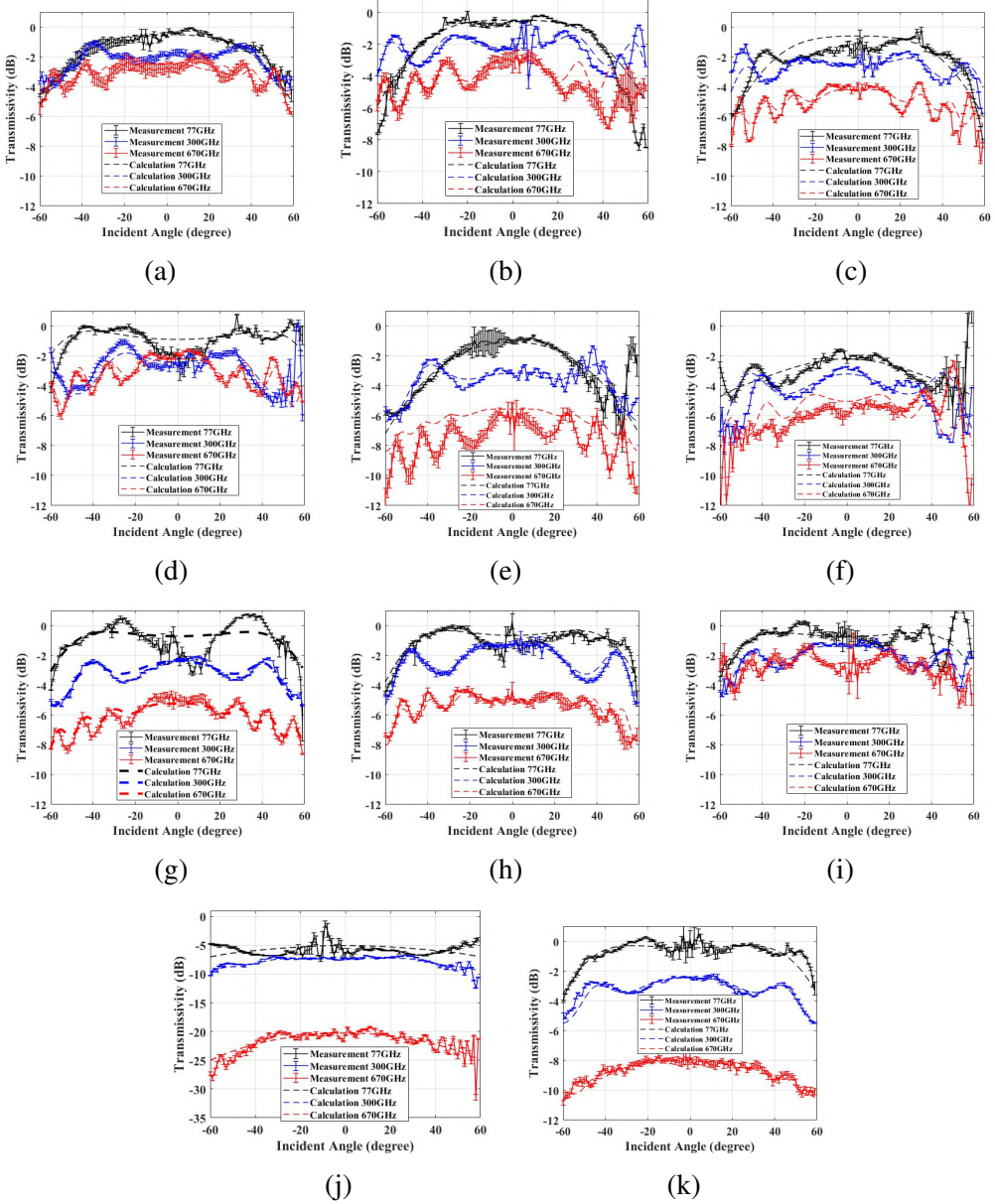


Fig. 2.13 Simulated and measured transmissivities of the automotive components as a function of incident angle using CW signal: Results in the frequency ranges of 77 GHz, 300 GHz and 670 GHz are represented in black, blue and red lines, respectively; (a)-(d) are results for bumper samples with solid paint, (e)-(f) are results for bumpers with metallic paint, (g)-(j) are results for bumpers with pearlescent paint and (k) is the result for headlight-cover.

In Fig. 2.13 and Fig. 2.14, solid lines with error bars represent the measured results and the dashed lines correspond to the simulated results. Error bars represent the standard deviations for three individual measurements.

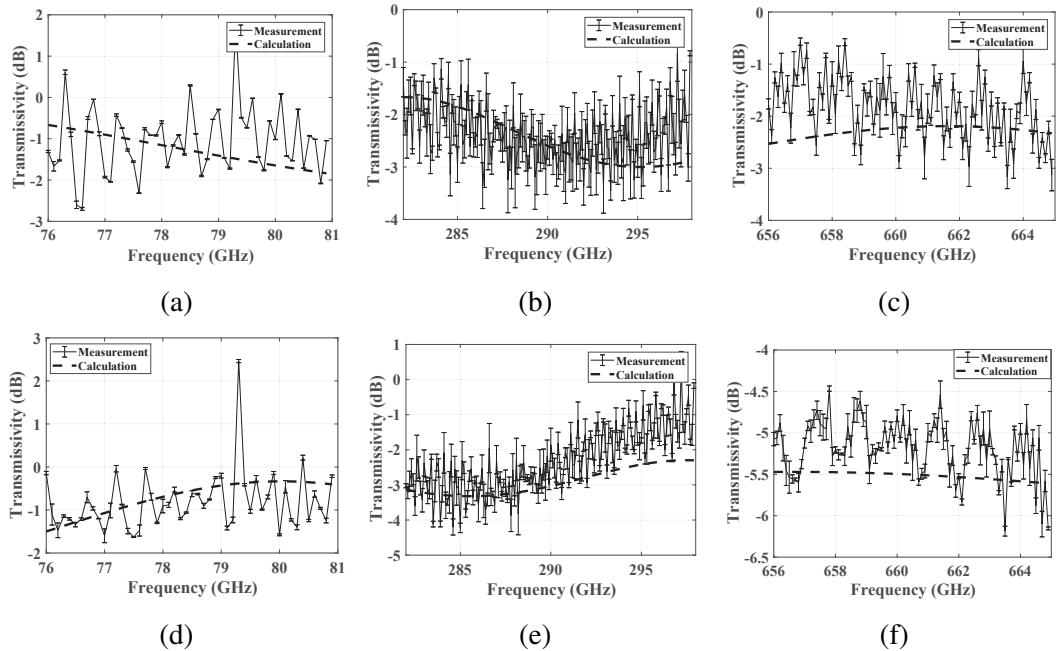


Fig. 2.14 Simulated and measured transmissivity of sample D and E vs frequency over a specific operational bandwidth: (a) (b) (c) are results for sample D at 77 GHz, 300 GHz and 670 GHz, respectively; (d) (e) and (f) are results for sample E.

The overall trend of the measured transmissivity results versus incident angle shows that typically the transmissivity decreases as the frequency increases. However, for sample D, higher transmissivity is measured at 670 GHz compared to the result at 300 GHz in the angle range of  $\pm 20^\circ$ . The increase of transmissivity at this angle is observed because the electrical thickness of sample D at 670 GHz is close to integer values of half-wavelength at  $0^\circ$  incident angle. The electrical thickness of the layer is defined as  $t_e = nd/\sin(\alpha)$ , where  $n$  and  $d$  are the refractive index and the thickness of material, respectively,  $\alpha$  is the angle between beam propagation direction and the medium boundary. A series of calculation were conducted to analyze this phenomenon in section 2.2. The extremes of the measured transmissivity as a function of incident angle are observed as expected. The electrical thickness of the sample changes with the incident angle due to different propagation path length. The constructive interference case is observed when  $\frac{N\lambda}{\sin(\alpha)} = \frac{nd}{\sin(\alpha)}$ , and  $N$  is integer factor. Shorter wavelength means shorter period of oscillations as the incident angle changes the length of propagation

path inside the medium. This observation illustrates the requirement for precision in the placement of the radar behind the covers at higher frequencies and consideration of the profile.

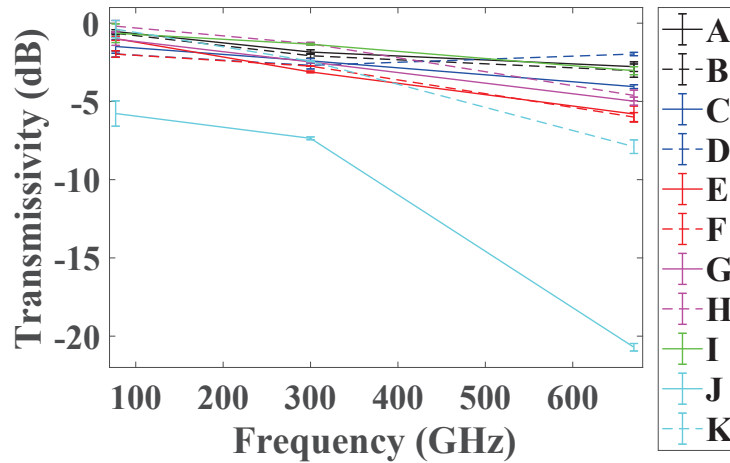


Fig. 2.15 Summary of the measured transmissivity at  $0^\circ$  incidence of the vehicle samples at 77 GHz, 300 GHz and 670 GHz.

The measured transmissivity values at  $0^\circ$  incident angle for the three frequencies are shown in Fig. 2.15. The measured transmissivity through bumper samples with solid paint (A-D) shows a difference of approximately 1 dB between the three frequencies, this is well inside the measurement accuracy. However, for the bumpers with metallic paint (E-F) and pearlescent paint (G-J), the difference between the transmissivity at 77 GHz and 300 GHz is higher than the difference between 300 GHz and 670 GHz, although the wavelength at 300 GHz is four times shorter than 77 GHz and wavelength at 670 GHz is only around two times shorter than 300 GHz. Considering sample G as an example, the transmissivity difference between 77 GHz and 300 GHz is around 1 dB which is smaller than the 3 dB difference between 300 GHz and 670 GHz.

The results of most bumper samples (except sample J) show that the transmissivity through metallic paint samples (E and F) are lower than that of solid and pearlescent paints in all the three frequency bands, even though the thickness of sample E and F are smaller than most of the other bumper samples (except A and D). Results of

sample J are observed to have more attenuation than the other samples as the substrate material of this sample is made of polyurethane (PUR) plastic, which is different to the others. Sample K is an optically transparent headlight-cover. The attenuation property of the headlight cover is at a similar level to the other samples at 77 GHz and 300 GHz, but decreases to -7.9 dB at 670 GHz, which is worse than the bumper samples with substrate material of PP.

Although precise multi-layer model of bumpers was difficult to establish because of the lack of information on the thickness of each paint layer, we still made some effort to compare the measurement results with the simulated transmissivity of multi-layer structures. To understand the transmissivity corresponding to the substrate plastic and the paint layers separately, the paint layer of sample B was removed and the transmissivity through sample B with no paint was measured.

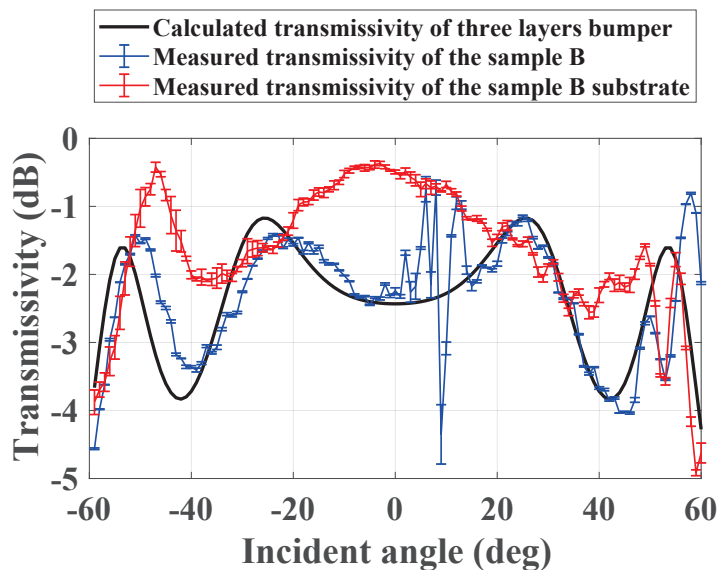


Fig. 2.16 Comparison of the simulated transmissivity of three-layer bumper and the measured transmissivity of sample B and the substrate of sample B.

Fig. 2.16 shows the measured transmissivity through sample B with paint (blue line) and without paint (red line) at 300 GHz, as well as the simulated transmissivity of three-layer bumper at this frequency (black line). The permittivity of substrate plastic layer is obtained from the measured result of bumper without paint based on

the root searching method in section 2.4.1 [26], which is calculated to be  $2.8 - 0.011i$  at 300 GHz. The permittivity of the primer and the white base coat paint are measured using TDS. The thickness of the substrate of sample B was measured at 3.62 mm. The thicknesses of primer and base coat layer are assumed to be  $25 \mu\text{m}$  and  $50 \mu\text{m}$  in this simulation, which is the maximum value in the thickness ranges shown in Fig. 2.6. Based on this permittivity and thickness information, the model of a three-layer structure bumper is established according to the theory in the theoretical section. The simulated transmissivity of the three-layer bumper of sample B is shown as a black line in Fig. 2.16, which agrees well with the measured results.

## 2.4.2 Measured Transmissivity through PC Sheets with Different Thicknesses

The theoretical model of transmissivity and thickness is explored here using PC material which could be custom designed in different thicknesses. In this section, we will present experimental results on transmissivity depending on thickness, angle of incident and frequency and compare with results of simulation shown in section 2.2 before. The analysis in this section is concentrated on 300 GHz and 670 GHz only and this is for two reasons: (i) the main purpose of this research is to investigate the feasibility of automotive radar in the Low-THz frequency range and (ii) the theoretical simulation agrees well with the measurement results at 77 GHz in the previous sections and this gives confidence to rely on the theoretical simulation for comparison purposes.

The transmissivity of PC sheets with different thicknesses are measured and compared with theoretical simulations. PC sheets used are 2 mm, 3 mm, 4 mm, 5 mm and 6 mm in thicknesses and with the sheet dimension of  $600 \text{ mm} \times 500 \text{ mm}$  which guarantees that the sample covers the 3 dB beamwidth of the signal in both paths. Fig. 2.17 shows the measured and simulated transmissivity results through PC sheets as a function of incident angle and frequency.

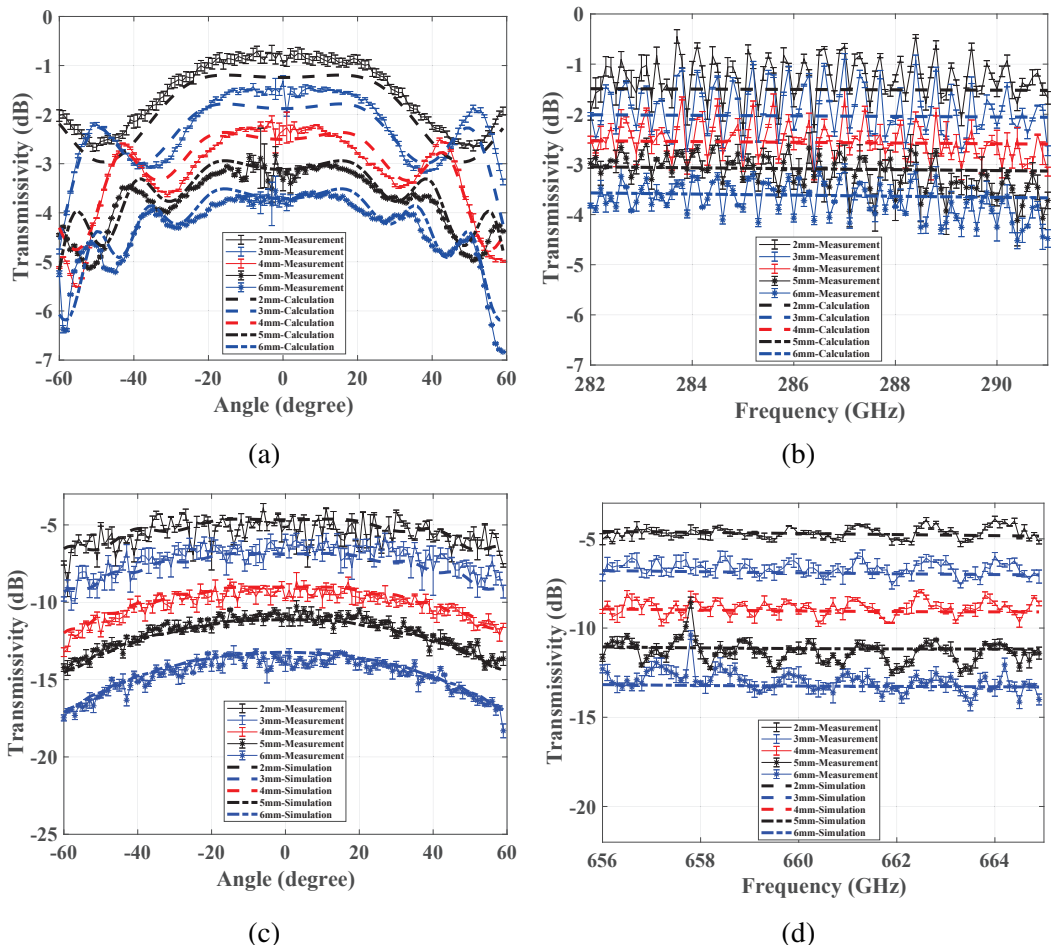


Fig. 2.17 Measured and simulated transmissivities through PC sheets with different thicknesses: (a) (b) are results at 300 GHz, and (c) (d) are results at 670 GHz.

The effective permittivity of PC sheets obtained by the root searching process are 2.5-0.032 $j$  and 2.6-0.057 $j$  at 300 GHz and 670 GHz, respectively. The measured and simulated transmissivity as a function of thickness at 300 GHz and 670 GHz are illustrated in Fig. 2.18. The simulated transmissivities through PC sheets with various thicknesses at 77 GHz are also presented for comparison. The simulated and measured results agree well in all three plots at both frequencies. As the thickness increases from 2 mm to 6 mm, the transmissivity through PC sheets decreases from -1.5 dB to -3.5 dB at 300 GHz. However, at 670 GHz, the transmissivity decreases from -5 dB to -13 dB. As discussed in section 2.2.3, smaller variations between local minima and maxima are observed when increasing thickness and frequency.

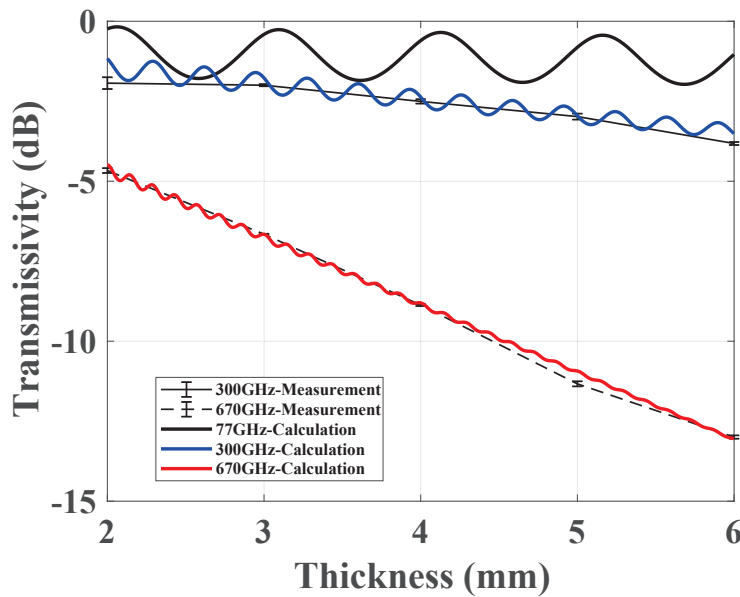


Fig. 2.18 The comparison of simulated and measured results as a function of medium thickness.

## 2.5 Conclusions

To estimate the propagation loss of potential automotive radar covers, the measured and simulated transmissivity of automotive bumper material, headlight-cover material, and also PC sheets with different thicknesses are presented at Low-THz frequencies as a function of incident angle and frequency. Measured results at 77 GHz are also shown for comparison. Good agreement is found between the measured results and the theoretical modelling results which are based on Fresnel theory and propagation matrices.

The effective permittivity of multi-layer bumpers and one-layer headlight cover are determined using the free space method. The measured results show bumpers with metallic paints have higher loss compared with solid paint and pearlescent paint bumpers and this is due to the metal composition. The losses through the bumper with a substrate composed of PUR plastic are measured, which are around 3 dB, 4 dB, and 15 dB higher than the PP plastic substrate at 77 GHz, 300 GHz, and 670 GHz, respectively. When radar sensor signals pass through the bumpers at 0° incident angle, the transmissivity

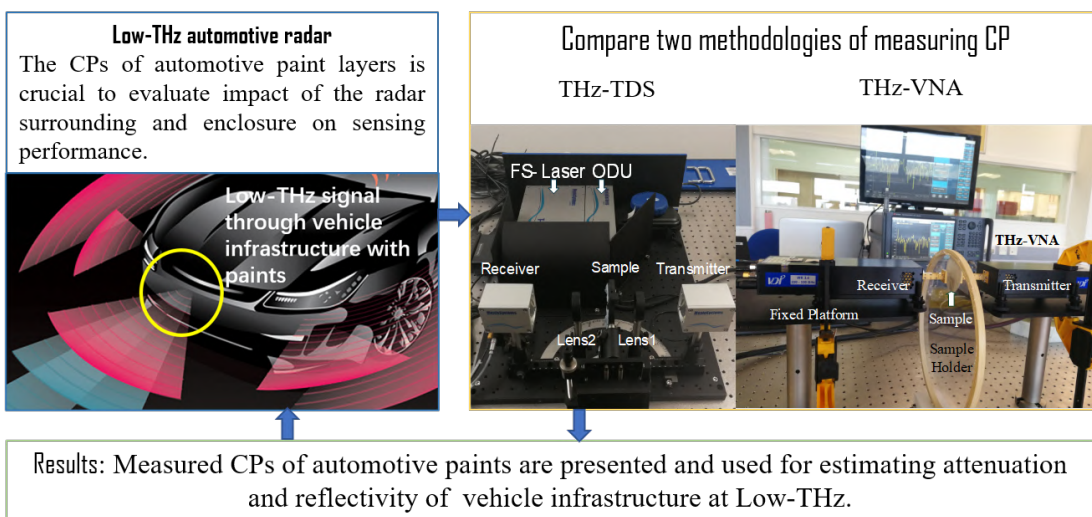
is in the range of -0.2 dB~−5.8 dB, -1.3 dB~−7.4 dB and -2 dB~−20 dB at 77 GHz, 300 GHz and 670 GHz, respectively. The transmissivity through various thicknesses of PC sheets are measured and analysed as it is the main material of headlight covers and also some other parts of the vehicle components. The results show higher losses with increasing thickness at 670 GHz compared to 300 GHz, and a decrease with a step of 0.5 dB and 2 dB is measured at 300 GHz and 670 GHz, respectively, when the thickness increases in 1 mm increments.

The results are directly applicable to automotive radar and also to wider applications in communication and other systems operating at Low-THz frequencies. Two main conclusions can be drawn to aid the industrial design of sensor cover infrastructure: Firstly, the model correctly describes the transmissivity and reflectivity fluctuations as function of signal frequency, thickness of medium and the real part dielectric permittivity of constituent materials.

Second (and obvious) conclusion is that the larger loss tangent of cover material, defined by the imaginary part of the dielectric permittivity, leads to higher absorption inside the medium and therefore high attenuation in the sensor cover. When conducting industrial design of sensor covers, the permittivity, thickness, operating frequency and placement need to be properly matched to obtain low reflectivity and high transmissivity based on the developed theoretical model.

# Chapter 3

## Automotive Paint Permittivity Estimation in Low-THz frequency



---

This chapter is intended to be submitted to the IEEE sensors journal. Author Contributions: The authors confirm their contribution to the chapter as follows: study conception and design: Y.Xiao, F.Norouzian; experiment operation: Y.Xiao, F.Norouzian; data collection: Y.Xiao, F.Norouzian; analysis and interpretation of results: Y.Xiao; manuscript preparation: Y.Xiao, F.Norouzian, E.G.Hoare, M.Gashinova, M.Cherniakov.

## 3.1 Introduction

The propagation characteristics of radar signal through vehicle infrastructure depends on electro-physical properties of a media, in particularly CP of automotive paint. In this chapter, complex permittivities of various automotive paints, which are in single layer, have been measured within the range from 0.14 to 1.1 THz with two approaches: THz-TDS and transmission measurement based on THz-VNA. The permittivities measured by VNA show good agreement with TDS results after filtering processing. The measured complex permittivities are used to evaluate the attenuation and reflection of aggregate paint, which are in multiple layer structure, with the theoretical model based on Fresnel's equation and propagation matrix. Attenuation and reflection of automotive paints with different basecoat layers are calculated and analyzed.

This chapter is organized as follows. In section 3.2, we briefly introduce the general mathematical model to extract CP values from the measured transmissivity results of TDS and VNA based on Fresnel's equation. In section 3.3, the method of fabricating the samples of solid automotive paint used in our measurement and, then, both the THz-TDS and THz-VNA experimental methodologies for estimation of CPs of single layer of paint are described. In section 3.6, the comparison and analysis of measured CPs of a number of automotive paint samples obtained by both methods is presented. Based on the permittivity properties of various paint samples, the calculated transmissivity and reflectivity of automotive paint in multilayered structures are analysed.

## 3.2 Theoretical Model

Very brief description of background theoretical model for calculation of CP using transmissivity of material is given here based on the described theory on section 2.2.2. CP is the fundamental electrical property of a material, can be considered as measure of capacitance to form an electric field in a medium made of the material [49] and

is dependent on frequency of the electromagnetic (EM) field:  $\epsilon(f) = \epsilon' - j\epsilon'' = \epsilon_0(\epsilon'_r - j\epsilon''_r)$ . The real part  $\epsilon'$  represents the ability of the medium to store the EM energy when signal passes through it, and the imaginary part  $\epsilon''$  represents the degree of EM energy attenuation inside the material [70].

According to the theoretical model presented in section 2.2.2, transmissivity is calculated by transmission and reflection coefficients which directly affected by the wave impedance  $\eta_s = \sqrt{\frac{j\omega\mu_s}{\delta_s + j\omega\epsilon_0\epsilon_s}}$  according to Fresnel's equation [38, 71]. Additionally, wave impedance  $\eta_s$  is calculated by permittivity  $\epsilon_s$  and permeability  $\delta_s$  of materials.

The permittivity can then be evaluated by searching the value which can minimize the root mean square error (RMSE) between the measured and the calculated transmissivity through the medium [72] as discussed in section 2.4.1 of Chapter 2. The experimental approaches to measure the transmissivity using setups of TDS and VNA will be explained in the following sections of 3.3.3, and 3.3.5.

## 3.3 Experimental Methodology

### 3.3.1 Automotive Paint Sample Structure

Automotive paint coating is an important part of the vehicle manufacturing process to give a smooth, glossy or sparkly look and also, to protect vehicle from UV radiation and corrosion [71, 58]. Automotive paint is usually applied in three coating layers: primer, basecoat and finally the clear coat layer. The thickness of each layer is around tens of micrometers.

The primer layer provides better adhesion of basecoat paint and the clear coat layer used for protecting basecoat paint from scratch and erosion due to weather. It is actually the basecoat which define the colour and look and is typically made of either of three paints: solid paint, metallic paint and pearlescent paint (mica). Nowadays, metallic

and mica colours are used more frequently and such paints contain aluminium or mica flakes, respectively.

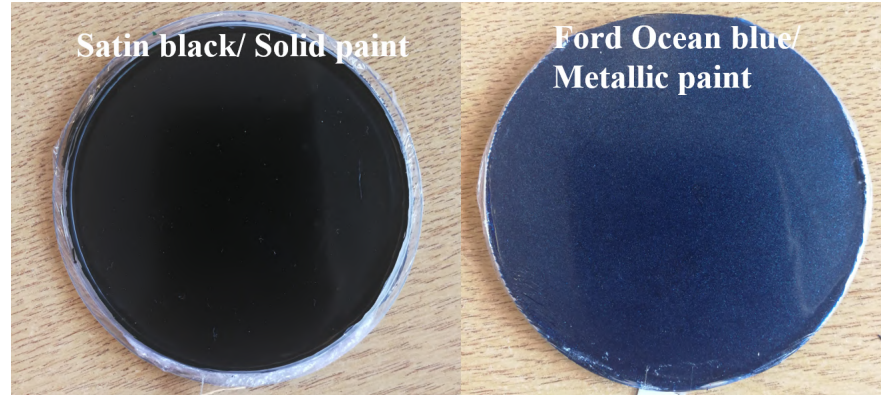


Fig. 3.1 Examples of paint samples (sample A and M in Table 3.1) after drying, which are in the color of solid black and metallic blue.

Table 3.1 Classification of automotive paint sample and thickness ( $\mu\text{m}$ ).

No.	Paint classification	$l_f$ (focused)	$l_c$ (collimated)
A	Satin black/Solid paint	$654 \pm 4$	668
B	Tool Box red/Solid paint	$571 \pm 35$	533
C	Dark Green/Solid paint	$476 \pm 11$	514
D	Domestic Gloss White/Solid paint	$466 \pm 24$	425
E	Dark Blue/Solid paint	$462 \pm 6$	442
F	Volkswagen Grey Anthracite/Pearlescent paint	$256 \pm 1$	260
G	Land Rover Epsom Green/Pearlescent paint	$371 \pm 35$	404
H	Land Rover Oslo Blue/Pearlescent paint	$501 \pm 11$	548
I	Renault Black/Pearlescent paint	$249 \pm 17$	265
J	Peugeot Diablo Red/Pearlescent paint	$586 \pm 1$	596
K	Audi Glacier White/Metallic paint	$954 \pm 52$	944
L	Hyundai Phantom Black/Metallic paint	$345 \pm 1$	370
M	Ford Ocean blue/Metallic paint	$570 \pm 5$	571
N	BMW sparkling Graphite/Metallic paint	$973 \pm 14$	972
O	Ford Tango Red/Metallic paint	$614 \pm 1$	627
P	Gold/Metallic paint	$194 \pm 7$	192
Q	Silver/Metallic paint	$200 \pm 6$	202
R	Grey primer	$432 \pm 13$	420
S	White primer	$1053 \pm 17$	1085
T	Red primer	$614 \pm 1$	627
U	Clear coat	$678 \pm 20$	670

Primers have also different colours to match with the color of basecoat and are typically red, white and grey. The grey primer is used for the basecoats with dark colors such as blue, grey and black.

In our experiment, the liquid paints of all three basecoat types (solid, metallic and pearlescent) in various colors, primer in three colors (red, white and grey) and clear coat are used for producing the paint samples.

To fabricate the paint samples for test, the liquid paint is poured onto one cling-film layer framed on a hoop, and place it on a horizontal dry surface. After seven days of drying, the samples of paint with the cling film were taken off from the hoop. Two paint samples are shown in Fig. 3.1 as the examples. Table 3.1 presents samples fabricated and their thickness measured using TDS set-ups with collimated and focused beams as explained in the next section 3.3.3.

### 3.3.2 Experimental Setup using THz-TDS

TDS is a spectroscopic technique and utilize a short THz pulse of a wideband spectrum. TDS is used widely to extract CP values of a large variety of materials [63, 58, 64], where the measured amplitude and phase information of the THz pulse transmitted through the material under test are compared with the transmission through free space, or as in majority of cases through a reference sample holder [57].

The schematic diagram of the configuration of THz-TDS and the photo of experimental setup are shown in Fig. 3.2(a) and 3.2(b), respectively. TERA K15 developed by Menlo Systems, Germany [73] is used as a spectroscopic instrument. The principle of spectroscopic systems is described in [74].

The setup shown in Fig. 3.2 corresponds to the focused beam configuration. The paint sample is placed in the sample holder, perpendicular to the beam. THz signal emission is collimated by the integrated lens inside the transmitter [75]. Two lenses - lens 1 and lens 2 have focal point distance of 5.4 cm and are aligned in the signal

path. The sample is placed at the focal point of both lenses and the illuminated area of the sample is of a 1 mm diameter. To account for the potential non-uniformity of the thickness of fabricated paint samples, the measurements were made with several positions of sample with respect to the beam, so that average thickness and variance were estimated in such a set-up.

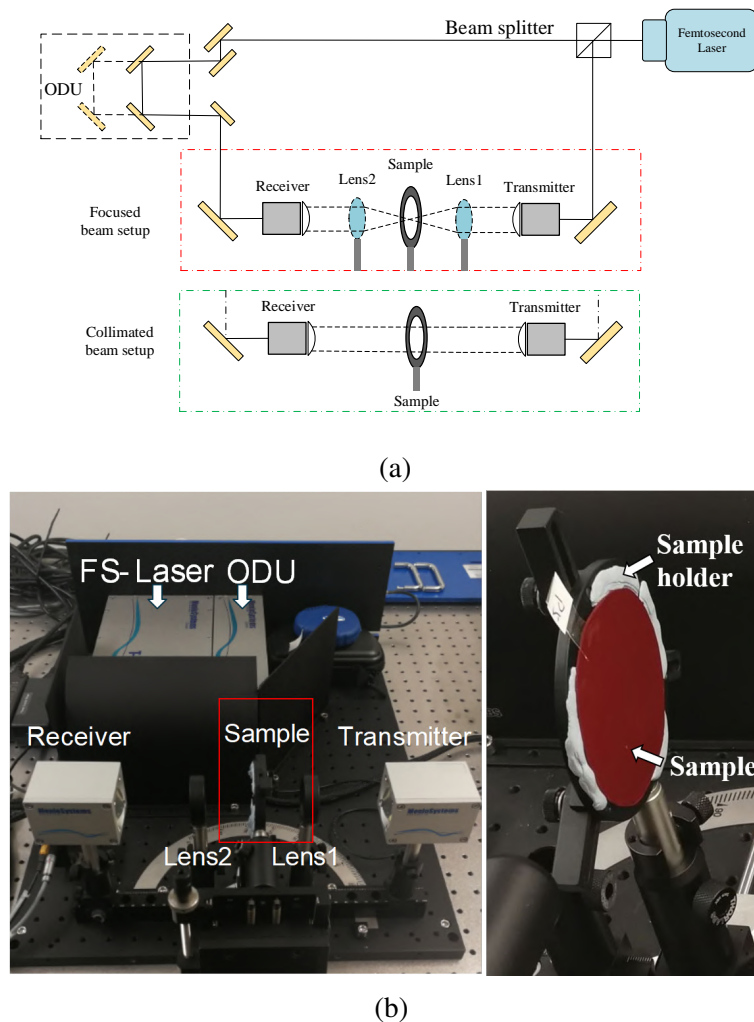


Fig. 3.2 (a) Schematic of THz-TDS experimental setup; (b) Experimental TDS setup used for measuring the CP of paints.

In the collimated beam set-up, lens 1 and lens 2 are removed which results in 5 mm diameter of the illuminated footprint. The diameter of all paint samples is around 60 mm to guarantee the beamfilling. In this set-up a single measurement was enough to estimate the effective thickness of the sample.

### 3.3.3 Estimation of Complex Permittivity and Thickness by using TDS Setup

Precise knowledge of thickness of the samples under the test is important to accurately determine permittivity of the samples. We use commercially available software TeraLyzer provided by Lytera to determine the CP [76]. This software also uses the Quasi-Space (QS) method introduced and defined in [72, 77] for accurate thickness extraction.

Here, we discuss the procedure of paint sample thickness estimation and permittivity extraction based on the results of sample K as the example.

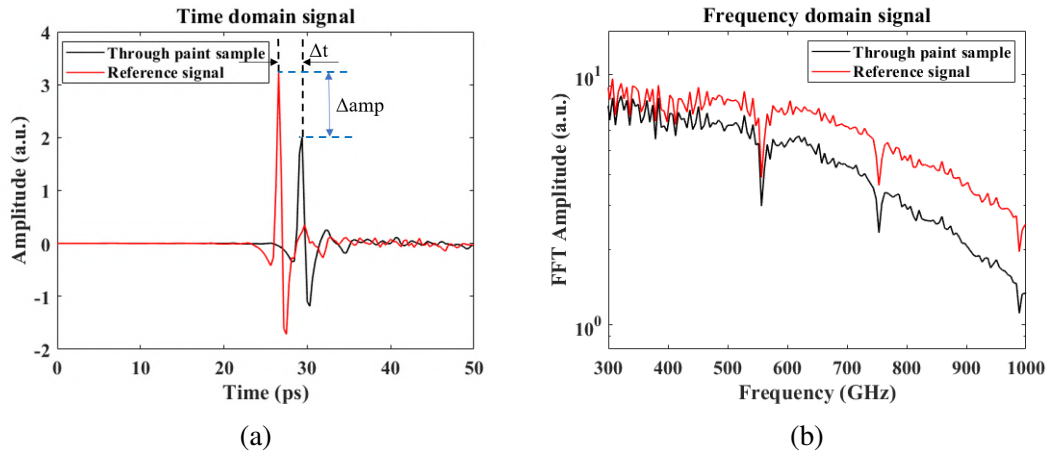


Fig. 3.3 (a) Time-domain signals obtained from the TDS experiment (Electric fields of signals through sample holder and through sample K); (b) Frequency domain signals through sample  $S_s(f)$  and through reference  $S_r(f)$ .

The received THz pulses are shown in Fig. 3.3(a), where red line corresponds to the pulse  $S_r(t)$  without the sample present in the propagation path (reference signal) and with it,  $S_s(t)$  (black line).  $\Delta t$  is the time difference between such pulses, which is used to calculate the complex refractive index as in [72]:

$$n = \frac{c\Delta t}{l_s} + n_{air} \quad (3.1)$$

where  $n_{air}$  is the real-valued refractive index of the air,  $l_s$  is the thickness of the sample and  $c$  is speed of light. Their spectral characteristics,  $S_s(f)$  and  $S_r(f)$ , obtained by a Fourier transform of the time domain signals, are shown in Fig. 3.3(b) and are used to evaluate the initial extinction coefficient of sample,  $k$ :

$$k = -\frac{c}{l_s \omega} \log \left| \frac{S_s(f)}{S_r(f)} \right| \quad (3.2)$$

The CP can therefore be calculated based on the following relationship of:

$$\epsilon' + j\epsilon'' = (n + jk)^2 \quad (3.3)$$

Inaccuracy of initial thickness measurement of the sample under test may cause the oscillations of both  $\epsilon'$  and  $\epsilon''$  [72] as shown in the Fig. 3.4. The bigger the offset of the estimated thickness from its true value, the larger will be the amplitude of such oscillations, as illustrated in Fig. 3.4(a) where  $\epsilon''$  is calculated for two values of thickness  $1006 \mu m$  and  $684 \mu m$  for the sample, which actual thickness is  $954 \mu m$  (Table 3.1, sample K). The results show that smaller oscillation in  $\epsilon''$  is observed when a thickness of  $1006 \mu m$  is used. For high accuracy of estimated thickness, it is expected that both real and imaginary parts of CP will display the monotonic behaviour.

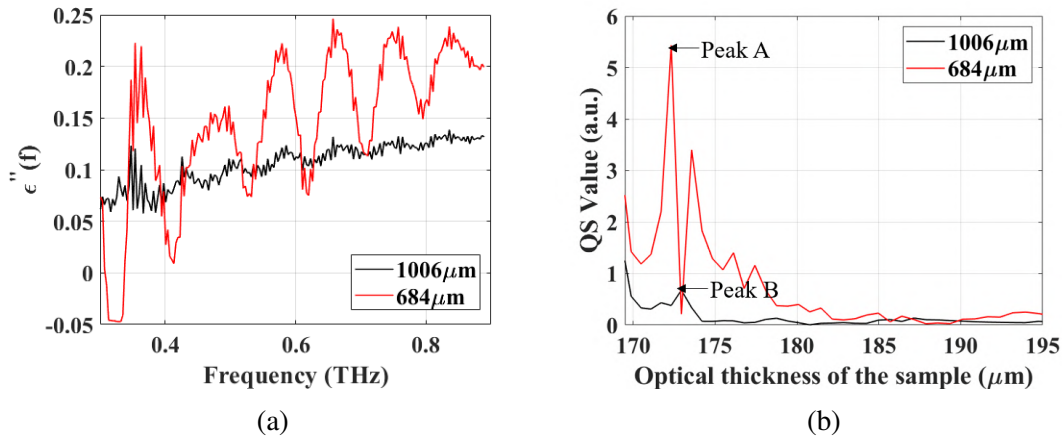


Fig. 3.4 (a) The measured  $\epsilon''$  of sample K, and (b) the corresponded QS values.

Therefore to estimate actual accurate thickness, a QS method was proposed in [77], which allows extraction of the thickness of sub- $100 \mu m$  thin samples in permittivity measurement. In this method the initial rough thickness value  $l_{init}$  is measured by a digital caliper. Then the actual thickness value is obtained by root searching procedure within the range  $l_{init} \pm 300 \mu m$  with the increment of  $30 \mu m$  in order to minimize the oscillation amplitude on the CP results.

After FFT the plot of  $\epsilon''$  would exhibit peaks corresponding to the frequency of oscillation as shown in Fig. 3.4(b), where x-axis is represented as optical thickness of the sample [77]. Higher magnitude of the peaks of QS values indicates more oscillatory behavior. In our case QS plot for  $684 \mu m$  thickness has higher peak (Peak A) compared to the results for  $1006 \mu m$  (peak B). Therefore, minimization of the QS peak value is the criterion used to obtain the accurate thickness of the sample.

Table 3.1 presents samples fabricated based on method described in section 3.3.1, and their thickness measured based on QS method using TDS set-ups with collimated and focused beams.

### 3.3.4 Experimental Setup using THz-VNA

The CPs are also measured using microwave instruments, the Keysight PNA-X [78], at Low-THz frequencies. The THz-VNA is equipped with six sets of up- and down-converters which cover the whole frequency range of 0.14 THz-1.1 THz. Transmission mode method [39] searches the CP by comparing and fitting the calculated transmissivity to the measured transmissivity.

The experimental setup is shown in Fig. 3.5. Sections of waveguides are used as the antennas for each frequency range. The characteristic of waveguides and the calculated far field distances are listed in Table 3.2.

The transmitter and receiver are aligned to maximize received power. The PNA is calibrated before each measurement to prevent the error caused by the change of

environment. The sample of automotive paint is held between tightly stretched layers of the cling film, orthogonally to the line-of-sight. The distance between two waveguide antennas is 30 mm, to guarantee operation in the far field of antennas. The beamwidth of the waveguide antenna is around  $60^\circ$ . The illuminated area on the sample is of the diameter less than 20 mm.

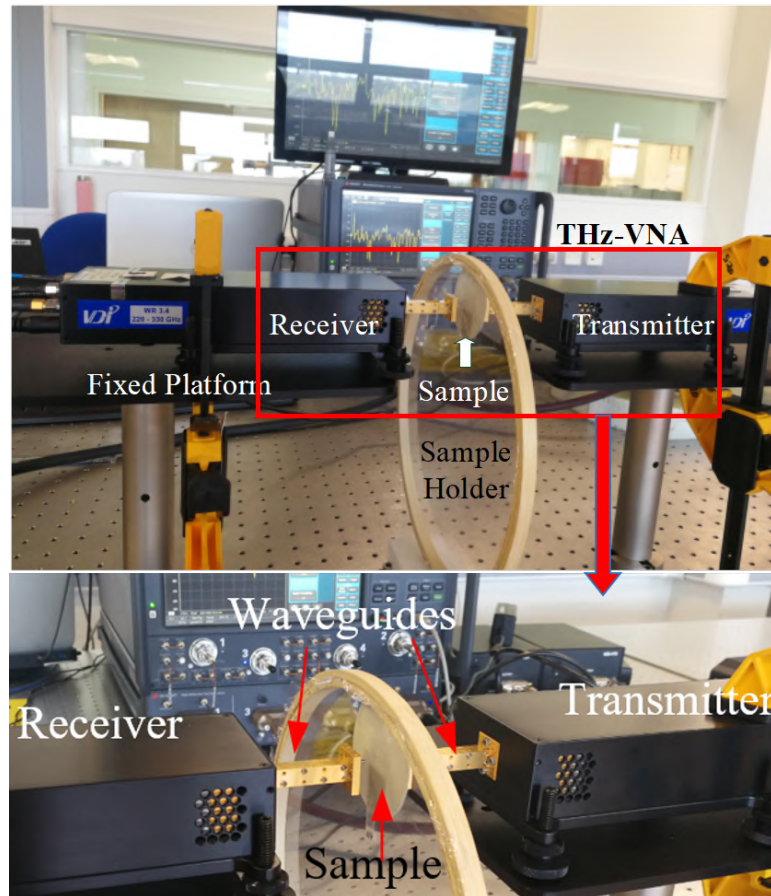


Fig. 3.5 Transmission measurement setup using THz-VNA.

Table 3.2 The apertures and farfield distances of waveguides in different frequency ranges.

Waveguide	Frequency (GHz)	Aperture (mm×mm)	Farfield (mm)
WM1295	140-220	1.295/0.6475	2.46
WM864	220-325	0.864/0.432	1.64
WM570	325-500	0.57/0.285	1.083
WM380	500-750	0.38/0.19	0.722
WM250	750-1100	0.25/0.125	0.458

### 3.3.5 Estimation of Complex Permittivity by using VNA Setup

The transmissivity is defined as the ratio of power received in presence of sample to the one without the sample:

$$T_{mea}^{VNA} = \left| \frac{S_{21}^s}{S_{21}^r} \right|^2 \quad (3.4)$$

where  $S_{21}^s$ ,  $S_{21}^r$  are the measured scattering coefficients with and without sample, respectively. The  $S_{21}^r$  is measured with the sample holder presented in the path.

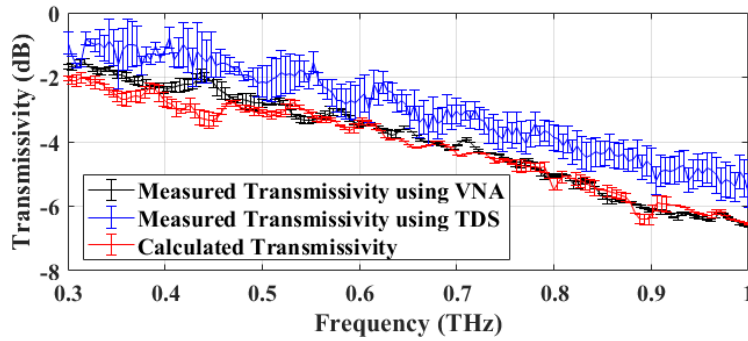


Fig. 3.6 Comparison of the measured transmissivity from VNA and TDS, ( $T_{mea}^{VNA}$  and  $T_{mea}^{TDS}$ ), and the calculated transmissivity  $T_{cal}$  which is closest to  $T_{mea}^{VNA}$ .

The CP is determined by minimization of the difference between the measured transmissivity  $T_{mea}^{VNA}$  and calculated transmissivity  $T_{cal}$ , defined by Eq. 2.9 in section 2.2.2:

$$D(\epsilon', \epsilon'') = \sum_{i=1}^M |T_{mea}^{VNA}(f_i) - T_{cal}(f_i, \epsilon', \epsilon'')| \quad (3.5)$$

where  $f_i$  is frequency of microwave signal in the range of 0.14 THz-1.1 THz, M is the number of frequency samples where transmissivity is measured. Therefore, the CP is calculated by root searching to provide the minimum value of  $D$  integrated over the whole considered frequency range. The range of permittivities can be determined by TDS results for convenience, if they are available. However in practice, any reasonable values, for instance those measured at 79 GHz [5, 6] can be used as an initial values in Eq. 3.4.

Fig. 3.6 presents the comparison between calculated  $T_{cal}$ , the measured transmissivity using TDS,  $T_{mea}^{TDS}$ , and VNA,  $T_{mea}^{VNA}$ , of sample K. The  $T_{cal}$  is calculated based on Eq. 2.9 and the CP of sample K obtained by VNA setup is plotted in Fig. 3.9.  $T_{mea}^{TDS}$  is determined as:

$$T_{mea}^{TDS} = \left| \frac{S_s(f)}{S_r(f)} \right|^2 \quad (3.6)$$

The error bar in the figure represents the measurement standard deviation (STD) of three realizations. The plots of  $T_{mea}^{VNA}$ ,  $T_{mea}^{TDS}$  and  $T_{cal}$  show a reasonably good agreement.

## 3.4 Experimental Results

In this section, the CP of automotive paints, listed in Table 3.1, are measured and results are discussed.

### 3.4.1 Measured Dielectric Properties of Automotive Paints

The CP of paints measured at 79 GHz, which is the current automotive standard frequency, can be found in [5, 6], and some typical values are shown in Table 3.3.

Table 3.3 CPs of paint layers at 79 GHz [5, 6]

Primer ( $\epsilon'/\epsilon''$ )	Clear coat ( $\epsilon'/\epsilon''$ )	Solid ( $\epsilon'/\epsilon''$ )	Pearlescent ( $\epsilon'/\epsilon''$ )	Metallic ( $\epsilon'/\epsilon''$ )
9/0.06	3.5/0.1	9.9/0.91	5.9/1.61	3.2/0.007

For all samples shown in Table 3.1, the CP results at Low-THz are obtained from three above described techniques: (i) THz-TDS with the collimated THz pulse signal (collimated TDS hereinafter), (ii) THz-TDS with focused THz pulse signal (focused TDS hereinafter), and (iii) THz-VNA transmission measurement with continuous wave signal.

The results of THz-VNA setup are processed by applying the filter to remove fluctuations of the measured CP with frequency as will be explained below. The

measured CP values of solid paints, pearlescent paints, metallic paints and both primer and clear coats are shown in Fig. 3.7, 3.8, 3.9 and 3.10, respectively. In these figures, the bluelines and solid black lines represent the real part of CP,  $\epsilon'$  (left y-axis), and the red plots and dashed black lines are for the imaginary part,  $\epsilon''$  (right y-axis).

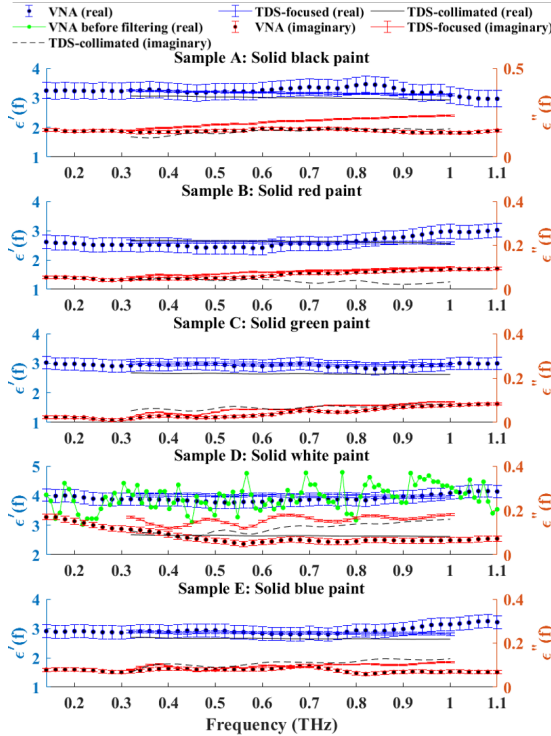


Fig. 3.7 Measured CP of solid automotive paints based on THz-TDS and THz-VNA.

In Fig. 3.7, dotted green line shows an unprocessed measured  $\epsilon'$  by VNA for the sample D, as an illustration of fluctuating trend with frequency observed for all samples. However it is expected that for non-polar materials the dielectric constant does not change significantly with frequencies unless anomalous dispersion points are encountered [53]. Because the anomalous dispersion points are not expected in the considered frequency bands confirmed by TDS results, such behavior is likely caused by the following possible issues of (1) calibration is not completely rigorous, (2) scattering, (3) sample has non-uniform thickness, therefore  $\epsilon'$  and  $\epsilon''$  obtained by VNA were filtered over the whole frequency range, where within a sliding window of specific length the average of the permittivity is calculated. The number of samples contained

in each window corresponds to the frequency band of 0.16 THz. We determine the filtering frequency band by observing the common period of fluctuation on measured CPs based on the FFT transformed value of original CPs from VNA. After such filtering procedure CPs display similar trend with results of TDS.

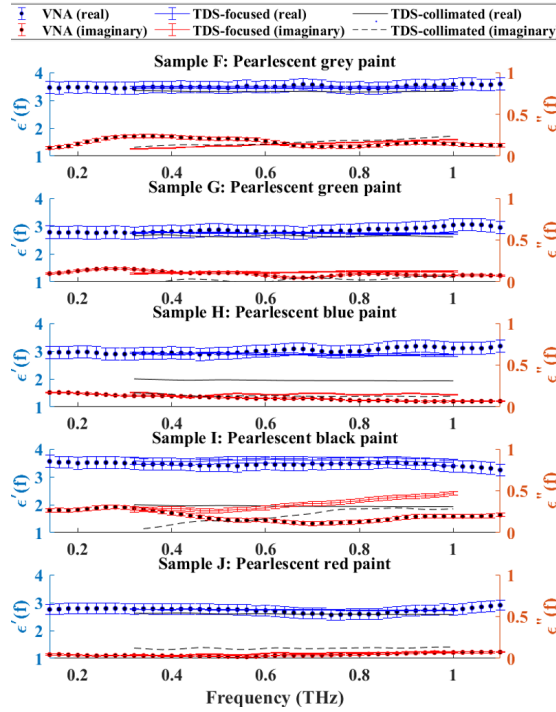


Fig. 3.8 Measured CP of pearlescent automotive paints based on THz-TDS and THz-VNA.

The  $\epsilon'$  of five considered solid paints (Fig. 3.7) is in the range of 2.5-4. The  $\epsilon''$  obtained from TDS measurements is in the range of 0.02-0.24 in the frequency band of 0.3 THz-1 THz. The  $\epsilon''$  obtained from VNA is less than 0.4 in the frequency band of 0.14 THz-1.1 THz, and bigger variation is observed at lower frequency band. The black solid paint is with the largest  $\epsilon''$  value as well as larger increase with frequency indicating higher losses compared to other solid paints, especially at higher frequencies.

The  $\epsilon'$  of pearlescent paints (Fig. 3.8) is in the range of 2.6-3.6, while  $\epsilon'$  is slightly higher, than in case of solid paints. Similar to the case of solid paints, highest loss is observed for pearlescent black paint with increase from 0.27 to 0.6 with frequency range of 0.3 THz-1 THz for TDS measurement.

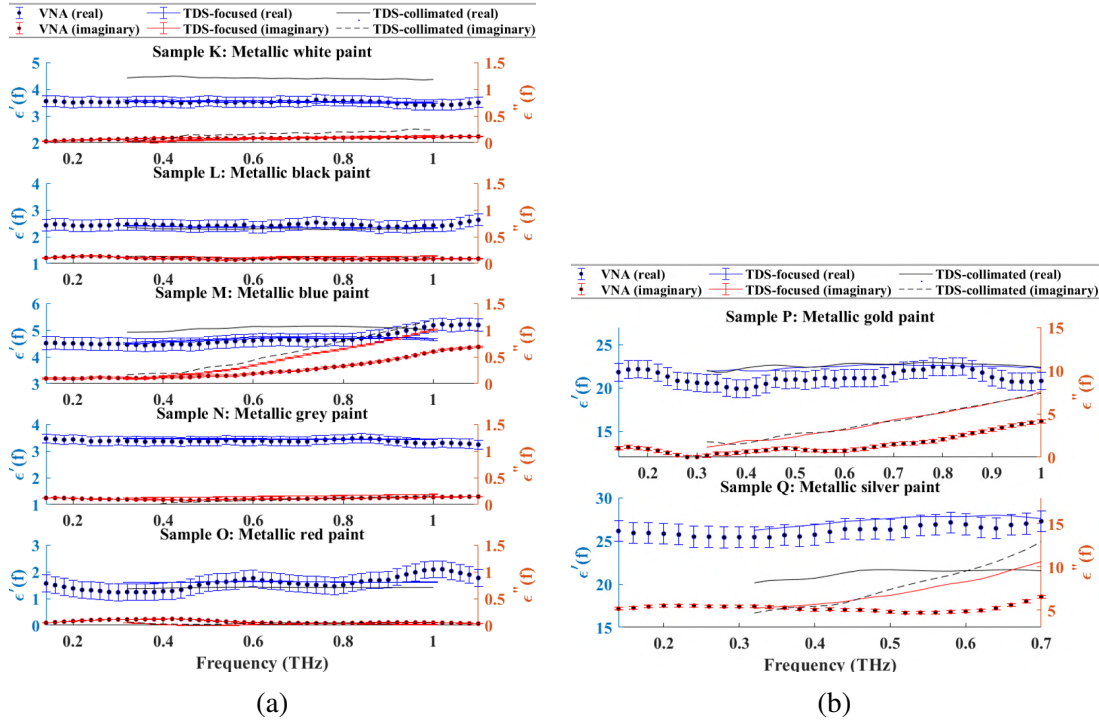


Fig. 3.9 Measured CP of metallic automotive paints based on THz-TDS and THz-VNA: (a) Results of metallic paints in color of red, white, black, blue and grey; (b) Results for bright gold and silver metallic paints.

Results for seven metallic paints are shown in Fig. 3.9. However, the dielectric constants and losses of two metallic paints - in bright gold and silver (Fig. 3.9(b)), are significantly different from other metallic paints (Fig. 3.9(a)). Indeed the real and imaginary parts of CP of the metallic paints in Fig. 3.9(a) are in the range of 1.6-5.1 and 0.01-1.29, respectively, whereas, the real and imaginary parts of CP of the bright gold (sample P) and silver (sample Q) metallic paints are in the range of 20-28 and 1.1-15, respectively. This is expected result due to higher concentration of metal for these two samples, which was also discussed in [5]. It is worth stressing that the permittivity of the metallic silver and gold paint samples are only shown in frequency range of 0.3 THz-0.7 THz and the range of 0.3 THz-1 THz due to the higher attenuation caused by these samples so that the received signal power is close to the noise floor of both TDS and VNA systems. The measured CP of clear coat and primers of three colors are shown in Fig. 3.10. The measured values of  $\epsilon'$  of primer materials are around 5.08-6.28,

while  $\epsilon''$  is basically below 0.22 obtained from TDS focused measurement. Clear coat has  $\epsilon'$  around 2.6 and the  $\epsilon''$  is below 0.1.

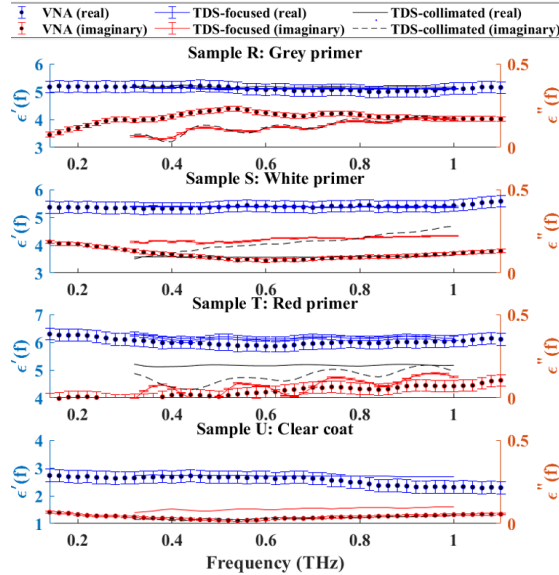


Fig. 3.10 Measured CP of primers in color of white, red and grey and clear coat based on THz-TDS and THz-VNA setups.

The measured CP obtained from VNA setup have wider variation than results of TDS. Higher measured dielectric loss and larger increase is observed in the results of the paint samples with darker colors in our selected samples. Analysis of effect of exact chemical composition of the paint on electric properties of paints is outside the scope of this study, which only gives comparative analysis of measurement techniques. The  $\epsilon''$  of majority of the paint samples show an increase with the frequency, indicating higher loss at higher frequencies, while the dielectric constant,  $\epsilon'$ , is mostly flat throughout the whole frequency range. The measured CPs obtained from TDS focused beam setup are normally higher than the results obtained from TDS collimated beam setup. For some of the TDS results (for example solid white paint and red primer sample), slight variations observed are due to the inaccuracy in the thickness estimation of the sample as discussed in section 3.3.2.

Table 3.4 Summary of the measured CP and the obtained standard deviation from three experiment setups.

Setup	Sample	$\epsilon'$	$\epsilon''$	STD ( $\epsilon'/\epsilon''$ )	Sample	$\epsilon'$	$\epsilon''$	STD ( $\epsilon'/\epsilon''$ )	Sample	$\epsilon'$	$\epsilon''$	STD ( $\epsilon'/\epsilon''$ )
TDS (focused)	A solid	3.08-3.24	0.14-0.24	0.0265/0.004	H Pearl	2.84-2.94	0.11-0.18	0.03/0.004	O Metallic	1.59-1.64	0-0.04	0.0055/0.0025
TDS (collimated)		2.88-3.06	0.1-0.17	X		1.9-2.0	0.12-0.17	X		1.36-1.42	0.02-0.06	X
VNA		2.96-3.46	0.13-0.16	0.27/0.008		2.88-3.22	0.06-0.17	0.21/0.005		1.23-2.1	0.027-0.12	0.31/0.0038
TDS (focused)	B solid	2.57-2.62	0.054-0.1	0.048/0.003	I Pearl	3.47-3.62	0.25-0.48	0.11/0.02	P Metallic	21.9-22.7	1.1-8.0	0.64/0.16
TDS (collimated)		2.49-2.67	0.02-0.05	X		3.22-3.37	0.04-0.30	X		21.8-22.9	1.5-8.0	X
VNA		2.40-3.05	0.04-0.09	0.23/0.006		3.24-3.55	0.1-0.31	0.21/0.02		19.9-22.5	0.002-4.7	1.02/0.19
TDS (focused)	C solid	2.94-3.01	0.02-0.09	0.06/0.0012	J Pearl	2.72-2.76	0.026-0.09	0.012/0.004	Q Metallic	26.2-27.9	5.15-11.67	0.37/0.49
TDS (collimated)		2.62-2.67	0.05-0.08	X		2.57-2.63	0.1-0.14	X		20.1-21.7	4.7-15.1	X
VNA		2.80-3.03	0.01-0.84	0.2/0.005		2.56-2.96	0.01-0.076	0.18/0.007		25-29	4.67-9.2	1.19/0.16
TDS (focused)	D solid	3.9-4.04	0.11-0.18	0.055/0.005	K Metallic	3.49-3.56	0.02-0.13	0.034/0.014	R Primer	5.08-5.15	0.05-0.19	0.016/0.004
TDS (collimated)		2.6-2.65	0.06-0.17	X		4.34-4.48	0.02-0.30	X		5.14-5.24	0.03-0.20	X
VNA		3.77-4.15	0.04-0.17	0.21/0.013		3.4-3.6	0.026-0.12	0.19/0.008		4.9-5.2	0.07-0.23	0.21/0.014
TDS (focused)	E solid	2.8-2.9	0.07-0.11	0.043/0.002	L Metallic	2.3-2.4	0.1-0.15	0.008/0.004	S Primer	5.37-5.40	0.18-0.22	0.014/0.003
TDS (collimated)		2.6-2.7	0.06-0.14	X		2.27-2.34	0.08-0.14	X		3.56-3.67	0.09-0.31	X
VNA		2.80-3.25	0.01-0.96	0.22/0.008		2.3-2.7	0.069-0.13	0.21/0.007		5.3-5.6	0.074-0.19	0.21/0.01
TDS (focused)	F Pearl	3.45-3.47	0.08-0.21	0.037/0.004	M Metallic	4.5-4.9	0.09-1.29	0.034/0.012	T Primer	6.06-6.28	0-0.15	0.08/0.0035
TDS (collimated)		3.43-3.47	0.08-0.2	X		4.9-5.1	0.17-1.29	X		5.12-5.23	0.05-0.20	X
VNA		3.4-3.6	0.09-0.23	0.21/0.019		4.4-5.2	0.093-0.7	0.23/0.013		5.85-6.3	0-0.11	0.21/0.034
TDS (focused)	G Pearl	2.72-2.77	0.09-0.13	0.024/0.0068	N Metallic	3.43-3.47	0.12-0.2	0.018/0.002	U Clear coat	2.67-2.75	0.07-0.10	0.016/0.0016
TDS (collimated)		2.61-2.68	0-0.06	X		3.43-3.46	0-0.18	X		1.95-1.97	0.02-0.05	X
VNA		2.7-3.05	0.04-0.16	0.22/0.008		3.2-3.4	0.08-0.15	0.17/0.005		2.27-2.7	0.02-0.07	0.22/0.0049

The measured CPs are summarized in Table 3.4, which shows the ranges over the whole frequency bands of TDS (0.3 THz-1 THz) and VNA (0.14 THz-1.1 THz). The TDS focused beam configuration provides the standard deviation below 0.11 (mostly around 0.05) for  $\epsilon'$  and 0.02 for  $\epsilon''$  and shows more reliable results compared to VNA due to absence of variations with frequency.

The THz-VNA measurement can measure CP values over a wider frequency band, which is 0.14 THz-1.1 THz, than TDS setup. The transmission method based on VNA setup might provide CP values with big variation at each individual frequency. However, THz-VNA can be utilized as an alternative of TDS for measuring CP of materials.

## 3.5 Application to Practical Muti-layer Automotive Structures

In this section, we analyze the influence of various automotive paints on attenuation and reflection of the signal in the frequency range of 0.3-1 THz. The measured CP values presented above are used for calculation. The theoretical model for calculating the transmissivity and reflectivity of multi-layer medium has been described in detail in our previous work [12].

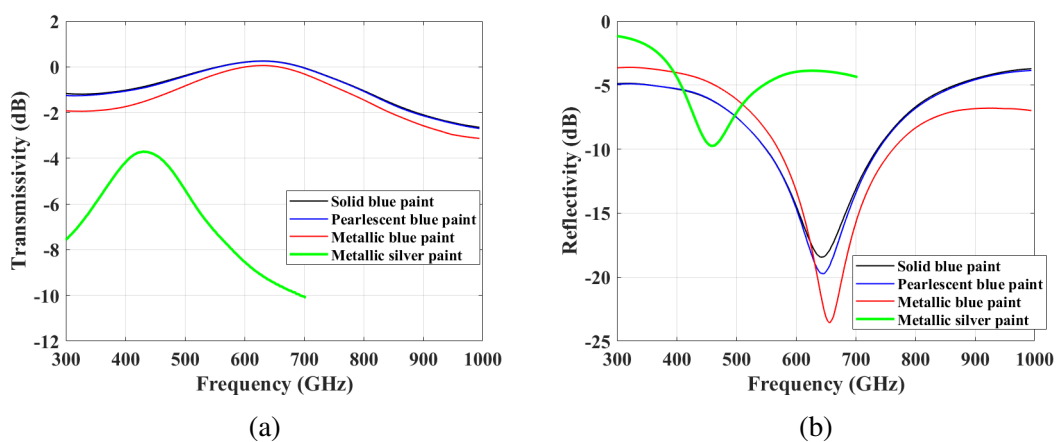


Fig. 3.11 Calclualted (a) transmissivity and (b) reflectivity of automotive paint in three-layer structure.

The calculated transmissivity and reflectivity as functions of the frequency are shown in Fig. 3.11(a) and 3.11(b), respectively. In this calculation, a paint layer with three-layer structure, as presented in Fig. 2.6 in section 2.2.4, is considered, which is composed of primer, base coat and clear coat with thicknesses of  $25 \mu\text{m}$ ,  $55 \mu\text{m}$  and  $40 \mu\text{m}$ , respectively. Samples R and U are used as the primer and clear coat. Various basecoat layers of solid, pearlescent and metallic blue as well as metallic silver which has a significant permittivity difference with other paints, are considered as the only variable in this calculation. The measured CP values obtained by TDS focused beam measurements are used for the calculation of transmissivity and reflectivity. The results of metallic silver paint only cover the frequency range of 0.3 - 0.7 THz. This has been explained in section 3.4.1 that the permittivity measurement saturates at 0.7 THz due to lower transmissivity of metallic silver paint than the others.

Transmissivity and reflectivity are functions of frequency, permittivity of material and thickness of medium [12]. Paint layers with solid and pearlescent basecoats have similar transmissivity and reflectivity. Slightly lower transmissivity and higher reflectivity are observed for the structure with metallic blue basecoat compared with the solid and pearlescent blue basecoat paint. Lower transmissivity is calculated for the metallic silver basecoat due to its higher dielectric loss. For multilayer structures with basecoats of the same color (blue) the calculated reflectivity shows the minimum within the frequency range of 0.6 THz-0.7 THz. For the metallic silver basecoat, however, the minimum of reflectivity is observed at 0.45 THz.

The permittivity, and also reflectivity and transmissivity results that are shown in Fig. 3.11 can be used when automotive radar is mounted behind suitable vehicle components which are covered by paint layers.

## 3.6 Conclusions

In this chapter, the CP of various automotive paints is investigated using three measurement setups: TDS focused beam, TDS collimated beam and VNA transmission setups. We presented the methods of permittivity measurement using VNA and TDS, as well as the thickness extraction based on QS method in TDS measurements. The measured permittivity values for three types of base coat samples in various colours, primer in three colours and clear coat are estimated and compared, and are utilized for further modelling of transmissivity and reflectivity of paint layers. The comparison between the measured CPs of various paints shows that metallic paints have higher imaginary parts of permittivity than other type of paints, and also, larger variation is observed from various samples of metallic paint whereas other type of paint show similar values for different samples. The modelling of various automotive paints showed higher transmissivity and lower reflectivity at some specific frequency ranges. These frequency ranges depend on the permittivity property of the materials and the thicknesses of mediums. For the silver metallic paint sample, the frequency band, where low reflectivity and high transmissivity are observed, differs from that of other paints due to the different CP value. The CP values of automotive paints obtained from this research is valuable for automotive industry to optimize radar placement behind suitable vehicle infrastructure with paint coatings.

We also investigate the feasibility of using THz-VNA for CP measurement. The measured results of CP obtained from VNA might show bigger variation with frequency than TDS. However, good agreement with TDS measurement is observed after filtering VNA values using a filter window corresponds to a frequency band of 0.16 THz. Therefore THz-VNA can be successfully used when TDS is not available for measuring CP of materials.

# **Chapter 4**

## **Contributions on Part I**

Part I investigated the low-THz automotive radar technology from the following two aspects: 1) the theoretical model and experimental verification of the transmissivity of low-THz radar signal through vehicle infrastructure; 2) the measurement on complex permittivities (CPs) of various commercial automotive paints. Here, we would like to give the general conclusions of this part of research from the view of industrial design and automotive radar applications.

High attenuation is a significant challenge in the application of mm-wave radar for external sensing. A robust theoretical model of the transmissivity developed for mm-wave and low-THz signals is an important tool which will allow us to understand the impact of signal parameters and environmental conditions on radar performance. Specifically, the transmissivity is the characteristic of the signal-environment interaction which can help design the vehicle infrastructure to maximize the reliability of the radar. Therefore the modeling and analysis of the transmissivity is the first contribution of this work, where good agreement between modeling and measurement has been demonstrated and therefore validated. It has been shown that the loss tangent of materials, which is defined by the imaginary part of the dielectric permittivity, leads to lower transmissivity. This is one of the key factors which need to be considered in the industrial design of the composition of vehicle components.

This assessment of the effect of CP formulates the second contribution of this research, which comes from the measurement of CPs of various automotive paints. To the best of our knowledge, we are the first to study the CP parameters at low-THz of these paints. The published values in this thesis are the key to the theoretical modeling of transmissivity and reflectivity through vehicle components.

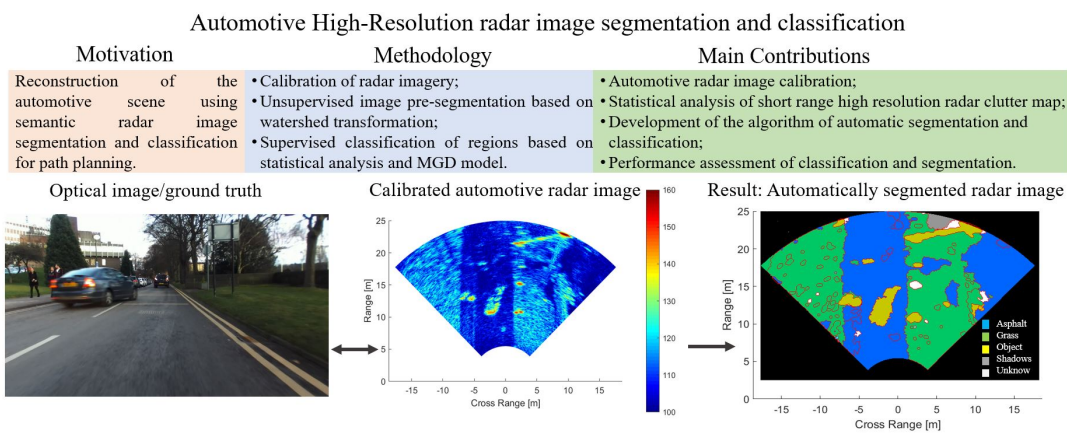
Based on the first two contributions, we are able to draw the overall conclusion on the feasibility of using sub-THz signals for automotive sensing. The comparison of transmissivity among the frequency bands of 77 GHz, 300 GHz, and 670 GHz provides non-trivial insights to estimate the capability of range measurement of the low-THz radar system.

## **Part II**

# **Image Segmentation Technique in Automotive Radar Field**

# Chapter 5

## Image Segmentation and Region Classification in Automotive High-Resolution Radar Imagery



---

This chapter has been published as: [1] "Image Segmentation and Region Classification in Automotive High-Resolution Radar Imagery," in IEEE Sensors Journal, vol. 21, no. 5, pp. 6698-6711, March 2021; [2] "Feature-based Classification for Image Segmentation in Automotive Radar Based on Statistical Distribution Analysis," 2020 IEEE Radar Conference (RadarConf20), 2020, pp. 1-6. Author Contributions: The authors confirm their contribution to the chapter as follows: study conception and design: Y.Xiao, M.Gashinova; dataset collection: L.Daniel; data pre-processing: L.Daniel, Y.Xiao; algorithm implementation: Y.Xiao; analysis and interpretation of results: Y.Xiao; manuscript preparation: Y.Xiao, L.Daniel, M.Gashinova.

## 5.1 Introduction

Image segmentation and classification of surfaces and obstacles in automotive radar imagery are the key technologies to provide valuable information for path planning in autonomous driving (AD). As opposed to traditional radar processing, where clutter is considered as an unwanted return and should be effectively removed, AD requires full scene characterization. Hence, clutter carries necessary information for situational awareness of the autonomous platform and needs to be fully assessed to find the passable areas. Based on this purpose, we would like to be the first to achieve full scene segmentation purely based on automotive radar data, and explore the feasibility of using radar as the core sensor for applications of AD or advanced driver-assistance systems (ADAS).

There is substantial research in the area of remote sensing on image segmentation, feature extraction, and classification. These are critical steps for object-based image analysis (OBIA) of synthetic-aperture radar (SAR) imagery in a wide range of applications of remote sensing, such as sea ice monitoring [79], land cover classification [80], agricultural crop identification [81] etc.

For automotive sensing to this day, however, the radar sensors have never exceeded the resolution required for traditional ADAS, which is far from that delivered by SAR images, so that image segmentation and surface classification were hardly considered in mainstream automotive radar sensing research. Therefore, the key requirements for provision of autonomous navigation can be summarized as follows: ‘radar clutter’ must be resolved (imaged), characterized (positions, extent and texture estimated to generate the ‘depth’ of scene), segmented and recognized, enabling deep scene reconstruction similar to SAR, where four main approaches are used:

- 1) The edge-based segmentation algorithms which are relatively simple and computationally effective; example algorithms are the fuzzy model and watershed transformation (WT). The fuzzy logic based techniques in remote sensing image segmentation include

fuzzy c-means clustering (FCM) [82, 83] and fuzzy stochastic estimation maximization (FSEM) [84]. The main challenge of FCM is the sensitivity to weight adjustments of adopted data attributes and the initialization process [85], and the FSEM method was limited to two classes segmentation. WT, which segments objects using closed boundaries has become the most popular edge-based segmentation methods in the remote sensing community. The WT method based on the typical gradient operator can however easily produce over-segmented areas due to image noise [86]. Therefore, the generation of gradient image is the key to improve the performance of WT which could constrain the initial edges. In this study, WT is implemented for pre-segmentation and the technical details are given in section 5.5.1.

2) The region-based methods. These are based on two basic operations: region merging and splitting. Region merging (or growing) starts from an initial region (or pixel), then merge the regions (or pixels) according to a specific homogeneity criterion which determines whether the area belongs to the growing region or not [87]. In contrast, region-splitting starts from the entire image, and then split the image into segments based on the criterion for inhomogeneity of regions [88]. The criteria used in region-based methods include the properties of spectral and spatial characteristics, shape, texture, size, prior knowledge and context of scenarios. The mathematical description of these properties is based on statistical distribution features [89], variance, Moran's I [90], and F measure etc. Typically region-based segmentation is based on either merging or splitting or combination of both techniques [91, 90]. However, finding the appropriate parameters of the criterion for judging splitting or merging of regions is a significant challenge.

3) Hybrid method (HM) could overcome the limitation of both edge-based and region-based segmentation methods. Most of the studies of HMs start from the edge-based method to create an over segmented image, and then merge the similar segments based on either homogeneity or heterogeneity of regions. The advantages of HMs are

(i) the freedom to select the methods for initial segmentation and the following region merging; (ii) less sensitivity to image noise texture.

4) Semantic methods are generally supervised approaches which allot the label to each pixel. Machine learning-based semantic methods include Neural network [92], Support vector machine [93] and Convolution Neural Network (CNN) [94] etc. Semantic methods showed encouraging results on SAR image segmentation, although require a vast amount of training data and a significant number of parameters for validation [91].

In this part of research, we proposed a HM of automatic segmentation of automotive radar images based on two main steps: unsupervised image pre-segmentation using marker-based WT, followed by the supervised segmentation and classification of regions containing objects and surfaces based on the use of statistical distribution parameters. Several distributions were considered to characterize returns from specific region types of interest within the scene (denoted as classes) in calibrated radar imagery—the extracted distribution parameters were assessed for their ability to distinguish each class. These parameters were then used as features in a MGD model classifier. Both the performances of the proposed supervised classification algorithm and the automatically segmented results were investigated using F1-score and Jaccard similarity coefficients (JSCs), respectively.

The chapter is organized as follows: Section 5.2 introduces the automotive radar dataset used in this part of research and outlines the methodology of image calibration. Section 5.3 states the procedure of distribution parameter extraction and discusses the fit errors. Section 5.4 proposes the supervised classification algorithm based on the MGD model using identified features. The effective and redundant factors for the classification improvement are determined from F1-score results of classification. Section 5.5 introduces the algorithm of automatic segmentation and discusses the results. Finally, conclusions are formulated, and the further steps are outlined.

## 5.2 Automotive Radar Image Data Collection

Here we describe the radar system used for data collection, the formation and calibration of radar imagery and the dataset used for the analysis in this chapter.

### 5.2.1 Radar System, Image Formation and Dataset

The radar system is an experimental high-resolution 79 GHz FMCW real aperture radar, designed by the University of Birmingham and ELVA-1 [95] with parameters presented in Table 5.1.

Table 5.1 79 GHz FMCW imaging radar parameters.

Parameter	Value	Units
Centre Frequency	78.5	GHz
Bandwidth	5	GHz
Transmit Power	13	dBm
PRF/PRI	232/4.3	Hz/ms
Chirp Duration	1	ms
Az. Beam Width (2-way)	1.7	°
El. Beam Width (2-way)	7.2	°
Antenna Gain	30	dBi
Polarization	VV	

The radar utilized in this part of study is monostatic, has a ranging frequency of 33.6 kHz/m and is mechanically scanned in azimuth. Range profiles are generated at equally spaced positions within the scan to form a radar image over a specified field-of-view (FoV) with an azimuth resolution dictated by the antenna beam width. The fine azimuth resolution achieved through using narrow beam imaging antennas combined with wide bandwidths/fine range resolutions provides uniquely high-resolution imagery. Let us stress here that the proposed algorithm is not only limited to the data format produced by the FMCW mechanical steering radar system discussed here but is also universal to

the other synthetic beamforming techniques such as MIMO. The universal property of this segmentation algorithm has been studied in our work [96].

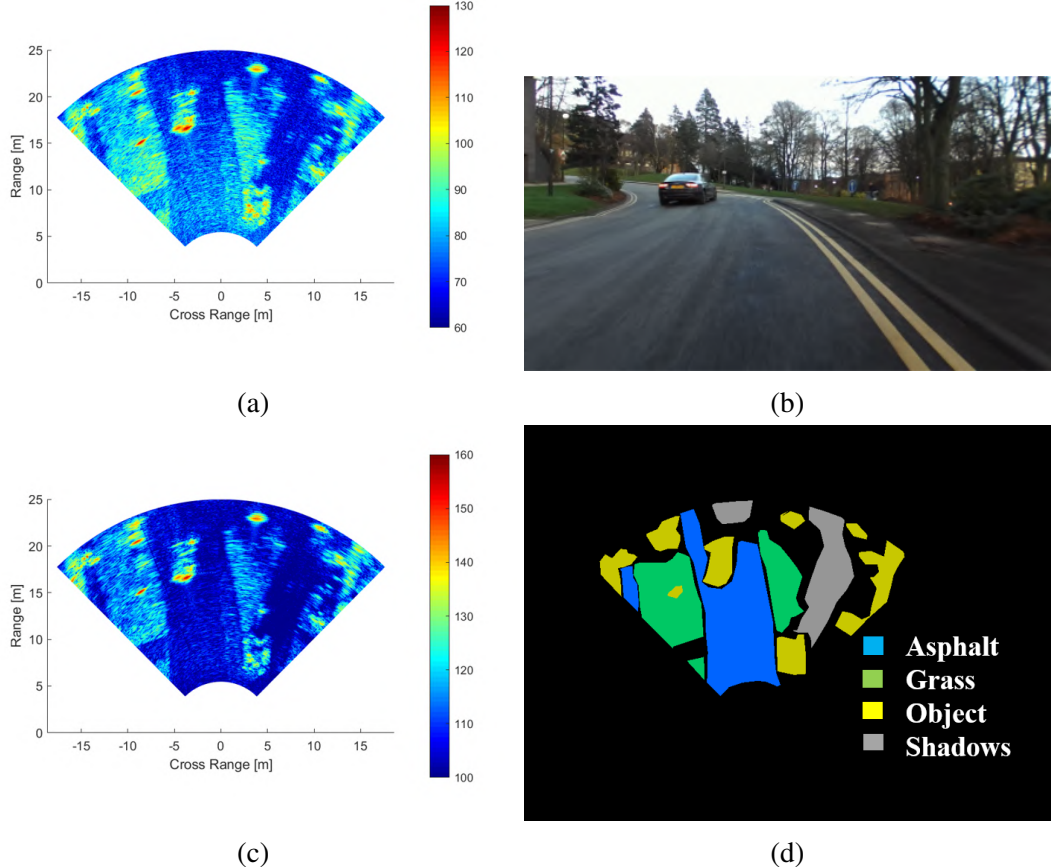


Fig. 5.1 Automotive radar image set: (a) The uncalibrated radar image in dB power values, (b) corresponding optical image, (c) calibrated radar image and (d) the color coded labeled radar image.

An example radar image can be found in Fig. 5.1(a). Fig. 5.1(b) is a corresponding optical image of the scene gathered using a Stereolabs ZED stereo video camera used for ground truth. The radar image here is expressed in uncalibrated dB power units and will be termed an image frame from hereon in. Radar videos are formed using a sequence of image frames from consecutive radar scans.

A dataset containing 330 frames of radar data is used, which was acquired with a scan rate in the order of 1 Hz with 199 azimuth range profiles within a FoV of  $90^\circ$ . The dataset was recorded from the radar systems on a moving vehicle platform

within the urban environment of the campus of the University of Birmingham, UK. The vehicle platform was driving slowly at the speed approximately  $6m/s$  with the radar data collected synchronously. The dataset contains multiple region types, including asphalt roads, grass areas, and several roadside and urban objects such as buildings, pedestrians, signposts and vehicles [97].

### 5.2.2 Radar Image Composition and Pre-processing

The mono-static radar image is composed of the backscatter returns from the scene objects, such as cars, tarmac road and grass areas shown in Fig 5.1(a) and 5.1(b). In classical radar applications, these are considered as clutter regions, obscuring detection of target objects (moving cars and pedestrians) and are subject to suppression. For path planning of autonomous platforms however, they are equally as important as targets, and segmentation and classification of all regions is fundamental. The surfaces, road infrastructure and indeed the target objects can be distinguished visually by their intensity contrast. The statistical analysis of these areas forms the basis of our classification procedure and will be discussed in Section 5.3.

For the sake of image segmentation we will treat all regions as clutter, the power return,  $P_r^s$ , within the resolution cell of a particular clutter area is governed by the following factors expressed in the form of a radar equation,

$$P_r^s \propto S(R) \cdot L_{atm}(R) \cdot L_{prop} \cdot \sigma_0(\theta_g, P, h_{rms}, L_c, \epsilon_r) \cdot A_{cell}(R, \theta_{az}, \Delta R) \quad (5.1)$$

where range dependent terms are:  $S$  is the radar response characteristic,  $L_{atm}$  is an atmospheric loss, which usually does not exceed 2-3 dB for automotive ranges,  $L_{prop}$  is the propagation loss and  $A_{cell}$  is the area of the resolution cell, governed by the antenna azimuth beamwidth  $\theta_{az}$ , and the radar range resolution  $\Delta R$ . The normalized RCS of the clutter area  $\sigma_0$  is a function of many factors including grazing angle,  $\theta_g$ , polarization,  $P$ ,

surface roughness parameters: rms surface height,  $h_{rms}$  and correlation length,  $L_c$ , and material dielectric permittivity,  $\epsilon_r$  [98].

In order to provide a more general segmentation algorithm transferrable between radar systems, all radar response characteristics should be removed from the imagery. Additionally, propagation effects should be compensated leaving solely the effects of the surface scattering. The following sub-section describes the calibration procedure.

### Image Calibration

A trihedral corner reflector (CR) with an RCS of 17.9 dBsm was placed at ground level at several ranges (within 5-60m) from the radar and imaged within a narrow FoV of  $\pm 5^\circ$ , and was measured several times. The measurement setup is shown in Fig. 5.2(a) where the average Tx/Rx height is 1.2 m, an example of the imaged CR is shown in Fig. 5.2(b).

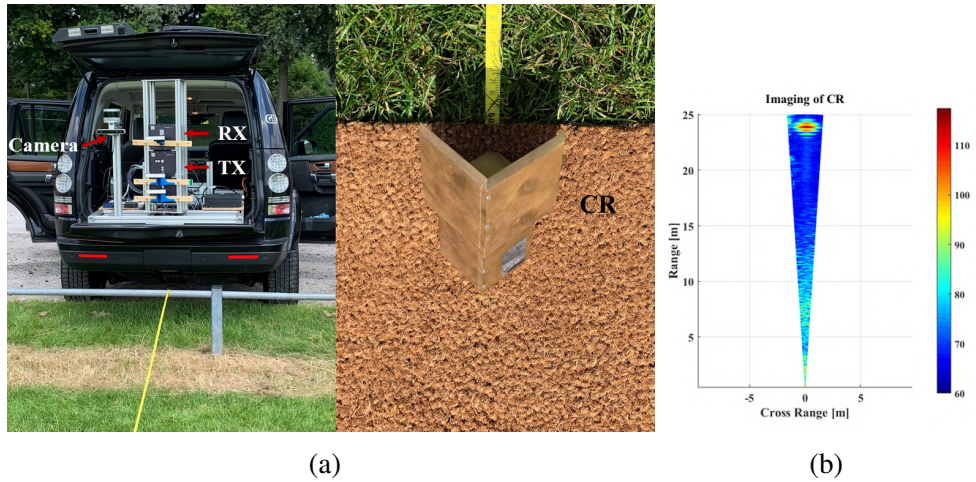


Fig. 5.2 (a) the experimental setup for measuring radar system response and propagation loss using a CR, and CR on ground, supported by a mat to prevent blockage by grass; (b) a radar image of the CR.

To determine if there was a potential effect from surface type, this was carried out on both grass and asphalt, being two surfaces of significantly different roughness. The measurement results are shown in Fig. 5.3(a) as blue and red curves. Using the radar equation and known RCS of the CR we can evaluate propagation loss as function of

range, which relates also to grazing angle [99]. The modelled free space propagation loss is shown alongside the measurement results in Fig. 5.3(a) as black curve.

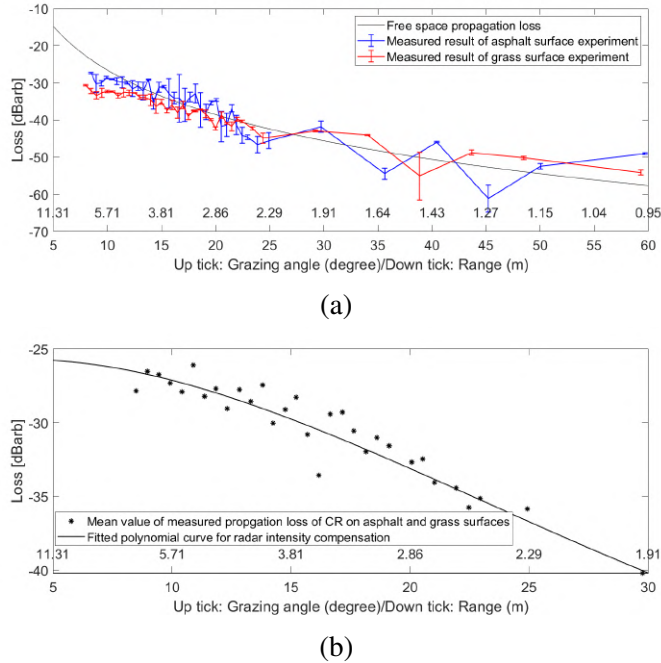


Fig. 5.3 (a) Measured loss compared with the free space propagation model; (b) Average loss calculated from the grass and asphalt measurements and polynomial loss fit (The label of x-axis shows both range information and the corresponding grazing angles for comparison).

It can be seen in Fig. 5.3(a) that at ranges  $> 15$  m, the loss follows the free space model trend. This is due to the radar IF response being flat in this region and multi-path/ground reflection playing a reduced role when considering a ground-based target. At ranges  $< 15$  m, we observe a deviation from the free space model which may be attributed to a combination of the drop-off in the radar IF response and antenna elevation pattern effects. The important conclusion is that the loss is not significantly different between grass and asphalt measurements and so a common loss curve/calibration can be used for all imagery, not specific to the surface type we are trying to determine. Therefore, to this end, a polynomial fit is calculated based on the averaged measurement results of both surfaces, and is used to apply the range response corrections as

shown in Fig. 5.3(b). The obtained 4<sup>th</sup> order polynomial was used as a close fit to our measurements:

$$L_{prop}^{fit} = -5.7 \times 10^{-6}R^4 + 0.001R^3 - 0.05R^2 + 0.36R - 26.4 \quad (5.2)$$

Compensation of the radar return w.r.t. range was applied to each range profile within the radar image frame. Fig. 5.4 shows an example of a range profile before and after the compensation. This effect is shown across all classes of surface in the compensated radar map of Fig. 5.1(a) which is shown in Fig. 5.1(c).

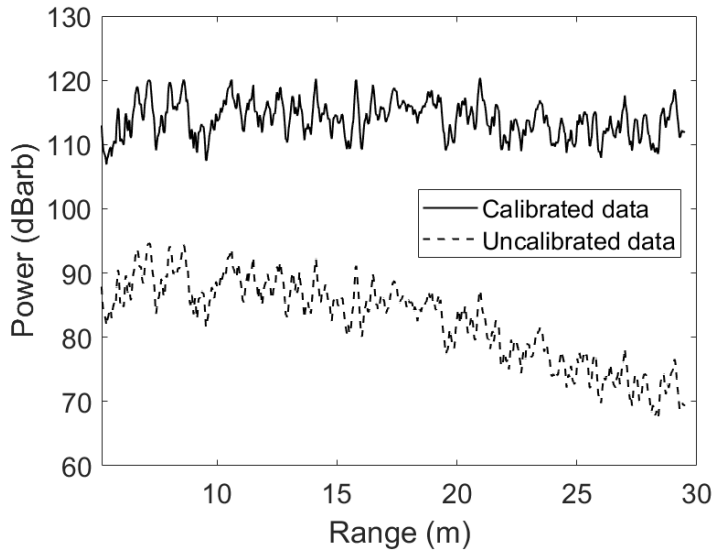


Fig. 5.4 Comparison of uncalibrated and calibrated radar range profiles.

### Backscatter Coefficient

The sheer variation of grazing angle shown on the x-axis upper scale in Fig. 5.3 is specific to the short-range topology, distinguishing it from other radar imaging systems such as airborne and spaceborne synthetic aperture radar. This variation in grazing angle implies a variation in the rough surface backscatter coefficient  $\sigma_0$  which in general can be split into 3 regions [100]: linear increase at small grazing angles, plateau at intermediate grazing angles and exponential increase at high grazing angles. The true

position and prominence of these transitions are radar and surface specific. Thus, after range loss compensation (Fig. 5.4) we should either remove the influence of the grazing angle on the normalized RCS of the clutter, or pre-segment image into regions in range where we expect a negligible variation of  $\sigma_0$ . The former requires a priori knowledge of the terrain, while for the latter we need to know the behavior of  $\sigma_0$  for the chosen classes to define range regions of similar returns. The calibration of range profile indicates that the last two terms of Eq. 5.1,  $\sigma_0$  and  $A_{res}$ , must have compensated each other. To explain this effect we have first modelled backscatter coefficient as function of grazing angle using Integral Equation Method [101], which in [102] has shown good agreement between measured and modelled results for asphalt at 94 GHz.

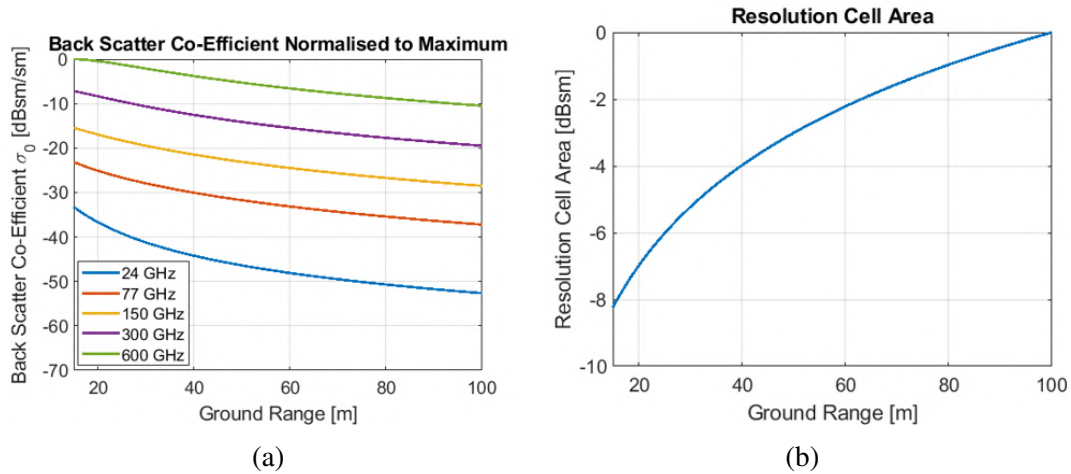


Fig. 5.5 (a) Back scatter coefficient as a function of frequency and range for a rough asphalt surface; (b) resolution cell area as a function of range for experimental radar setup.

Fig. 5.5(a) shows that simulated backscatter coefficient for multiple frequencies drops as the grazing angle reduces. In Fig. 5.5(b) a plot of the resolution cell area  $A_{res}$  (in dBsm) calculated using radar parameters (Table 5.1) and elevation above the ground. Fig. 5.5 therefore highlight the fact that for the real-aperture imaging radar an increase in resolution cell size with increase in the range counteracts the falloff in the normalized RCS. It should be noted that this discussion of  $\sigma_0$  relates to our average received power level and the ability to look further ahead of the vehicle, though at the

expense of cross-range resolution. It does not account for statistical variations in the return power between individual resolution cells, which may vary with grazing angle as the scattering mechanism changes. This potential statistical variation with range will be discussed in Section 5.3.

### 5.2.3 Image Format and Data Labelling

Now the data has been described, we discuss its labelling for use in examining potential features for supervised learning. For path planning, we need to distinguish between tarmac, other kinds of terrain, roadside objects and road actors (targets). In terms of image segmentation, this represents the classification into four broad classes such as tarmac (e.g. asphalt), non-tarmac surface e.g. grass (requiring a vehicle response to transit from tarmac), shadow and most general-target object regions, which incorporate all impassable obstacles such as buildings, vehicles, streetlights, traffic signs and trees, which generally have a higher RCS in the imagery. Shadow regions behind objects are of particular interest as their identification and subsequent estimation of shadow depth can provide indirect information about an object's height. Shadow-like regions will also be formed from regions of very low backscatter, such as surface water. It should be noted that the methodology proposed in this study is not limited to these chosen classes. All radar images are labelled using the labelling tool of Liblable [103, 104]. The tool operates for optical images labelling and so a raster image (RGB image) of the radar scan must be used, not the raw range-azimuth data; corresponding video imagery guides the labelling. Thus mapping between two data representations is required to perform the labelling and corresponding radar data extraction. The representations are: the radar range-azimuth map pixels ('resolution cells') converted and plotted in Cartesian coordinates in a Plan Position Indicator (PPI) representation and the radar raster image pixels with three color channels (defined as "rixels" which pertains to RGB image instead of radar data format). The relationship between resolution cells

and rixels is shown graphically in Fig. 5.6. A full description of the transformation may be found in [95], it is very specific to the real aperture radar coordinate map and its representation and is summarised in Section 5.3.1. The labelled image of the radar frame in Fig. 5.1(a) is shown in Fig. 5.1(d), where the pixels of the radar raster image belonging to a specific class are identified by the same color. The pixels of areas which could not be associated with one of four classes in the optical image due to restricted visibility or uncertainty are shown as black background in the labelled image. These will be treated as belonging to an “unknown” class, which can then be refined in advanced context-based and association approaches.

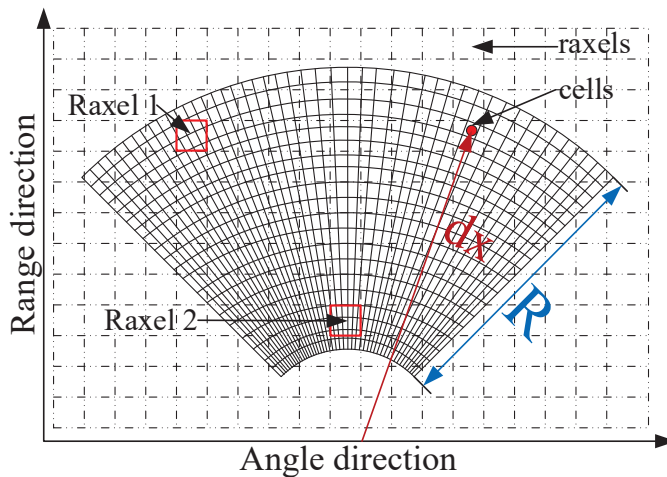


Fig. 5.6 Relationship between rixels of rasterised radar images and radar map (resolution) cells.

## 5.3 Region Statistical Properties and Feature Extraction

The distribution parameters of the labelled radar clutter are extracted and analyzed to determine potential use as feature vectors in the automatic segmentation and classification procedure. In order to determine the features which provide the greatest

contrast between region types, distribution fits are made to the probability density histograms of both the radar absolute intensity values,  $V_{intensity}$  and the dB-power values,  $P_{dB}$ . Weibull and log-Weibull distributions have been widely used in modelling of ground clutter [105, 106]. Both distributions are considered to model radar intensity values, and logarithmic power values. Rayleigh and Rice distributions are considered as reference fits for Gaussian-like clutter and returns consisting of strong components indicating presence of a target. This relationship between Rayleigh and Rician distributions could be mathematically represented as: if the variable  $V = \sqrt{X^2 + Y^2}$  where  $X \sim N(v\cos\theta, \sigma^2)$  and  $Y \sim N(v\sin\theta, \sigma^2)$  are independent normal random variables ( $\theta$  is any real number), then  $V \sim Rice(|v|, \sigma)$ , and Rayleigh is the special case of Rician distribution that  $V \sim Rayleigh(\sigma)$  when  $v = 0$ . In the following section of 5.3.2, this relationship is used in the analysis of intensity distribution feature as the variables of X and Y refer to the I and Q components of radar signal, and the variable V refers to the intensity value.

The definitions of the PDFs of these four distributions are given as:

$$f_{weibull}(x; \lambda, k) = \frac{k}{\lambda} \left( \frac{x}{\lambda} \right)^{k-1} e^{-\left(\frac{x}{\lambda}\right)^k}, \quad (5.3)$$

$$f_{log-wei}(x; \lambda, k) = \frac{k}{\lambda} \left( \frac{\ln x}{\lambda} \right)^{k-1} e^{-\left(\frac{\ln x}{\lambda}\right)^k}, \quad (5.4)$$

$$f_{rayleigh}(x; c, \sigma) = \frac{(x - c)}{\sigma^2} e^{-(x - c)^2 / (2\sigma^2)}, \quad (5.5)$$

$$f_{rice}(x; c, \sigma, v) = \frac{(x - c)}{\sigma^2} e^{\frac{-(x - c)^2 + v^2}{2\sigma^2}} I_0\left(\frac{(x - c)v}{\sigma^2}\right), \quad (5.6)$$

where  $x \geq 0$ ,  $f_{weibull}$ ,  $f_{log-wei}$ ,  $f_{rayleigh}$  and  $f_{rice}$  are PDFs of Weibull, log-Weibull, Rayleigh and Rice distributions, respectively;  $k$  and  $\lambda$  are the shape and scale parameters of Weibull and log-Weibull distributions;  $c$  and  $\sigma$  are the location and scale parameters

of Rayleigh and Rice distributions;  $v$  is the shape parameter of Rice distribution which gives the distance between the origin point and the center of the bivariate distribution.  $I_0(z)$  represents the Bessel function of the first kind with order zero. Rayleigh distribution with  $\sigma_{Rayleigh} = \lambda_{Weibull}/\sqrt{2}$  is the special case of Weibull distribution whose shape parameter  $k = 2$ .

### 5.3.1 Methodology for Extracting Distribution Feature

Initially, we need to extract data from regions where a statistically meaningful assessment can be made.

As the image labelling is performed in raxel space on the raster image, (Fig. 5.6), the initial task is to map these labelled class regions to their appropriate resolution cell values in the corresponding radar map. The azimuth dimension of each cell depends on its range. Therefore, raxels in the labeled image at different ranges correspond to a different number of cells in azimuth, e.g. raxel 1 and raxel 2 shown in Fig. 5.6. A raxel consists of  $\frac{c_{nr}}{r_{nr}}$  cells in range direction, where  $c_{nr}$  is a number of cells and  $r_{nr}$  is the number of raxels within a region of  $R$  extent in range. In the case of physical aperture beamforming the relationship between the sizes of raxels and cells in the azimuth direction is a function of distance  $d_x$ . In the azimuth direction, the number of cells corresponding to one raxel is,  $round[\frac{c_{na}R}{2Ac_{nr}d_x\sin(0.5^\circ)}]$ , where  $c_{na}$  is number of azimuth positions in the FoV of  $A^\circ$ . The analysed radar frames are truncated between ranges of 5-25 m, thus  $R=20$  m. The FoV  $A = 90^\circ$ ,  $c_{nr} = 668$  and  $c_{na} = 199$  ( $0.5^\circ$  azimuth step between range profiles). The rasterised image resolution gives,  $r_{nr} = 308$ , so one raxel consists of  $3 \times 2$  cells at the range of 5 m and  $3 \times 1$  cells at the range of 25 m [95]. In order to simplify the process of cell extraction, we disregard this difference and take the larger  $3 \times 2$  cells for each raxel whatever the range to the raxel. This guarantees all cell intensities of the ROI are extracted, though some will be extracted multiple times.

To remove multiple counts, the co-ordinates of the extracted cells are compared, and repeats are discarded.

It should be noted that the transformation between rixels and cells may be simplified (potentially 1-to-1) if the data was labelled on a rasterized rectangular range-azimuth radar plot (B-scope). The choice to label on the PPI was made due to the direct visual equivalence between this and the ground truth camera imagery, which aids the labeling process.

As discussed in section 5.2.2 it is important to investigate variation of statistical characteristics for each class as a function of grazing angle. The grazing angle across the truncated image area varies from  $11^\circ$  to  $2.3^\circ$  and at ranges  $>25$  m the grazing angle variation is insignificant. Due to the significant changes in the grazing angle, range segmentation into regions of 5 m extent will be performed.

Class datasets extracted from all available radar frames are further divided into arrays of size 1000 to produce statistically meaningful histogram plots using a consistent number of intensity values for investigating each class.

### 5.3.2 Distribution Fitting to Region Intensity Statistics

Fig. 5.7 presents exemplar histograms of I and Q components, and the radar intensity values for the four region classes. Fig. 5.7(a), 5.7(b) and 5.7(c), 5.7(d) show that the components of the returns from asphalt and shadows area are distributed normally with zero mean, which justify use of Rayleigh and Rice distributions for their intensity distribution analysis (Fig. 5.7(i), 5.7(j)). However, the I and Q components of grass and objects areas shown in Fig. 5.7(e), 5.7(f) and 5.7(g), 5.7(h), deviate from normal distribution and the histograms of intensity values in Fig. 5.7(k) and 5.7(l) are better fit by a Weibull distribution. Only radar intensity values are discussed here for feature analysis as the phase information is found to show limited effects on the feature differentiation based on our study.

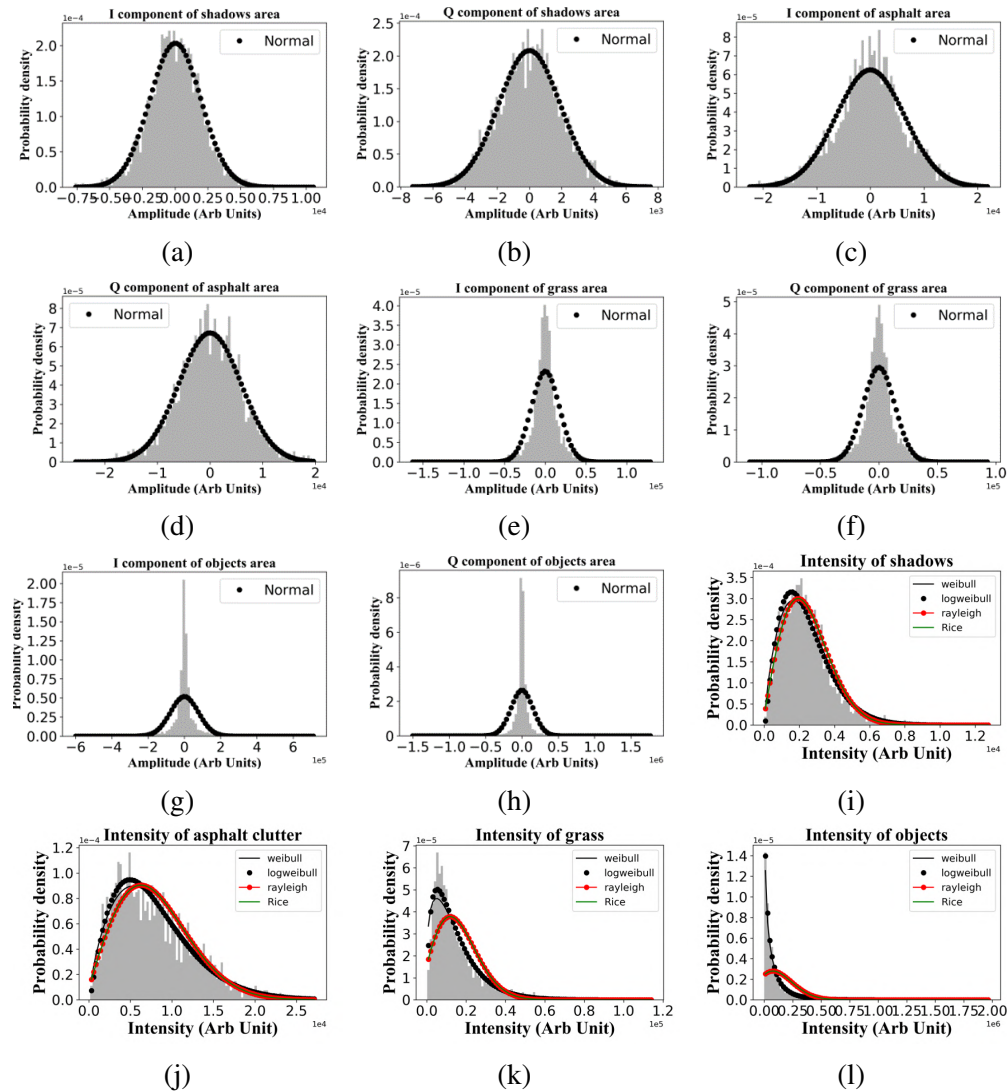


Fig. 5.7 The probability density histogram plots and distribution fits of I and Q components (a)-(h) and  $V_{intensity}$  (i)-(l), for the four classes.

The scale ranges of  $V_{intensity}$  (horizontal axes) increase successively from shadows to asphalt to grass, with highest values corresponding to “object” class. The probability density scales (vertical axes) reflect the increasing spread of intensities for these classes with higher median values.

To estimate the intensity histogram fit errors, the normalized RMSD will be used, which averages the individual RMSDs over all histogram bins:

$$NRMSD = \frac{1}{N} \sum_{n=1}^N \frac{\sqrt{(v_{PDF}^{(n)} - v_{hist}^{(n)})^2}}{|v_{hist}^{(n)}|} \quad (5.7)$$

where  $N$  is the number of bins,  $v_{PDF}$  and  $v_{hist}$  are the PDF fit value (center of the histogram bin) and the histogram value of each bin respectively.

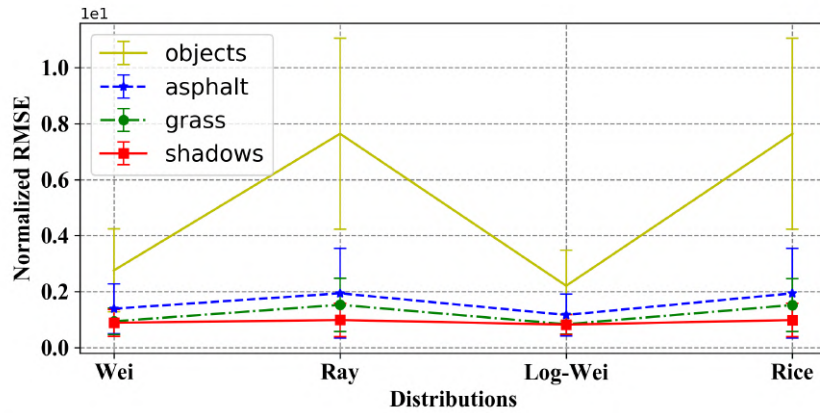


Fig. 5.8 Results of NRMSDs between PDF fits and the density histograms of intensity values extracted from the four class region types.

The NRMSD results are shown in Fig. 5.8, in which the error bars represent the standard deviation of the fit errors, estimated from fits to all instances of the class regions in the labelled dataset. The result confirms observations in Fig. 5.7 that Weibull and log-Weibull have smaller fitting error and deviation than Rayleigh and Rician distributions for all four classes. Also the smallest deviation is shown for the shadows and largest for the object class which are intuitively obvious results as the latter is very different from the traditional distributed clutter, while the former should be close to the noise floor of the receiver due to fundamental absence of reflections.

We should stress here, that while finding the ‘correct’ distribution is important task for characterization of radar returns and essential for understanding of the underlying physical processes, it is not our goal—we want to compare parameters of the same

distribution when applied to different classes to determine if there is sufficient parameter contrast to discriminate and classify an ROI within the image. The Weibull fit distribution parameters extracted from  $V_{intensity}$  for the four region types are shown in Fig. 5.9. Log-Weibull is omitted due to its similar fitting performance, Rayleigh and Rician are omitted due to their poorer fitting performance and thus greater variations in distribution parameters for a given class. Each point represents the mean value of the specific parameter evaluated for all areas of the same class in our dataset within a prescribed range group (discussed in Sections 5.2.2 and 5.3.1), the error bar represents the standard deviation. We draw the following conclusions 1) object areas show significant difference when compared to the other classes; 2) most parameters show a monotonic trend of change with increase of range; 3) for all clutter classes, except object, Weibull shape parameter  $k$  is close to 2 which shows that conventional clutter returns are close to Rayleigh distribution; 4) There are large overlaps between feature parameters extracted from areas of asphalt, grass and shadows and significant variation in parameter values for the object class. This will result in classification confusion when using distribution parameters derived from the  $V_{intensity}$  data representation.

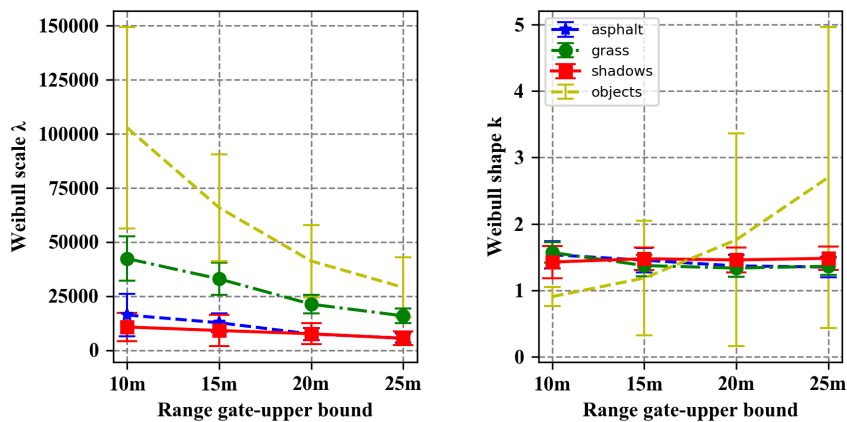


Fig. 5.9 The distribution parameters obtained from Weibull distribution fit of  $V_{intensity}$  as a function of range gate.

Next, we will estimate the distribution of class region statistics from both uncalibrated and calibrated dB-power radar maps to determine if this can improve parameter contrast.

### 5.3.3 Distribution Fitting to Uncalibrated and Calibrated Region Power Statistics

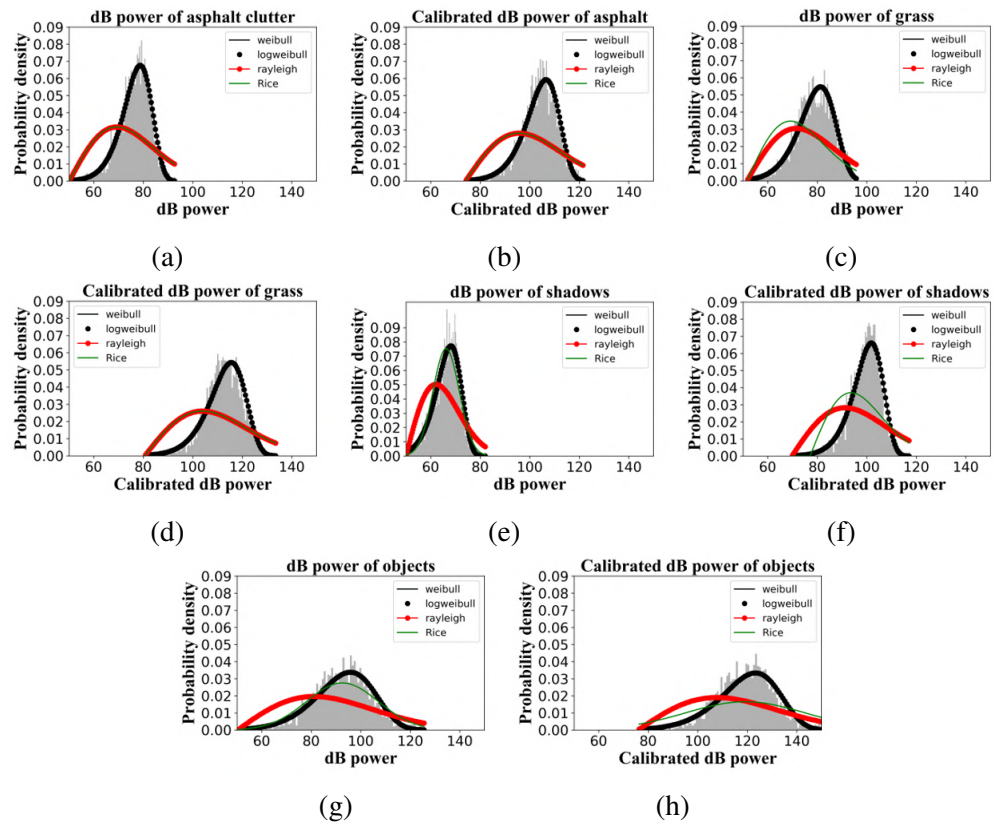


Fig. 5.10 (a)-(h) Density histograms and PDF fits for uncalibrated (left column) and calibrated (right column) radar map dB-power values.

Corresponding density histograms and PDF fits for exemplar region dB-power statistics,  $P_{dB}$ , are shown in Fig. 5.10. Shadow has the smallest variation of radar power compared to other classes, as it is defined by the electronic noise of radar transceiver rather than any reflected signal. Comparison of the histograms in Fig. 5.10(c), 5.10(d) and 5.10(e), 5.10(f) show that grass area returns follow a slightly wider bell shape distribution than that of asphalt, which can be explained by wider deviations in the

height profile of grass within regions. The areas containing target return demonstrate a wide intensity spread and evidence of bimodality.

However again let's stress that for the purposes of showing that classes have distinctive differences, we may fit unimodal distributions for all classes. Comparing the uncalibrated and calibrated  $P_{dB}$  histograms shows that calibration will shift the median and slightly change the distribution scale parameter.

Fig. 5.11 presents the results of fitting errors estimated based on the  $P_{dB}$  of radar clutters. Weibull and log-Weibull distributions show comparable fit errors to the four classes and have smaller fitting errors than Rayleigh and Rician. Thus, Fig. 5.12 shows the distribution parameters of uncalibrated (a) and calibrated (b) dB-power region statistics resulting from the Weibull fit.

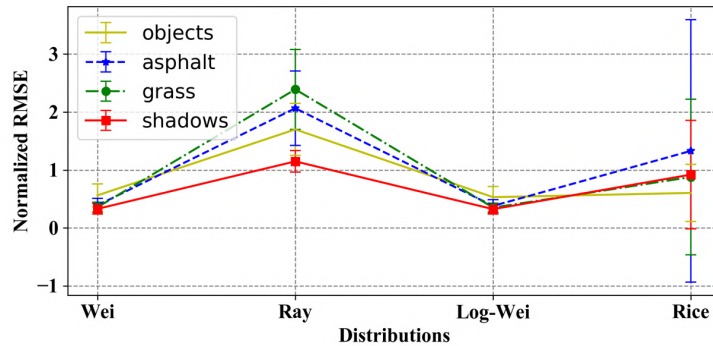


Fig. 5.11 NRMSEs of PDF fits to the density histograms of uncalibrated radar power map regions for the four classes.

The following conclusions can be drawn:

1. For results of both uncalibrated and range calibrated data, the scale parameter,  $\lambda$ , showed significant contrast between different classes.
2. The  $\lambda$  parameter obtained from the uncalibrated  $P_{dB}$  decreases with range for all four classes, although for shadows it has distinctively less change than for other classes. Importantly, for classes other than shadow, this decreasing trend is reduced after the calibration and therefore we may assume that the same class will

have similar statistical parameters across the full range of the calibrated image. By contrast, the calibration leads to an increase in shadow parameter values which again indicates its essentially different physical nature of shadow—calibration results in an invalid increase of receiver noise floor values, rather than actual calibration of returned powers.

3. The results for Weibull shape parameter,  $k$ , mainly stresses the contrast between objects and other classes, with calibration improving the object parameter separation, but reducing that of shadow.

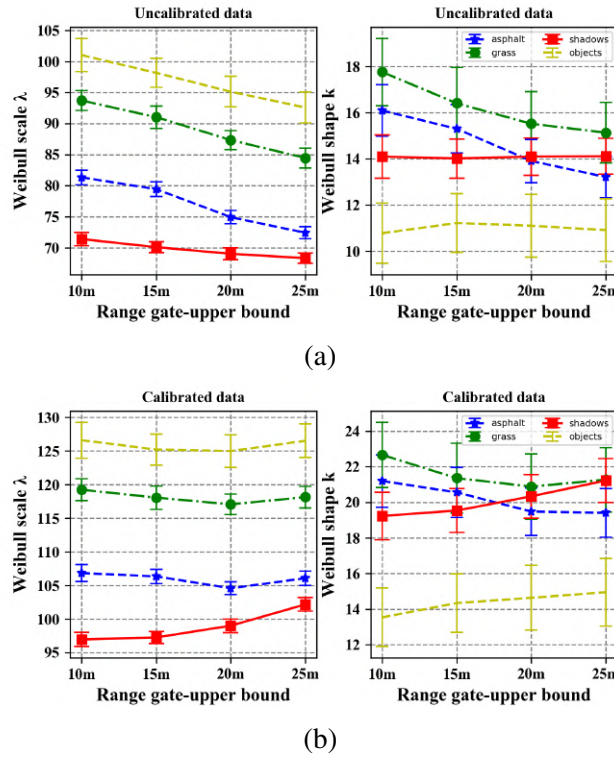


Fig. 5.12 The parameters obtained from Weibull distribution fit to uncalibrated  $P_{dB}$  (a), and calibrated  $P_{dB}$ ; (b) Range values indicate the upper value of a range gate.

We may conclude that the parameters obtained from the  $P_{dB}$  data showed higher contrast than  $V_{intensity}$  and calibrated and uncalibrated data representations both have their own advantages for parameter contrast. Thus, both representations will be tested in discrimination of different classes.

## 5.4 Classification Based on Statistical Distribution Features

Here we propose the supervised classification algorithm based on the MGD model in which the extracted parameters of the Weibull distributions for each class are used as feature parameters. This model has previously been used for unsupervised anomaly detection [107]. At this stage the automotive radar image dataset is separated into training and test data to verify the model performance.

### 5.4.1 Classification Algorithm Based on MGD Model

The general definition of the MGD PDF is denoted as:

$$p(x_t) = \frac{1}{(2n)^{\frac{n}{2}} |\Sigma|^{\frac{1}{2}}} e^{-\frac{1}{2}(x_t - M)^T \Sigma^{-1} (x_t - M)} \quad (5.8)$$

where  $x_t = [f_1, f_2, \dots, f_n]$  is a feature vector consisting of  $n$  different random variables,  $M$  is the vector of their mean values  $M = [\mu_1, \mu_2, \dots, \mu_n]$ ,  $\Sigma$  is their covariance matrix and  $|\Sigma|$  is its determinant. In our case the random variables are the previously identified statistical distribution parameters and will be termed hereon in as feature parameters. To use the MGD formulation for classification we must include a training phase, this is a significantly different methodology than when used solely for anomaly detection. The training stage involves the calculation of one  $M$ , and one  $\Sigma$  per class  $c$  for the  $C$  classes under consideration i.e.  $M_c$  and  $\Sigma_c$ . This is accomplished using a class training feature parameter set  $X_{tr}^c$ , extracted from the training data.

$$X_{tr}^c = \begin{pmatrix} F_{1,1}^c & \dots & F_{1,n}^c \\ \vdots & \ddots & \vdots \\ F_{m,1}^c & \dots & F_{m,n}^c \end{pmatrix} \quad (5.9)$$

where  $F_{i,j}^c$  is an instance of a training feature and  $i = \{1 \dots m\}$  labels the number of samples (observations) of the  $j = \{1 \dots n\}$  feature parameters, i.e. the number of regions of a particular class from which the feature parameters have been extracted. The values  $\mu_j^c$  in  $M_c$  and elements of  $\Sigma_c$  are calculated as follows:

$$\mu_j^c = \frac{1}{m} \sum_{i=1}^m F_{i,j}^c, \quad \sum_{j,v}^c = \frac{1}{m} (F_{i,j}^c - \mu_j^c)(F_{i,v}^c - \mu_v^c)^T. \quad (5.10)$$

Once MGD's for all classes have been trained, a test vector of feature parameters  $x_t$ , from an unknown class region can be evaluated using Eq. 5.8 to obtain a p-value,  $p_c(x_t)$  from each class MGD. The p-values give the probability that the test set belongs to a particular class, further evaluation of the obtained set of p-values is used to assign a single class type to a region. This involves 2 stages of decision making, which will be described later in this sub-section and expanded upon in Section 5.5.2.

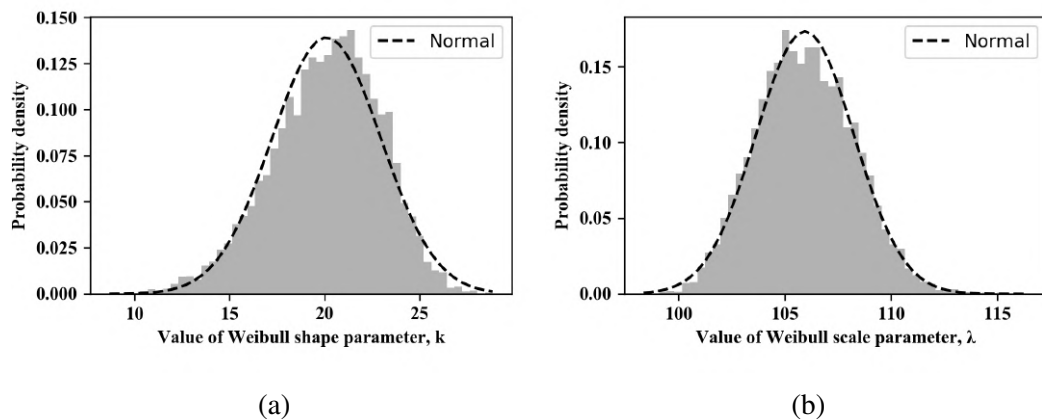


Fig. 5.13 Probability density histograms of extracted statistical parameters and normal PDF fits for “asphalt” class: (a) Weibull shape parameter  $\lambda$ ; (b) Weibull scale parameter  $k$ .

In order for a multi-variate statistic ( $n$ -variate in this case) to be Gaussian, each of its  $n$  variables should be Gaussian, thus for the MGD to model our feature parameters exactly, the distributions of the parameters should ideally be Gaussian. Examples of the density histograms for Weibull  $\lambda$  and  $k$  feature parameters for instances of the asphalt class, are shown in Fig. 5.13 with corresponding Gaussian fits. Although there are some

small observable discrepancies between the data and normal fit, similar to discussion in Section 5.3.2 regarding distribution fits, the MGD framework may still be used and approximates our parameters as Gaussian variables.

An example of the covariance matrix calculated for training feature parameters,  $\lambda$  and  $k$  of asphalt areas is shown in Eq. 5.11:

$$\Sigma_{k\lambda} = \begin{bmatrix} 8.22 & -0.21 \\ -0.21 & 5.3 \end{bmatrix} \quad (5.11)$$

This indicates  $\lambda$  and  $k$  have low correlation since the absolute values of non-diagonal elements are close to 0.

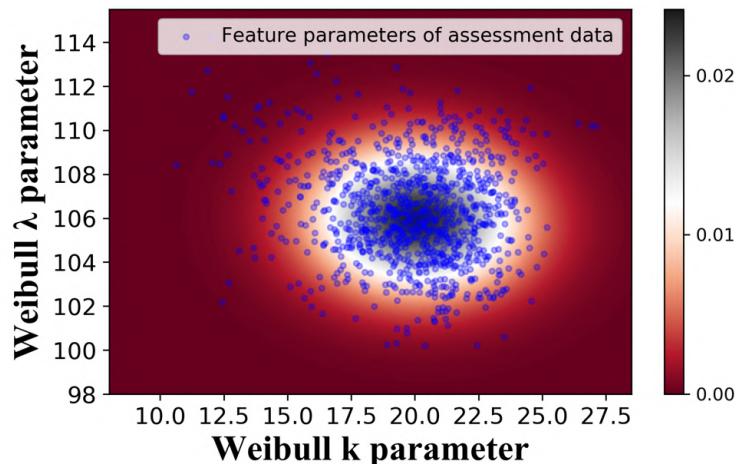


Fig. 5.14 Comparison between the generated bi-variate ( $\lambda$  and  $k$ -variates) Gaussian PDF for asphalt (colourmap indicates probability density) and the training feature parameter values (blue markers).

Fig. 5.14 shows the bi-variate Gaussian distribution generated using Eq. 5.8, the covariance matrix in Eq. 5.11 and the corresponding mean values  $\mu_\lambda$  and  $\mu_k$ . The circular shape again highlights the low correlation between features. The training feature parameter values are plotted with blue markers and show good agreement with the generated distribution—this emphasises that the MGD framework approximates our parameter distributions well.

To estimate performance of the MGD classifier, Weibull shape,  $k$ , and scale,  $\lambda$ , factors from uncalibrated (“unc”) and calibrated (“cal”) dB-power data are evaluated as feature parameters in the following combinations: i)  $x_t^{(1)} = [w_\lambda^{unc}, w_k^{unc}]$ ; ii)  $x_t^{(2)} = [w_\lambda^{cal}, w_k^{cal}]$ ; iii)  $x_t^{(3)} = [w_\lambda^{unc}, w_k^{unc}, w_\lambda^{cal}, w_k^{cal}]$ ; the effect of training sample size on performance is also examined. The full MGD model for the first case, combining the individual MGD’s for each class, can be represented as:

$$p_{MGD}(x_t) = \left[ p_1(x_t, \Sigma_1, M_1), \dots, p_c(x_t, \sum_c, M_c) \right] \quad (5.12)$$

Test ROI’s are selected from the labeled data. Each ROI is further divided into equal sample sub-regions. Feature parameters are extracted from each sub-ROI and form the input to the trained MGD model. The class with the highest  $p$ -value,  $p_c(x_t, \Sigma_c, M_c)$ , identifies a sub-ROI as belonging to that class—this is the first stage of classification. Thus, within each initial ROI we may have many sub-ROI’s labelled differently according to their individual result of classification. In the second stage of classification, the whole ROI is labelled as the class represented by the largest number of sub-ROI’s. In general, more complex metrics can be used for the voting of the class at the second stage of classification.

### 5.4.2 Estimation of Classification Performance

We use the F1-score [108] as a general assessment tool for estimating the performance of classification on the test dataset. The definition of the F1-score calculation is based on the precision and recall estimation of the classification results:

$$F1 = \frac{2 \cdot precision \cdot recall}{precision + recall} \quad (5.13)$$

in which, recall and precision are:

$$\text{precision} = \frac{T_p}{T_p + F_p}; \text{recall} = \frac{T_p}{T_p + F_n} \quad (5.14)$$

where  $T_p$ ,  $F_p$  and  $F_n$  are the number of true positives, false positives and false negative obtained from the confusion matrix results. We will evaluate the impacts of (i) the calibration of radar data and (ii) the size of the training dataset on performance of classification, the F1-score results are shown in Fig. 5.15 and 5.16.

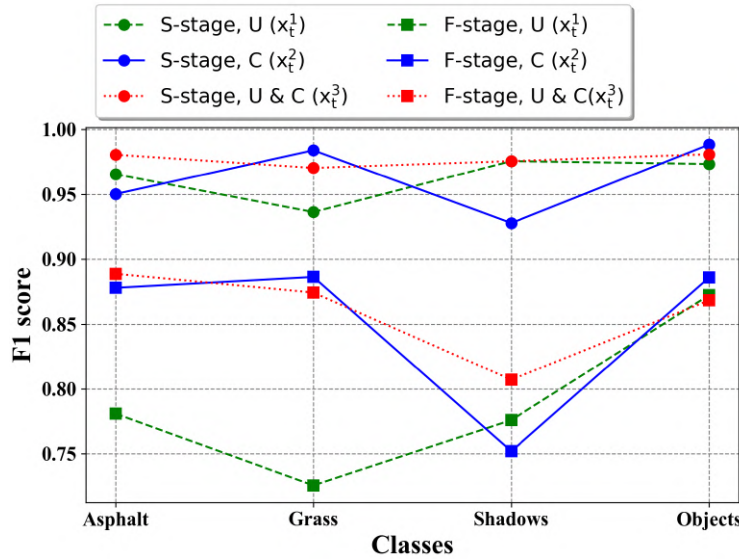


Fig. 5.15 F1-score results obtained from the classification algorithm. (Legend labels F and S indicate results of first and second stages of classification and U and C correspond to the use of uncalibrated and calibrated power data respectively.)

In Fig. 5.15, the F1-score at each classification stage are plotted for each class presented on x-axis. The results for the three types of feature parameter compositions,  $x_t^{(1)}$ ,  $x_t^{(2)}$  and  $x_t^{(3)}$  described in Section 5.4.1 are represented using different line types, and results of first and second stage of classification are shown by different markers. The results of first stage of classification showed that F1-scores of asphalt and grass areas are effectively improved by use of features from calibrated data, either solely or in combination with uncalibrated. By contrast, the F1-score of shadows showed the opposite effect where use of  $x_t^{(1)}$  results in better performance than that of  $x_t^{(2)}$ ,

however the combination of both,  $x_t^{(3)}$ , showed the best F1-score. These conclusions are consistent with the results and discussion in section 5.3.3, where we stressed the physically different mechanisms behind the clutter returns and shadows and the effect of calibration the distribution/feature parameters. The F1 score results of targets showed similar performance for all  $x_t^{(1)}$ ,  $x_t^{(2)}$  and  $x_t^{(3)}$  since feature parameters obtained from uncalibrated and calibrated data all demonstrate high contrast with respect to other classes. For the results of second stage of classification, the utilization of features from both uncalibrated and calibrated dB-power data improved the F1-score performance, especially for the asphalt, grass and shadow classes.

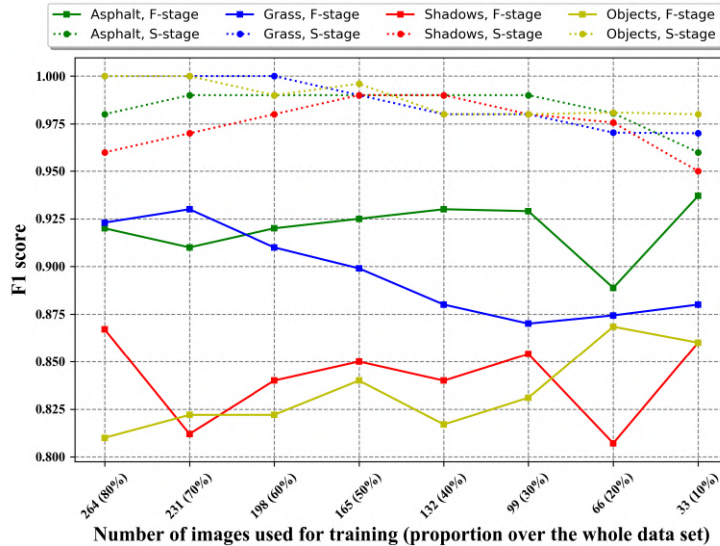


Fig. 5.16 F1-score results of classification algorithm for varied amounts of training data, using combined features case  $x_t^{(3)}$ .

In Fig. 5.16, F1-scores for the combined feature case  $x_t^{(3)}$  are plotted as function of the size of the training dataset, which was varied from 80% of the available dataset (330 frames) to 10%. Results for different areas are presented using different color. The results showed no obvious monotonic trend for different amounts of training data, however the F1 score of the second stage of classification did drop when using only a small fraction for training. Therefore, this classification algorithm does not significantly depend on the amount of training data, which infers a high consistency of

statistical parameters over all instances of class regions in the dataset. The comparison between results of first and second-stage of classification showed that classification performance is significantly improved in the second stage. This is also highlighted in the corresponding confusion matrices in Tables 5.2 and 5.3. The F1-scores of the first stage of classification are not higher than 0.825, and that of the second stage are above 0.95.

Table 5.2 Confusion matrix after first stage of classification combined calibrated/uncalibrated features.

		Predicted			
		Asphalt	Grass	Shadows	Objects
Actual	Asphalt	7020	121	1389	37
	Grass	97	3510	0	472
	Shadows	112	0	3149	4
	Objects	1	319	0	2748
	Recall	0.82	0.86	0.96	0.90
		Precision	0.97	0.89	0.69
		F1 score	0.89	0.87	0.81
					0.87

Table 5.3 Confusion matrix after second stage of classification combined calibrated/uncalibrated features.

		Predicted			
		Asphalt	Grass	Shadows	Objects
Actual	Asphalt	252	0	7	0
	Grass	1	180	0	5
	Shadows	2	0	180	0
	Objects	0	5	0	257
	Recall	0.97	0.97	0.99	0.98
		Precision	0.99	0.97	0.96
		F1 score	0.98	0.97	0.98

## 5.5 Automatic Segmentation of Radar Imagery

Till this point, we have shown the development and performance of the segmentation algorithm on fully labelled data. Now we move to the discussion of automatic segmen-

tation and classification of a single test frame. The processing flowchart is shown in Fig. 5.17 and processing steps will be explained in the following sub-sections.

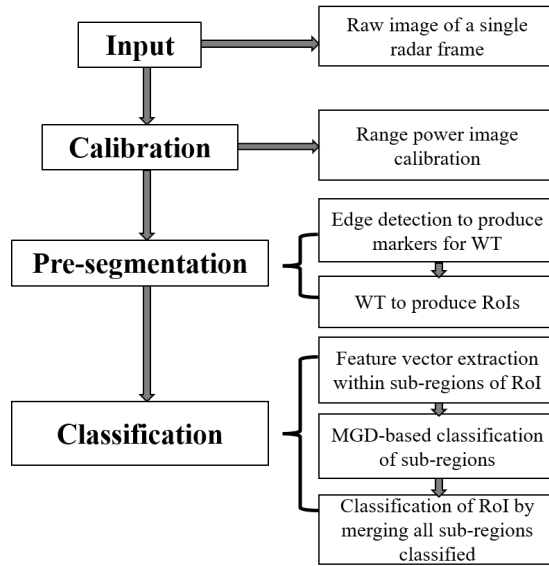


Fig. 5.17 Block diagram of the automatic segmentation on automotive radar image based on distribution feature extraction and MGD classification model.

### 5.5.1 Image Pre-segmentation Using the Watershed Transform

An image pre-segmentation stage is used to define the ROI's within which the classification and region merging stages are applied.

The most widely used methods of image segmentation based on RGB information are thresholding [99], edge detection [109], region growing [110] and WT method [111]. In this chapter, the marker-based WT method is used to generate the closed contours of the regions in the radar imagery, which will be subject to classification. The principle of the WT in OpenCV is given in [111] and full description of the method can be found in computer vision literature, e.g. [112–114]. Here we will only briefly describe main steps undertaken.

First, a greyscale image generated from the radar image is binarised using a threshold on raxel values. The threshold value utilized here is by default in OpenCV, and it can be set manually to mitigate the over- or under-segmented areas. Markers for the WT

are produced by subtracting the erosion binary image from the dilated binary image, producing a set of broken edges. These are then connected in the WT process to form the contours of sub-regions within the image, generating what we term a pre-segmented image. Results of this process using the uncalibrated and calibrated radar imagery are presented in Fig. 5.18—the extracted region contours are superimposed over intensity maps. It clearly demonstrates more robust performance of the method on the calibrated image Fig. 5.18(b), with the uncalibrated image Fig. 5.18(a) displaying both under-segmented regions containing mixed classes and over-segmented areas.

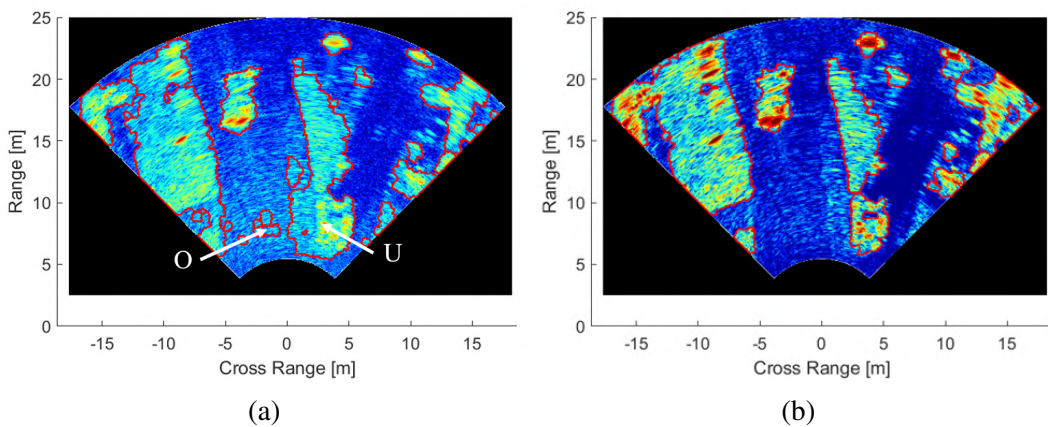


Fig. 5.18 The pre-segmentation results obtained using (a) uncalibrated and (b) calibrated radar images after single application of WT. ('O' indicates an over-segmented region, 'U' an under-segmented one.)

A single WT on a calibrated image is enough to produce region pre-segmentation, uncalibrated imagery would require multiple applications of the WT—this increases the algorithm complexity and computation time.

### 5.5.2 Region Merging Using MGD-based Classification Method

After pre-segmentation, which may result in potentially over-segmented ROIs, the identification and merging of similar regions is performed within the classification procedure described in Section 5.4.1. The input is the pre-segmented test automotive radar image which may include ROIs which do not necessarily correspond to any of the

defined classes. Therefore, to stress that for some regions the confidence in finding the correct class is low, another class “unknown” is introduced. This is a class containing the regions which show no obvious bias to any of the other classes in one of two distinct ways, described below. Firstly, the output p-values of the MGD model evaluated for specific ROI sub-regions are normalized using the softmax function defined as:

$$p_{soft,c} = \frac{e^{P_c}}{\sum_{c=1}^C e^{P_c}} \quad (5.15)$$

in which  $p_c$  represents the original p-values obtained from the MGD model and to reiterate,  $C$  is the number of classes (4 in this case). The softmax function allows elimination of large differences between the original  $p$  values. The “unknown” label will be assigned in the first stage of classification to the sub-ROI’s where all  $p_{soft,c}$  values are smaller than a threshold  $t_u$ . The sub-ROI’s for which at least one  $p_{soft,c} > t_u$  will be classified according to the highest  $p_{soft,c}$  value. In this work we used a threshold  $t_u = \frac{1}{C} + \varepsilon$  where  $\varepsilon$  is a small value, in our case 0.01, though this is a subject for further optimization. Table 5.4 gives examples of areas which are classified as either “known” classes (case 1 and case 2) or “unknown” (case 3). The three cases discussed here are actually asphalt class.

Table 5.4 Example of original p-values and softmax normalized values and their class determination.

Case	Original class p-values $p_c$				Softmax p-values $p_{soft,c}$				Class
	$p_a$	$p_g$	$p_s$	$p_o$	$p_{soft,a}$	$p_{soft,g}$	$p_{soft,s}$	$p_{soft,o}$	
1	2e4	5e-3	2e-33	1e-58	1	0	0	0	Asphalt
2	0.4	5e-9	2e-3	5e-6	0.33	0.22	0.22	0.22	Asphalt
3	2e-4	1e-19	4e-40	1e-6	0.25	0.249	0.249	0.249	Unknown

Secondly, the ROI will be classified as an “unknown” area if the highest score in the second stage of classification is not unique.

It should be stressed here that the pre-segmented image may consist of over-segmented areas which could be too small to extract a statistically meaningful number

of power values,  $P_{dB}$ , upon which to perform a distribution fit and extract parameters. These small areas are extended to a square region of rixels in the size of  $30 \times 30$  around the center point. Then the feature extraction will be performed within the extended area.

The rixels of the classified ROI will be labeled and colour-coded according to the assigned class, this operation will then be repeated for the next ROI.

### 5.5.3 Results of Automatic Segmentation of Automotive Radar Images

An example of an automatic segmentation result is illustrated in Fig. 5.19, which shows the annotated ground truth image of the scene (a), annotated calibrated radar frame (b), manually labelled image (c) and the automatically segmented and labelled image in (d).

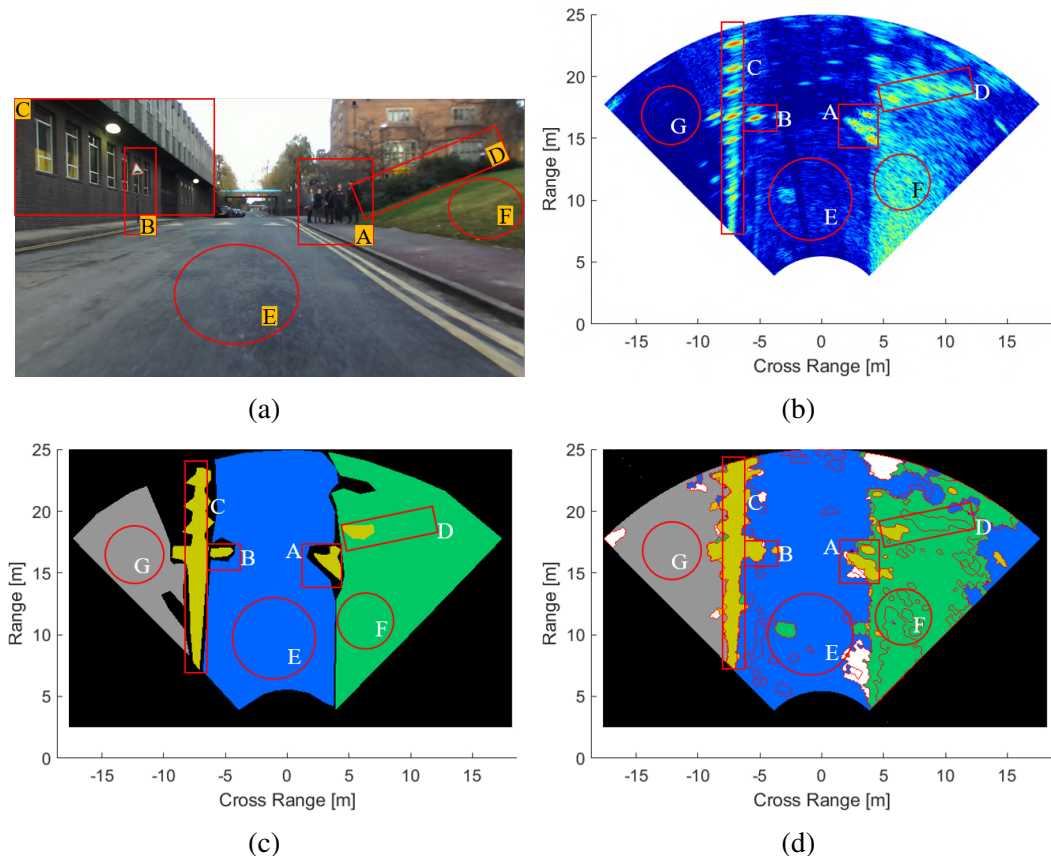


Fig. 5.19 (a) Ground truth optical image; (b) calibrated automotive radar image; the manually labeled image (c) and automatically segmented radar image (d).

Annotations in the Figure are: A, B, C, D are pedestrians, traffic sign, wall, and bush, respectively and all are of the class ‘object’. E is the road surface (class asphalt), F is grassed area (class “grass”) and G is a region of shadow of the wall (class shadow), white represents unclassified regions. Square bounding boxes are used for annotation of objects and circles identify surfaces.

Comparing Fig. 5.19(c) and 5.19(d) one can see that most of the objects and surfaces in the labeled image Fig. 5.19(c) are classified correctly in the full segmented image 5.19(d). Unclassified regions are present e.g. a region of pavement near the annotation E. Pavement regions are currently included in the asphalt class, in Fig. 5.19(b) however there is noticeable difference in the regions surface returns in contrast to its asphalt surroundings. This may just be an anomalously rough patch of surface, inclusion of a ‘pavement’ class may remedy the confusion in the classification. Another important feature is the region classified as a patch of grass (within circle E) within the asphalt road surface, this is a manhole cover. Importantly, it has been classified as a surface type feature rather than object and so could still be traversed, but the contrast can warn a vehicle to prepare for a transition. It may also be seen as an anomalous region within the large region of asphalt road and contextually this may aid identification—again additional classes may also be added.

The automatic segmentation results of 4 successive frames of a radar “movie” (radar snapshots) are shown in the bottom row of Fig. 5.20. Corresponding optical ground truth snapshots and calibrated automotive radar images are on the top and middle row respectively. The imaged scenes are mainly composed of areas of road tarmac, grass, traffic signs and trees on the grass area. The segmented images show that the majority of regions such as the areas of asphalt, grass and objects are properly segmented using the WT method and correctly classified based on the MGD model. The moving vehicle in different frames shown passing through the scene is also identified correctly with well-defined shape.

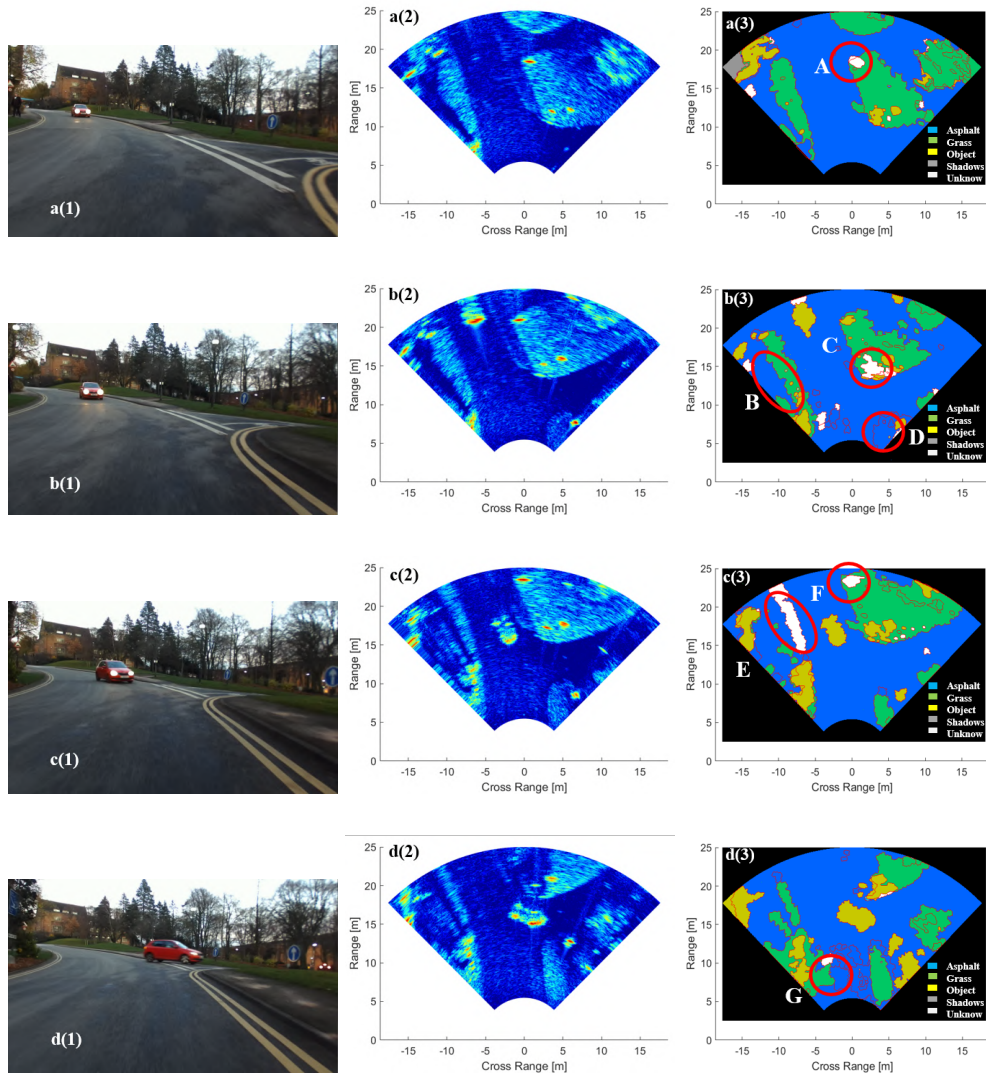


Fig. 5.20 The automatically segmented results of four consecutive frames of automotive radar imagery: a-d(1) are the optical images; a-d(2) are the calibrated automotive radar images and a-d(3) are the results of automatic segmentation. (Region colour coding equivalent to Fig. 5.19)

There are some incorrect classifications of areas. This may be caused by the overmerging of regions in the pre-segmentation. For example, area B in Fig. 5.20 b(3) shows that the shadow area has merged with the larger asphalt area and is incorrectly classified as asphalt. Similarly area G in Fig. 5.20 d(3) shows that the asphalt or kerbside merged with the lawn area and is incorrectly classified as grass area. Some regions have been classed as “unknown” areas, such as A in a(3), C in b(3) and F in c(3), which are

primarily object regions containing lampposts and signage, and E, an area of grass in c(3). However, each of these unclassified regions are in fact correctly classified in at least one of the 4 segmented images. In the next stages of research, we plan to improve confidence of true positive classification by using frame-to-frame region tracking and associations within a succession of frames.

The numerical estimation of the accuracy of the automatic segmentation and classification is conducted based on a test data set consisting of 120 continuous image frames and utilises the JSC [115]. In the performance analysis we exclude segments which, though classified as one of the known classes in automatic segmentation, cannot be confirmed by ground truth and were marked as black areas in the manually labelled images. The JSC for each class is defined as:

$$J_{class} = \frac{A_{fs} \cap A_{label}}{A_{label}} \quad (5.16)$$

where  $A_{fs}$  is the number of correctly classified rixels overlapping with the labelled data regions of that class and  $A_{label}$  is the total number of rixels of corresponding class in the labeled data.

The averages of the JSCs of the four area classes are presented in Table 5.5. Areas of asphalt have the highest JSC of 0.81 and the areas of grass and object show the lowest value of 0.64.

The JSC's for the single frame image segmentation of a relatively complex scene are encouraging. As mentioned previously, improvement will be made by considering results of consecutive frames of the radar movies.

Table 5.5 The JSCs of the automatically segmented radar images and the labeled images.

Areas	Asphalt	Grass	Shadows	Objects
Average JSC	0.81	0.64	0.79	0.64

## 5.6 Conclusions

An algorithm for automatic segmentation and classification of automotive high-resolution radar images is presented in this chapter. The two main steps in this algorithm are: 1) initial image pre-segmentation using WT method; 2) supervised region classification into chosen classes, utilizing statistical parameters of radar image regions as feature parameters in a proposed MGD classifier. The features were based on Weibull distribution parameters extracted from image data represented in dB-power units, this showed better contrast between features/classes than when considering radar intensity values.

As performance metrics, the F1 score and JSC have been used to assess the results of classification/segmentation. They showed good performance of the proposed algorithm to reconstruct the content of single (stand alone) radar image frames.

It was shown that the proposed two stage classification process can significantly improve the accuracy of the automatic classification.

A detailed range-power calibration process has been described and shown to vitally enhance the image pre-segmentation process when compared to using uncalibrated data. Segmentation/classification depends highly on the result of pre-segmentation by WT and this should be subject of further studies to determine the feedback mechanism to compensate the occasional inaccuracies of initial segmentation.

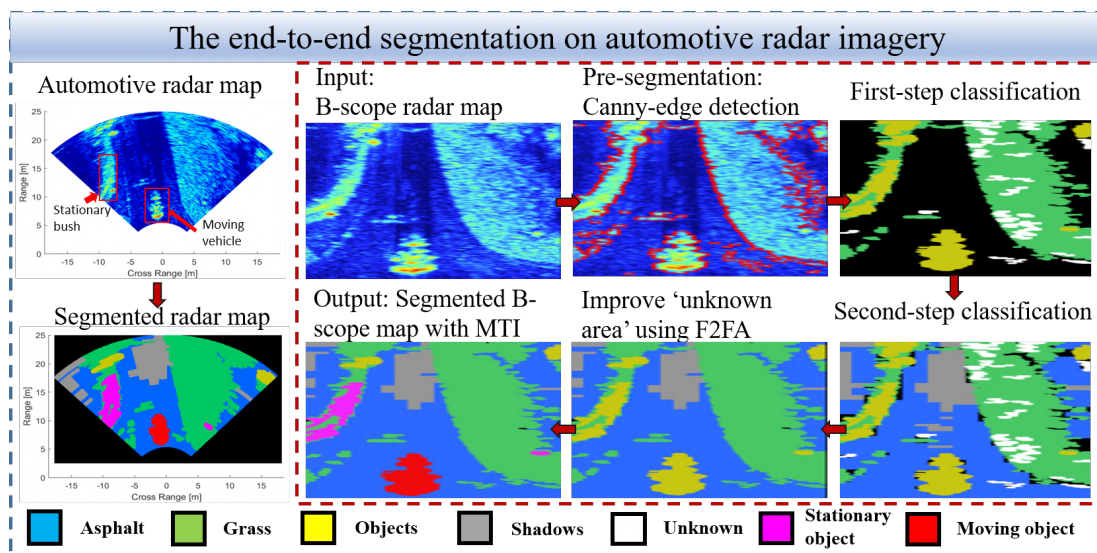
It was demonstrated that the calibration tends to reduce the variation of the feature parameters over the extent of the radar imagery. In general the Weibull statistical (feature) parameters for dB-power radar imagery show good separation between classes, the exception to this is the shadow class which has overlap with other classes in the scale factor k parameter, this motivates the inclusion of uncalibrated data features in order to improve classification of all classes.

Further work will also include context-based analysis to enhance classification, for example: anomalous regions within large extents of a particular class.

Finally, we will investigate the full use of multiple consecutive frames of radar movie to improve confidence of classification.

# Chapter 6

## The End-to-End Segmentation on Automotive Radar Imagery with MTI based on Frame-to-Frame Association



This chapter has been published as: "The End-to-End Segmentation on Automotive Radar Imagery" at the 18th European Radar Conference (EuRAD 2021) and is intended to be submitted to IEEE sensors journal. Author Contributions: The authors confirm their contribution to the chapter as follows: study conception and design: M.Gashinova, Y.Xiao; dataset collection: L.Daniel; data pre-processing: L.Daniel, Y.Xiao; algorithm implementation: Y.Xiao; analysis and interpretation of results: Y.Xiao; manuscript preparation: Y.Xiao, L.Daniel, M.Gashinova.

## 6.1 Introduction

Autonomous driving (AD) requires full scene assessment for effective path planning, which in the case of automotive imaging radar requires the development of novel approaches to characterize the whole scene within the field of view and to decompose it into stationary scenes with labeled entities and moving actors. The concept of image segmentation on automotive radar maps has been proposed in Chapter 5. The automatic segmentation on automotive radar imagery uses the hybrid method (HM) initially introduced in SAR image segmentation, which includes pre-segmentation based on watershed transformation (WT) [116] and supervised region classification based on MGD classifier [107]. In this chapter, we develop the end-to-end (E2E) radar image segmentation with moving target indication (MTI) based on frame-to-frame association (F2FA). To reduce confusion due to unambiguous correspondence between radar cells and pixels of segments or regions of interest present in our previous work using PPI radar maps, the image is now segmented in the B-scope radar map representation. The estimation on maximum segmentation and classification ranges of various areas allows the recommendation of the automotive radar parameters to achieve the region classification task at useful ranges. The segmentation will be made in a two-step process where 1) areas of strong returns will be identified after Canny-edge detection, and 2) remaining areas of weak returns, closer to the radar noise level, will be assessed to distinguish between shadows and low RCS clutter areas using an appropriate threshold. F2FA is utilized to distinguish moving objects based on overlap features and also to re-classify ill-determined unknown areas from the two-step segmentation.

The technique of MTI is used in scenarios where the removal of clutter is paramount for the detection of targets [117]. It has been successfully developed in the field of automotive radar system [118, 119], airborne surveillance radar [120], through the wall detection [121], indoor tracking [122] and SAR [123]. Traditional MTI methods use Kalman filters for the special case of linear dynamical systems with Gaussian noise

[124, 125]. Our implementation achieves the MTI based on the classification results of individual radar frames. We would like to stress that Doppler information is not available here for achieving MTI due to the large pulse repetition interval (PRI) of our radar system with high-resolution imagery. Therefore, the procedure of tracking is identified as F2FA instead of using Doppler information. The overlaps of moving and stationary objects between frames have been estimated and utilized for distinguishing them. Additionally, the ‘unknown areas’, which show low bias to any of the considered classes within the two steps of single frame segmentation, have been improved by F2FA.

This chapter is organized as follows: Section 6.2 introduces the automotive radar image dataset which utilizes B-scope radar maps. We estimate the noise floor hitting ranges of different areas to understand the maximum range where segmentation can be achieved. Section 6.3 states the details of single frame segmentation in E2E segmentation. Section 6.4 proposes the concept of F2FA which delivers: 1) MTI and 2) re-classification of unknown areas. In section 6.5, both results with and without MTI have been estimated and discussed. Jaccard similarity coefficients (JSCs) of segmentation results are investigated and compared with results in Chapter 5. Finally, conclusions are formulated and further steps are outlined.

## 6.2 B-scope Radar Map Dataset

### 6.2.1 B-scope Radar Map

In Chapter 5, we have given the details of the radar systems used, the dataset, and the processing approach. The region classification based on statistical properties of selected area classes requires initial labeling based on the assessment of the radar power return map, which carries physical information on scattering properties of regions positioned in range and azimuth as defined by radar resolution.

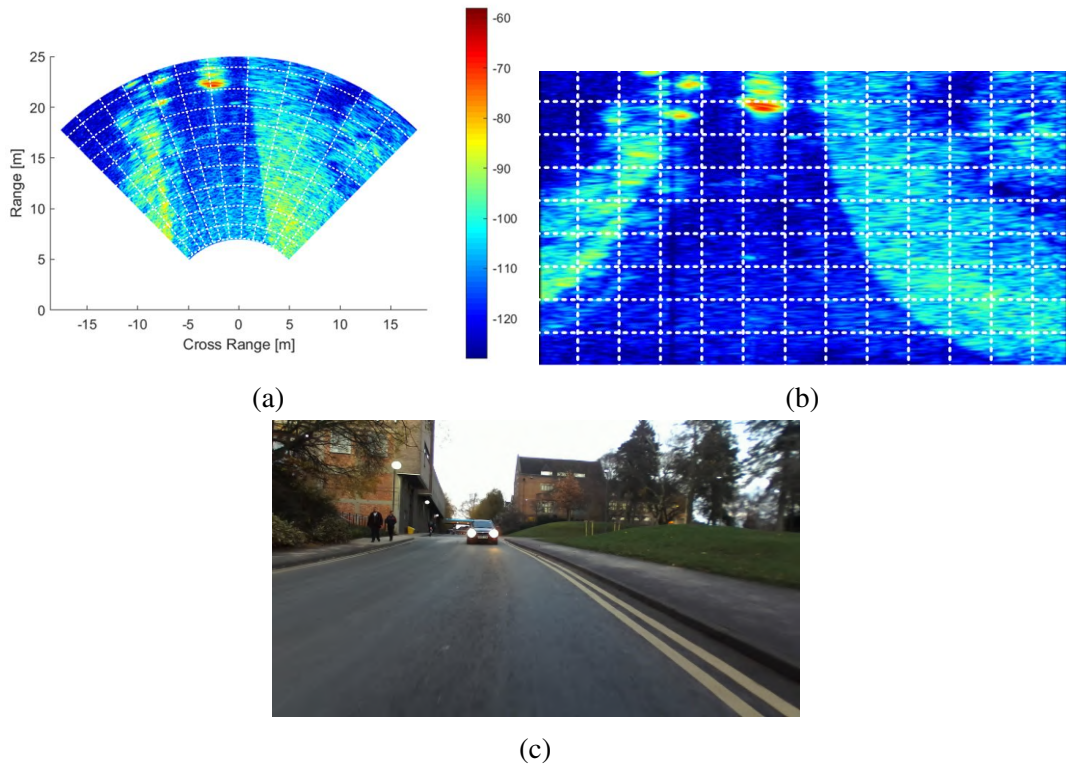


Fig. 6.1 (a) is the PPI radar map; (b) B-scope map of the same size ( $802 \times 199$ ) of radar cells; (c) ground truth - photo.

Two data mapping representations can be used for scene mapping by high-resolution automotive radar: plan position indicator (PPI) radar map and B-scope radar map. PPI representation has been used in Chapter 5 which can provide a good view of position and shape of objects as shown in Fig. 6.1(a) for the scene in Fig. 6.1(c). The radar range-azimuth map pixels are defined as resolution cells, and the radar raster image pixels with three color channels are defined as rixels. The mapping between rixels of the PPI map, and cells of the radar return power map is achieved by sophisticated coordinate transformation calculation since the size of radar cells is range-dependent in the PPI map. To simplify the mapping between rixels of the PPI map and cells of the radar return power map and reduce the confusion due to ambiguous correspondence between regions expressed in radar cells and pixels, the B-scope radar map representation (Fig. 6.1(b) of the scene in Fig. 6.1(c)) is considered here. B-scope radar maps with power

---

returns calibrated as in Chapter 5 will therefore be considered as the input into the E2E segmentation to produce segmented ROIs for further classification.

The radar data used in the example of Fig. 6.1 were collected using experimental high-resolution 79 GHz FMCW real aperture radar, designed by the University of Birmingham and ELVA-1 [126], though the approach is applicable to any high-resolution imagery. More details of the parameters of automotive radar system are given in Chapter 5. The data was recorded from a moving vehicle platform within the urban environment of the campus of the University of Birmingham, UK. The data collection is conducted based on the rear-facing automotive radar from a forward-moving car, and the following analysis, especially in F2FA, will be done reciprocal by assuming that the front radar collects data when the car moves forward.

Regions are classified according to several chosen classes which would define passable vs unpassable regions: asphalt, grass, shadow and somewhat arbitrary “object”, which includes various roadside and urban objects such as buildings, pedestrians, signposts [126]. For each, instead of traditional beam-filling RCS, we will use NRCS of distributed clutter to stress the general extended nature of regions in the clutter map to be segmented [126]. The whole dataset, which contains 330 frames of radar maps, is divided into three parts which are: 30% used as training dataset, 30% as validation dataset, and 40% used as test dataset. The whole dataset is manually labeled and used for statistic feature extraction and the estimation of segmentation performance.

Let’s stress that while physical beamforming with mechanical steering has been used for data collection and scene mapping here, the methodology developed is applicable to any radar image, obtained as a result of physical, MIMO, or synthetic beamforming.

### 6.2.2 Estimation of Maximum Segmentation/Classification range.

Here we will consider the physical margins of applicability of image segmentation process by finding ranges to which regions can be classified unambiguously w.r.t. particular radar parameters.

As discussed previously in Chapter 5, in imaging radar we will treat the radar map as a clutter map, considering main classes such as asphalt, grass, objects, and shadows. The power return as a function of range is governed by multiple factors, as expressed in the following radar equation:

$$P_r = S(R) \cdot L_{atm}(R) \cdot L_{prop}(R, \lambda) \cdot \sigma \quad (6.1)$$

Here,  $S(R) = P_t G^2 \alpha$  is the radar response characteristic,  $P_t$  is the transmitted power,  $G$  is the antenna gain,  $\alpha$  is the receiver response.  $L_{atm}(R)$  is an atmospheric loss,  $L_{prop}(R, \lambda)$  is the propagation loss,  $\lambda$  is the wave length,  $\sigma$  is the radar cross section where for clutter  $\sigma = \sigma_0(\theta_g, P, h_{rms}, L_c, \epsilon_r) \cdot A_{cell}$ . Here  $\sigma_0$  is the NRCS which depends on grazing angle,  $\theta_g$ , polarization  $P$ , surface roughness  $h_{rms}$ , correlation length  $L_c$  and dielectric permittivity of the surface material  $\epsilon_r$ .  $A_{cell}$  is the area of resolution cell:  $A_{cell} = \Delta R \cdot \Delta x = \Delta R \cos(\theta_g) R$ . Here,  $\Delta R = 2R \cdot \tan(\theta_{az}/2)$  is the cross-range dimension of the illuminated area,  $\sigma_{az}$  is the 3dB azimuth beamwidth,  $\Delta x$  is the range resolution and  $\Delta x_{gnd}$  is the ground range resolution. The parameters of radar to be used to calculate received power are given in Table. 6.1.

Table 6.1 The feature parameters of the automotive radar system.

$I_t$	G	$\alpha$	$\lambda$	$\theta_{az}$
17 dBm	30 dB	-23 dB	0.0038 m	17°

The noise floor can be considered as a constant defined by:

$$P_{noise} = kT_0 BF_{noise} \quad (6.2)$$

where  $k$  is the Boltzmann's constant,  $T_0$  is the temperature of the receiver,  $B$  is bandwidth and  $F_{noise}$  is the noise figure. Let's stress here that shadow is a special class which though being seen on the imagery as the area of low return, physically represents not a reflection, but noise floor of the radar.

Therefore, our task will be to find ranges to which selected classes, characterized by  $\sigma_0$  can be resolved, or in other words, their returns will be above the noise floor. The smallest of such ranges will define the boundary, where image segmentation can characterize scenes completely. At longer ranges, some clutter returns will be under the noise floor, and therefore may be incorrectly classified as shadow areas. This allows recommendations on the transmit power and noise performance of the automotive radar system to achieve the region classification task at useful ranges.

The measured average power level estimated from the labeled non-calibrated automotive radar image dataset covering a selected range of 5 m-55 m is shown in Fig. 6.2. As expected at shorter ranges the power decreases more rapidly with the range due to more rapid change of grazing angle, and then return power asymptotically approaches the radar noise floor at long ranges. The average value of noise floor is calculated as -120 dBm in the following estimation.

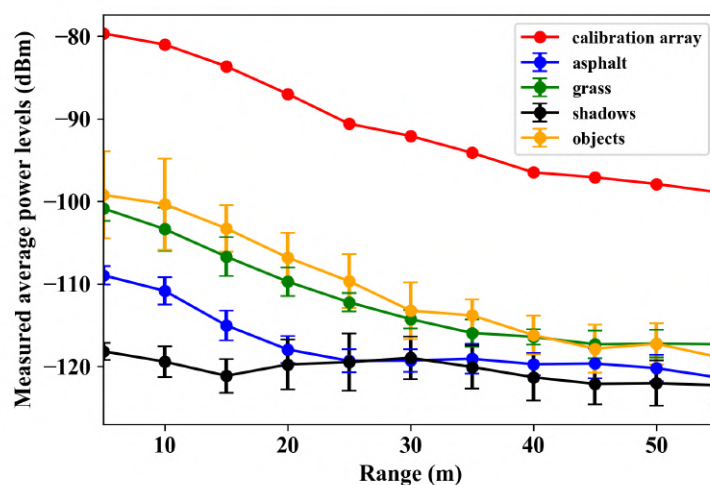


Fig. 6.2 The measured average power levels of un-calibrated radar data with respect to range gates and the calibration array utilized for power level calibration.

The factor to be equalized within calibration can be represented mathematically as:

$$F_{cal} = S(R) \cdot L_{atm}(R) \cdot L_{prop}(R, \lambda) \quad (6.3)$$

and obtained by applying the polynomial loss fit curve to the returns from the trihedral corner reflector (CR) used as a reference target positioned at different ranges [126]. The practical calibration values utilized for whitening the radar return power level is presented as red plot in Fig. 6.2 which is obtained according to Eq. 6.1:

$$F_{cal} = \frac{P_{meas}^{CR}}{\sigma_{CR}} \quad (6.4)$$

where  $P_{meas}^{CR}$  is the measured return power level of CR and  $\sigma_{CR}$  is the RCS of CR which corresponds to the factor of  $\sigma$  in Eq. 6.1 in the case of the reference target. After applying the calibration of return power w.r.t range, we intended to classify the regions independently on their range.

According to Eq. 6.1, the NRCS of various areas can be calculated as:

$$\sigma_0 = \frac{P_{meas}}{F_{cal} \cdot A_{cell}} \quad (6.5)$$

Here,  $A_{cell}$  is calculated based on the parameters of the radar system. The estimated NRCS of different classes as a function of range/grazing angle are presented in Fig. 6.3(a).

The NRCS tends to flatten at longer ranges, therefore for the ranges beyond 30 m the following average NRCSs will be used for the calculation of max ranges (hitting range) to which each class will be resolved, being above the noise floor:  $\sigma_0^{asphalt} = -41.4$  dBsm/sm,  $\sigma_0^{grass}$  and  $\sigma_0^{objects} = -33.4$  dBsm/sm, respectively. The estimated  $\sigma_0^{asphalt}$  shows agreement with the published measured backscattering coefficients of dry asphalt in [127], which means our estimation is reliable. The  $\sigma_0^{objects}$  is arbitrarily defined as it includes a large number of different targets with a significant difference in return. Fig.

6.3(a) shows median values of NRCSs and Fig. 6.3(b) indicates the range of potential values of areas of grass and objects. The comparison between the density histograms of  $\sigma_0^{objects}$  and  $\sigma_0^{grass}$  in Fig. 6.3(b) indicates that the  $\sigma_0^{objects}$  covers a wider NRCSs range than  $\sigma_0^{grass}$  as expected.

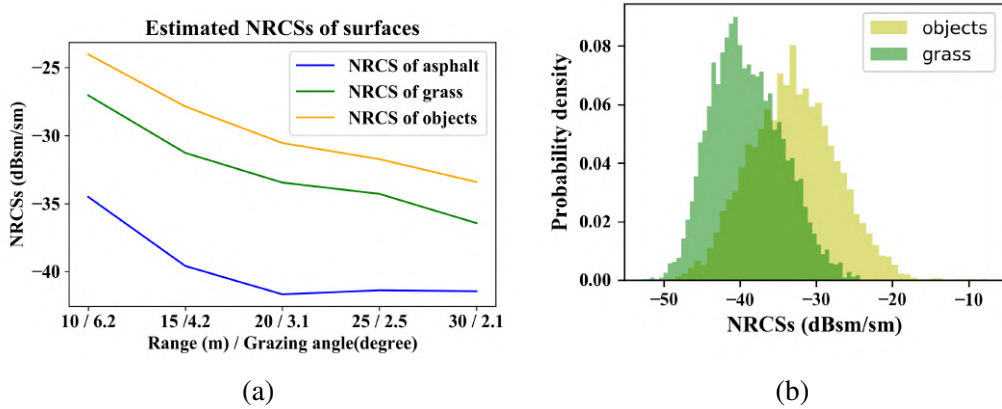


Fig. 6.3 (a) The estimated mean NRCSs of various areas based on the measured return power level. (b) The density histograms of NRCSs of grass and objects.

The measured average return power at ranges up to 55 m, and the evaluated values by use of NRCSs of selected classes at ranges up to 200 m are shown in Fig. 6.4, so that noise hitting ranges are estimated by the intersection with the noise power level. The smallest hitting range is of asphalt and it defines the region, R(1), where the full segmentation on all areas can be achieved in the ideal case. The longest range relates to the class “objects”, after which the image segmentation may not be possible since all returns are predominantly under the noise floor.

Table 6.2 Parameters of automotive radar systems

Radar system	INRAS	TI	NXP	Polarad79
Transmitted power (dBm)	10	12	10	17
Antenna gain RX (dBi)	15	10	15	30
Antenna gain TX (dBi)	17	10	17	30
Noise floor (dBm)	-131	-117	-130	-120

The transmitted power, antenna gains, and noise floor of some practical automotive radar development kits [128, 129] are shown in Table 6.2, alongside the bespoke radar

(Polarad79) used in this work. The predicted noise-hitting ranges of asphalt, grass, and class “objects” for these different radar systems are shown in Fig. 6.5, meaningful segmentation is only expected up to these ranges.

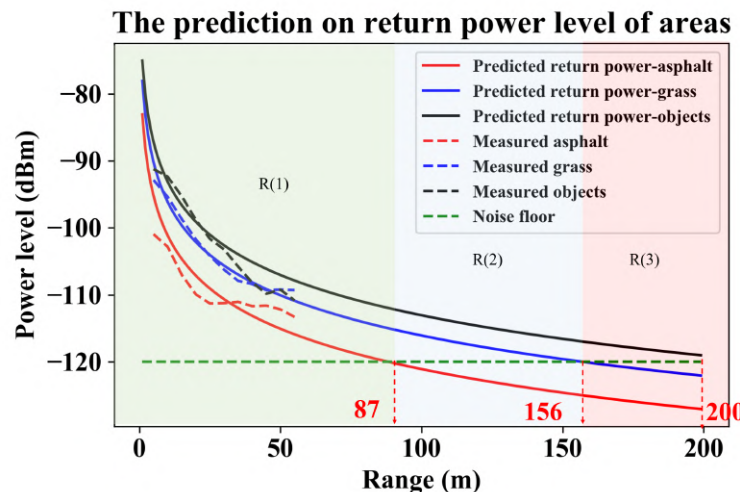


Fig. 6.4 The predicted return power level of various areas and the noise floor hitting ranges.

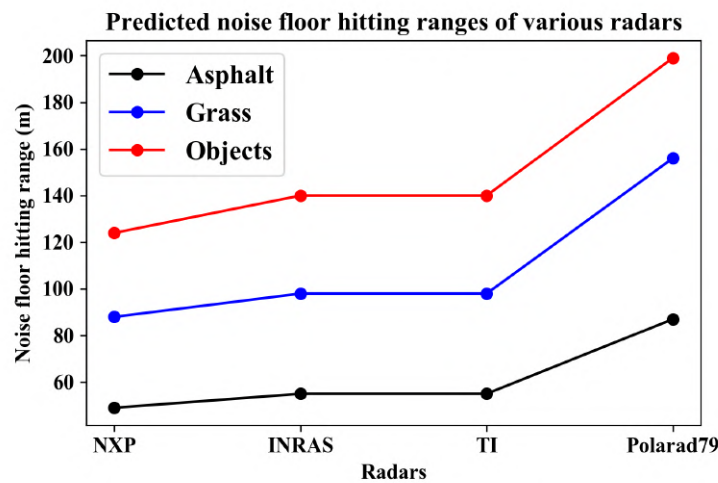


Fig. 6.5 The predicted noise floor hitting ranges of various classes as a function of the dynamic range of the radar system.

There are two ways to increase the meaningful range for image segmentation of automotive radar maps. One straightforward way is to increase the transmitted power or the antenna gain of the radar system, which is challenging due to the regulation of

the power flux density of the signals. Another way is to improve the noise performance of the radar receiver.

## 6.3 Single Frame Segmentation of the E2E Segmentation

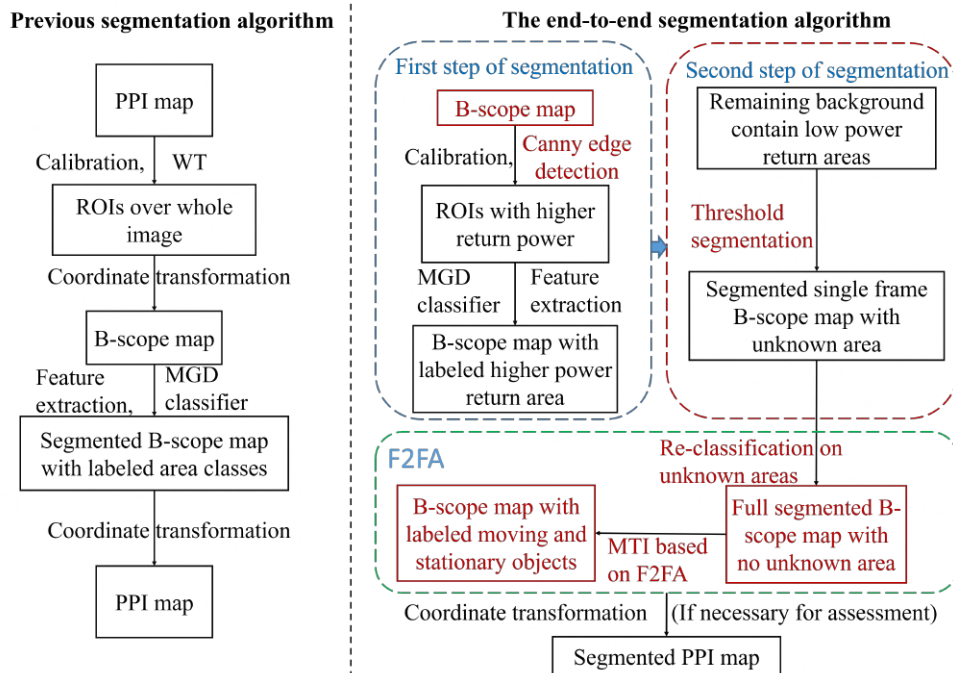


Fig. 6.6 Block diagrams of algorithm in Chapter 5 and the E2E segmentation.

In this section, we describe improvements to the single frame segmentation from Chapter 5, reformulated as a two-step segmentation process which then fit into the F2FA process discussed in the next section. Compared with the previous method in Chapter 5, the differences of single frame segmentation are 1) use B-scope radar map as the input into segmentation instead of PPI map; 2) use Canny-edge detection for pre-segmentation instead of WT; 3) use a two-step segmentation process, which includes the segmentation of higher contrast areas (first step) and then of lower contrast areas (second step). We would like to stress that contrast here indicates the intensity difference of areas when regarding radar map as RGB imagery, based on which Canny

edge detection can segment areas of grass and objects from the remaining background of asphalt and shadows.

Fig. 6.6 shows the block diagrams of the single frame segmentation proposed in Chapter 5 and the E2E segmentation developed, which includes single frame segmentation and F2FA.

### 6.3.1 Step 1-Segmentation of Areas with High Power Return

The first step of region classification includes pre-segmentation based on Canny-edge detection and region classification of high-power return classes. In the WT used for pre-segmentation in Chapter 5, the threshold used for producing binary images needs to be set manually to balance under- and over-segmentation between areas due to different color scales between frames. So Canny edge-detection is preferable in the further study in this chapter as it can detect the edges between areas with high contrast automatically, and the Otsu method threshold level is automatically determined [130] to improve the robustness of the pre-segmentation. An example of a pre-segmentation result, where contours of areas with higher power return are clearly visible is presented in Fig. 6.7 (a).

Additional size measure is implemented on ROIs produced by Canny edge detection to reduce the over- and under-segmentation automatically. The ROIs are divided into three groups by area size: small regions (SRs) which might be a result of over-segmentation, general regions (GRs), and large regions (LRs) which might be the merged areas. Two thresholds ( $t_{SR}$  and  $t_{LR}$ ), for defining SRs and LRs, are set based on the following considerations: (i)  $t_{SR}$  is determined by the number of resolution cells occupied by areas smaller than a signpost, as these areas are mostly over-segmented. These kinds of areas are merged into the surrounding region for classification. (ii)  $t_{LR}$  is determined by the number of resolution cells occupied by areas larger than the typical size of vehicles as they have a higher chance to be the under-segmented areas containing

grass and objects. For these areas, an additional operation of Canny edge detection is applied to determine if the region is merged and whether it can be further subdivided. Then ROIs are classified based on the MGD classifier developed in Chapter 5.

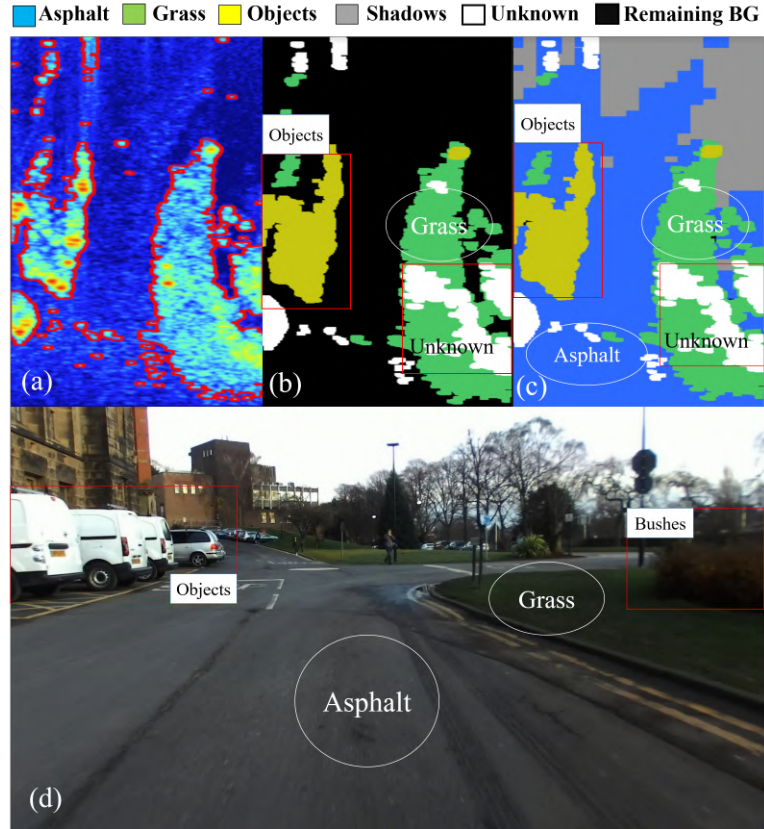


Fig. 6.7 (a) The result of pre-segmentation based on Canny edge detection; (b) The result after the classification of high-power return regions produced in pre-segmentation; (c) The result after segmentation of the remaining background which is mostly asphalt and shadows; (d) The optical imagery corresponds to the radar detected scene.

The classification result obtained from the first step of segmentation is shown in Fig. 6.7(b), which produces the labeled mask of high power return areas which are mostly grass and objects. The unknown areas are shown in white which shows low bias to any area classes. E.g. the “unknown” marked by the red bounding box in Fig. 6.7(b) is bushes whose distribution features show low bias to either objects or grass. The identification of “unknown” is based on the  $p_{soft}$  obtained from MGD classifier as described in [126] that areas with  $p_{soft}$  less than a certain threshold  $t_u$  is recognized as “unknown” in the current stage.

The value of  $t_u$  is finetuned by balancing the percentage of unknown areas and the precision of segmentation which is calculated as:

$$P = \frac{T_p}{T_p + F_p} \quad (6.6)$$

Here  $T_p$  is the number of true positives and  $F_p$  is the number of false positives. Fig. 6.8 shows the estimated mean precision values of various areas and the percentages of “unknown” areas obtained when increasing  $t_u$ . The x-axis is the threshold bias  $t_{bias}$  which has the relationship with  $t_u$  as  $t = \frac{1}{N_{class}} + t_{bias} \times 10^{-5}$ , where  $N_{class}$  is the number of considered area classes and  $N_{class} = 3$  in our case. As expected, the percentage of “unknown” area approaches to linear increase, and the precision improvement achieved by increasing  $t_u$  is limited at some point, which also means the limitation of performance improvement at the stage of single frame segmentation. The unknown regions are considered to be improved using context-based information through F2FA as described in section 6.4.

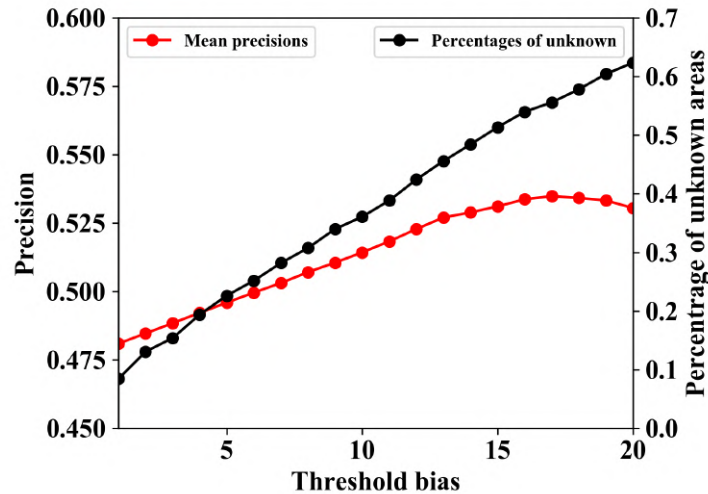


Fig. 6.8 The estimated mean precisions of segmentation results and percentages of unknown areas as function of threshold bias  $t_{bias}$ .

### 6.3.2 Step 2-Segmentation of Remaining Low Contrast Background

The segmentation of lower contrast areas of asphalt and shadows is shown in Fig. 6.7 (c), which is dealt with in the second step.

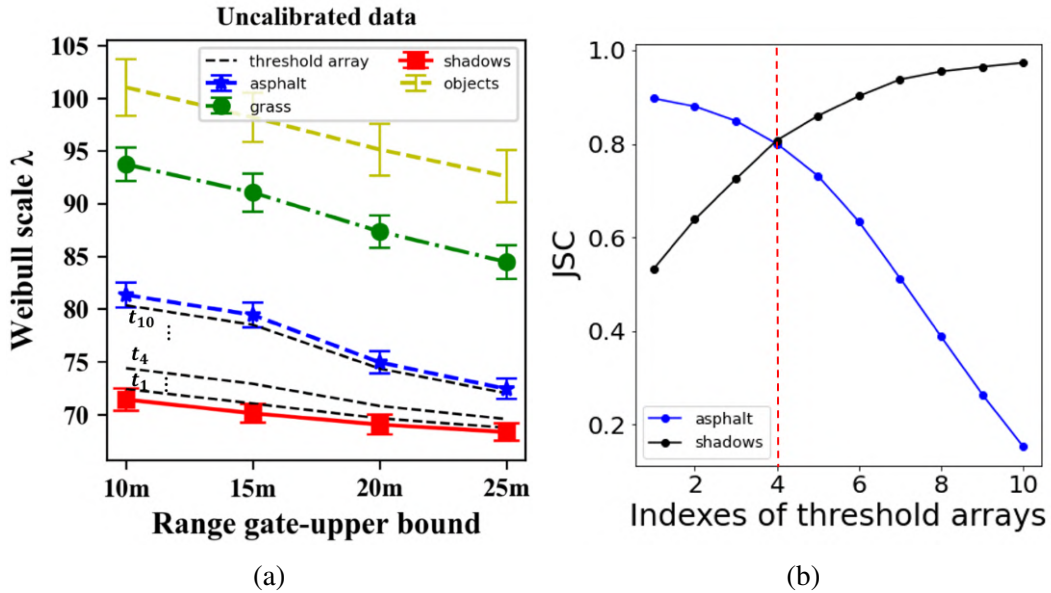


Fig. 6.9 (a) The Weibull scale parameters of various areas extracted from the uncalibrated data; (b) The estimated JSC values over different indexes of threshold arrays obtained based on the validation dataset.

Let us stress again the difference between shadow and other classes by looking at their distribution feature parameters, as discussed in Chapter 5. The Weibull scale factor,  $\lambda$ , of shadow areas exhibits a different trend with range compared to that of other classes, as shown in Fig. 6.9(a). Shadow may be understood as the receiver noise with little or no change in distribution parameters, evidenced by nearly constant  $\lambda$ .

In the second step of segmentation, shadows are separated through thresholding within the remaining low-contrast areas. ROIs under test are generated by a sliding window, whose size is sufficient to make a meaningful estimation of the distribution of samples within and estimate the scale factor,  $\lambda$ . The window size of  $30 \times 30$  is used here. The shadow threshold values  $t_s$  to be used, are determined from the feature parameters extracted from the training data at different ranges. Areas with  $\lambda < t_s$ , are classified as shadows, otherwise, they will be labelled as “asphalt”.

As shown in Fig. 6.9(a), thresholds for different range groups, are assumed to be between  $[\lambda_{sha}, \lambda_{asp}]$ , where  $\lambda_{sha}$  is the scale parameter of shadows and  $\lambda_{asp}$  is the scale parameter of asphalt at different ranges. To find the set of optimum threshold values, we equally divide the space between  $[\lambda_{sha}, \lambda_{asp}]$  into arrays of threshold levels  $[t_i]_{i=1\dots n}$ , which are represented as black lines in Fig. 6.9(a), with indexes of  $[1, 2 \dots n]$ ;  $n$  is the number of levels and  $n = 10$  here. The estimated JSC values are plotted as function of the index of threshold arrays as shown in Fig. 6.9(b). The optimized threshold array  $t_4$  is obtained by searching for which gives the best classification performance (highest average JSC value) based on the practical estimation.

## 6.4 Frame-to-frame Association

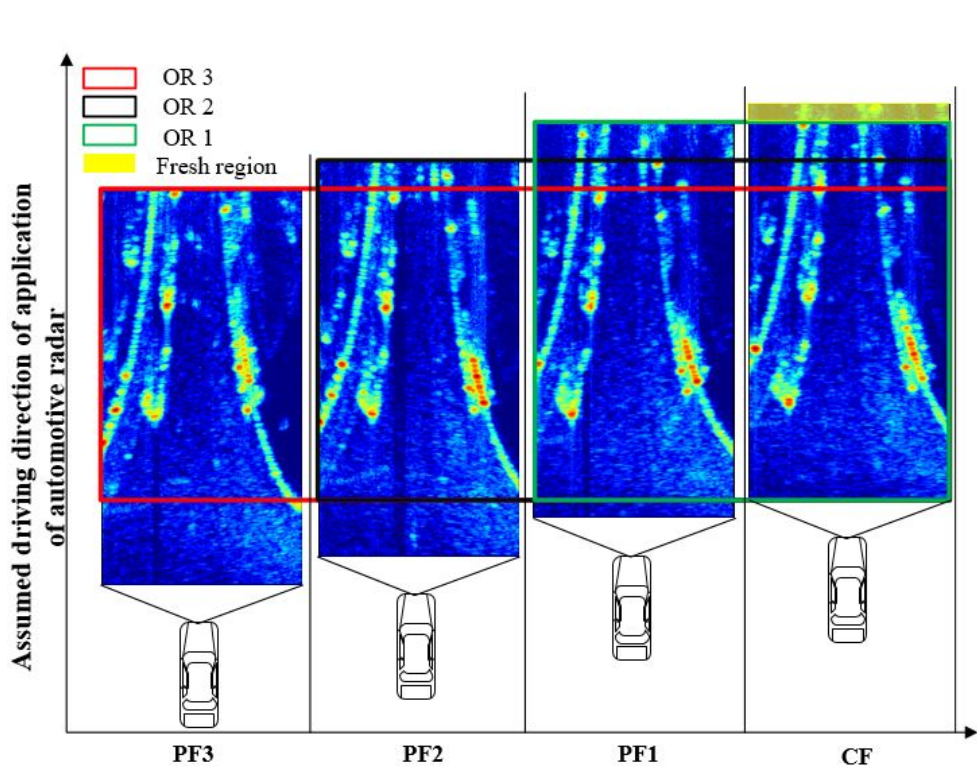


Fig. 6.10 The overlapping relationship between continuous frames in the scene detection of automotive radar.

F2FA is used to improve and extend classification performance based on context information from a sequence of segmented radar maps. As an illustrative example, Fig. 6.10 shows a set of four consecutive radar maps which we call the last frame as the current frame (CF) and three preceding as previous frame 1 (PF1), PF2 and PF3. The overlap regions between CF and PF1-PF3 are annotated as OR1, OR2, and OR3 in Fig. 6.10 so that the OR3 region in CF can be classified using information from all four consecutive frames.

### 6.4.1 Methodology of F2FA

#### Estimation on the Overlap Ratio of Radar Detected Scene

We need to know the overlap ratios between the CF and PFs so that we can estimate the number of PFs which can be tracked and utilized for F2FA.

The overlap ratios of a series of radar frames are defined by a number of factors, such as driving speed, trajectory, radar frame rate (number of frames per second), and the maximum detection range of the radar map. Here we estimate the relationship between overlap ratio, vehicle speed, and frame rate in different trajectories with a constant detection range.

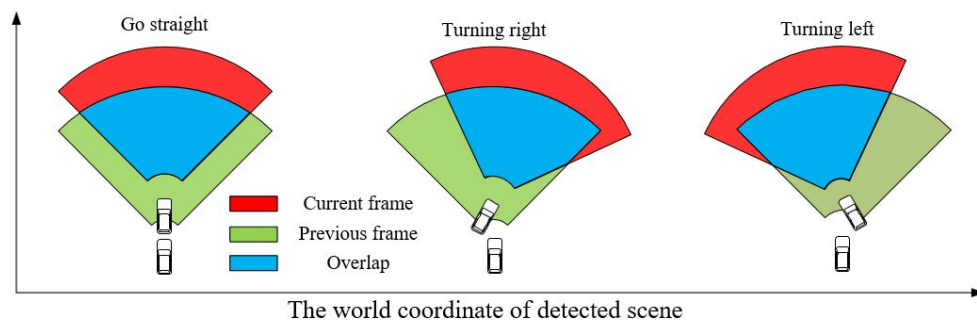


Fig. 6.11 The layout of three kinds of driving scenarios.

Three driving scenarios are considered in Fig. 6.11: moving straight, turning right, and turning left. The mapped field of View (FoV) of 90° in azimuth and a range of

5-25 m corresponding to two consecutive frames (CF and PF) are shown as sectors filled in red and green. The overlap ratio of the image frames, which is filled in blue, is calculated by:

$$P_{olr} = \frac{A_{oa}}{A_{frame}} \quad (6.7)$$

where  $A_{oa}$  is the area of the overlap region and  $A_{frame}$  is the area of a single frame. Under all equal conditions (speed, radar frame rate),  $P_{olr}$  is the same for either turning left or right, so we will consider this as one driving scenario called “cornering”.

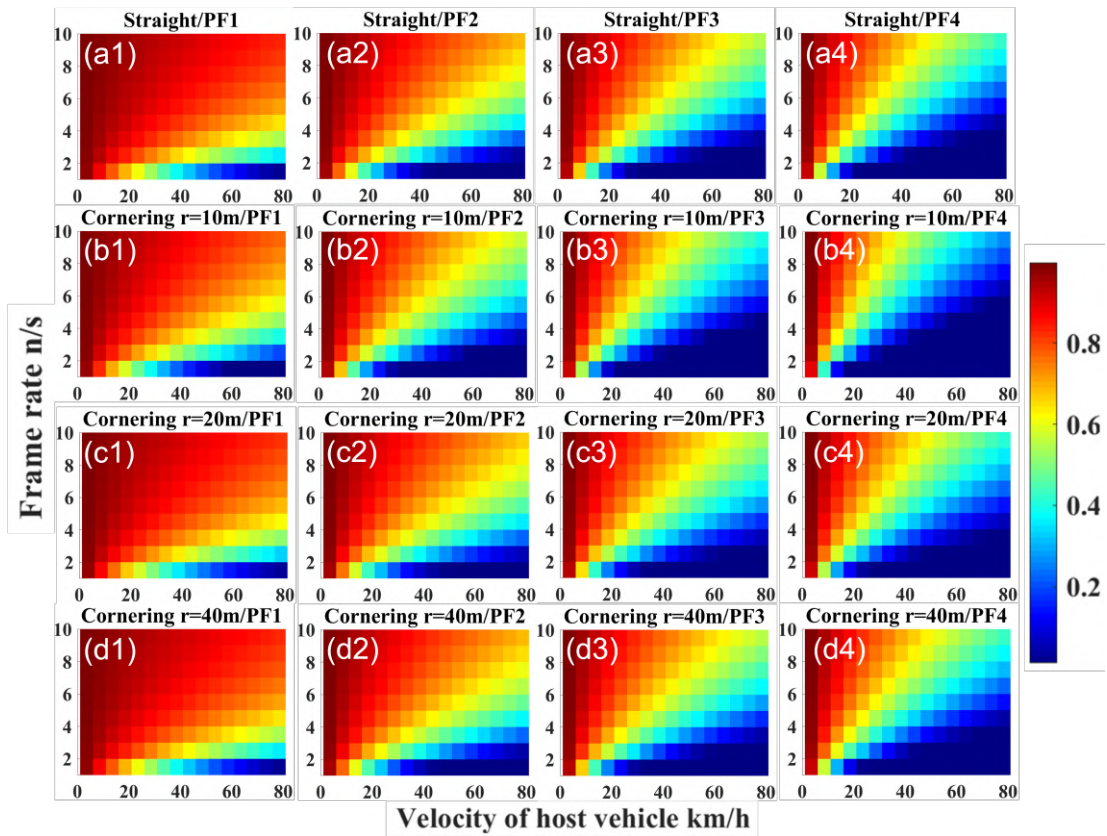


Fig. 6.12 The overlap ratios between CF and PFs versus vehicle velocity (km/h) and frame rate (n/s). (a1)-(a4) are going straight; (b1)-(b4) are cornering under the radius of 10 m; (c1)-(c4) are cornering under the radius of 20 m; (d1)-(d4) are cornering under the radius of 40 m.

Fig. 6.12 shows a “heatmap” of calculated  $P_{olr}$  as a function of frame rate (vertical axis) and vehicle speed (horizontal axis) for straight (Fig. 6.12 (a)) and cornering (Fig.

6.12 (b)-(d)) scenarios. When the host vehicle is driving straight, the overlap ratio between adjacent frames only depends on frame rate and vehicle speed, but in the case of cornering  $P_{olr}$  it also depends on angular velocity,  $\omega = \frac{v}{r}$ , where  $v$  is the linear velocity and  $r$  is the cornering radius. The cornering conditions with different radius values of 10 m, 20 m, and 40 m are presented in Fig. 6.12 (b), (c), and (d), respectively.

Due to the low frame rate of our experimental radar, 1 frame/s, the speed of the vehicle in the experiments was chosen to be low, around of 6 m/s, to allow frame overlap. Modern MIMO automotive radar can provide frame rates of tens of frames per second, for example, using a sweep time of 102.4  $\mu$ s and 4 Tx elements, the 'INRAS' radar [131] has a frame rate of 76 frame/s, which can provide enough overlap for F2FA even at higher driving speeds.

The overlap ratios of recorded four consecutive PFs are larger than 0.5, so half of the initial range will be assessed in all 4 frames for F2FA. In the case of cornering, the decrease of the cornering radius leads to the decrease of overlap while increasing the radius is similar to straight movement.

### **Image Registration based on Affine Transformation**

The movement of the vehicle assumes a shift of the scene mapping from frame to frame and therefore the relationship between pixels in consecutive frames needs to be established so that the same image regions will be correctly associated.

Ideally, exact positioning and velocity can be estimated by the use of time-stamped IMU and GPS, and the frame registration can be achieved by tracking the corresponding regions accordingly. This method is presented in our previous work in [132]. However, the real-time driving information is not available in the dataset utilized in this study due to the absence of IMU setup when collecting the data. Therefore, the alternative solution for coordinating the consecutive frames is proposed based on the affine transformation (AT) method [133]. The brief idea is to calculate the AT transformation matrices

between frames based on the manually marked-out corresponding keypoints. The obtained matrices can represent the geometric transformation relationship between frames, and are directly utilized for the frame registration to implement the similar function with the real-time driving information mentioned in the ideal case.

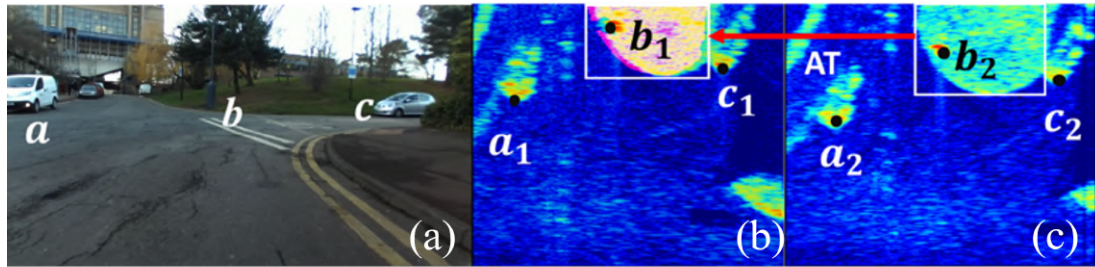


Fig. 6.13 Scene presented in optical imagery (a) and two radar frames of the B-scope radar map (b) PF and (c) CF. The manually selected keypoints and the example of region projection of grass area using AT are shown.

Firstly, let us make it clear on the calculation of AT transformation matrices. Due to the movement of the platform, the consecutive images can be distorted w.r.t each other and such distortion can be decomposed into – scaling, translation, rotation, and shear, which in general can be presented in operator matrix form:

$$\mathbf{p}_{n-1} = \mathbf{A}\mathbf{p}_n + \mathbf{b} \quad (6.8)$$

where  $\mathbf{p}_n$  is the vector of coordinates of the pixel in CF (or before AT),  $(x_n, y_n)$ .  $\mathbf{p}_{n-1}$  is the vector of coordinates of the corresponding pixel in PF (or after transformation),  $(x_{n-1}, y_{n-1})$ .  $\mathbf{A} = \begin{bmatrix} s_x \cos(\theta) & -sh_x \sin(\theta) \\ sh_y \sin(\theta) & s_y \cos(\theta) \end{bmatrix}$  is an invertible matrix where  $s_x$  and  $s_y$  specify the scale factor along  $x$  axis and  $y$  axis;  $sh_x$  and  $sh_y$  specify the shear factor along  $x$  axis and  $y$  axis, and  $\theta$  specifies the angle of rotation. The vector  $\mathbf{b} = \begin{bmatrix} t_x \\ t_y \end{bmatrix}$  represents operator of translation where  $t_x$  and  $t_y$  represent the displacement along  $x$  axis and  $y$  axis, respectively.

The calculation of AT matrices is considered as a backward procedure as we are going to learn the matrices of  $\mathbf{A}$  and  $\mathbf{b}$  based on the manually marked corresponding coordinates of  $\mathbf{p}_{n-1}$  and  $\mathbf{p}_n$ . Therefore, to establish AT matrices, three groups of corresponding keypoints are extracted manually as shown in Fig. 6.13, which are ( $a, a_1, a_2$ -stationary vehicle), ( $b, b_1, b_2$ -lamp post), and ( $c, c_1, c_2$ -another stationary vehicle).

When introducing the coordinate values of three keypoints in Eq. 6.8, the vector format of the combined equations can be represented as:

$$\mathbf{M}_{PF} = \mathbf{M}_{CF}\mathbf{E} \quad (6.9)$$

$$\Rightarrow \begin{bmatrix} x_{a,1} \\ y_{a,1} \\ x_{b,1} \\ y_{b,1} \\ x_{c,1} \\ y_{c,1} \end{bmatrix} = \begin{bmatrix} x_{a,2} & y_{a,2} & 1 & 0 & 0 & 0 \\ 0 & 0 & 0 & x_{a,2} & y_{a,2} & 1 \\ x_{b,2} & y_{b,2} & 1 & 0 & 0 & 0 \\ 0 & 0 & 0 & x_{b,2} & y_{b,2} & 1 \\ x_{c,2} & y_{c,2} & 1 & 0 & 0 & 0 \\ 0 & 0 & 0 & x_{c,2} & y_{c,2} & 1 \end{bmatrix} \begin{bmatrix} s_x \cos(\theta) \\ -s_x h_y \sin(\theta) \\ t_x \\ s_y \sin(\theta) \\ s_y \cos(\theta) \\ t_y \end{bmatrix} \quad (6.10)$$

where coordinates of each keypoint  $j$  in  $i$ -th frame is presented as  $[x_{j,i}, y_{j,i}]_{j=a,b,c}^{i=1,2}$ ,  $i = 1$  represents the coordinates of PF and  $i = 2$  represents the coordinates of CF. The least-squares solution of vector  $\mathbf{E}$ , which includes the six entities of  $\mathbf{A}$  and  $\mathbf{b}$ , can be determined as [134]:

$$\mathbf{E} = [\mathbf{M}_{CF}^T \mathbf{M}_{CF}]^{-1} \mathbf{M}_{CF}^T \mathbf{M}_{PF} \quad (6.11)$$

The calculated AT matrices are recorded and synchronized with our consecutive radar frames for frame registration. The frame registration is considered as a forward procedure as the regions in PF ( $\mathbf{p}_{n-1}$ ) are tracked based on the coordinates of regions in CF ( $\mathbf{p}_n$ ) and the calculated AT matrices using Eq. 6.8.

To show the result of this forward procedure, we present one example of frame registration that the pink colored mask in Fig. 6.13 (b), the PF, is projected from the grass-contoured region with a white box in Fig. 6.13 (c), the CF. The AT transformed area demonstrates very good correspondence of practical grass region in PF.

This method aims at achieving the geometric transformation between consecutive frames, which is not limited to the method of AT. The AT matrices are recorded as the external input to the end-to-end segmentation algorithm. Therefore, the automatic segmentation procedure will not be interrupted by this manual keypoint selection.

### 6.4.2 MTI using F2FA

In our dataset, mainly three kinds of moving objects are observed: vehicles, pedestrians and bicycles. By considering the overlap of classified object regions in consecutive image frames, image-based MTI can be performed to distinguish stationary and moving objects.

Fig. 6.14 shows the expected difference between stationary and moving objects in image registration, where (a) and (d) are the ground truth optical imagery, (b) and (c) are the consecutive manually labeled radar maps with the projected region of stationary objects, (e) and (f) are the consecutive manually labeled radar maps with the projected region of moving objects. The highlighted object regions in (b) are projected onto the PF (c), based on the assumption that they are stationary, and are highlighted by a pink semi-transparent mask in (c). Their position and shape coincide with the labelled region of the parked car in (c), labeled as yellow, indicating they are stationary objects. In contrast, in Fig. 6.14 (e), and (f), the projected region of a moving car is displaced from its observed position (red box in (f)) in the PF, which indicates that it moves and the size of overlap area will lead to estimation of its speed.

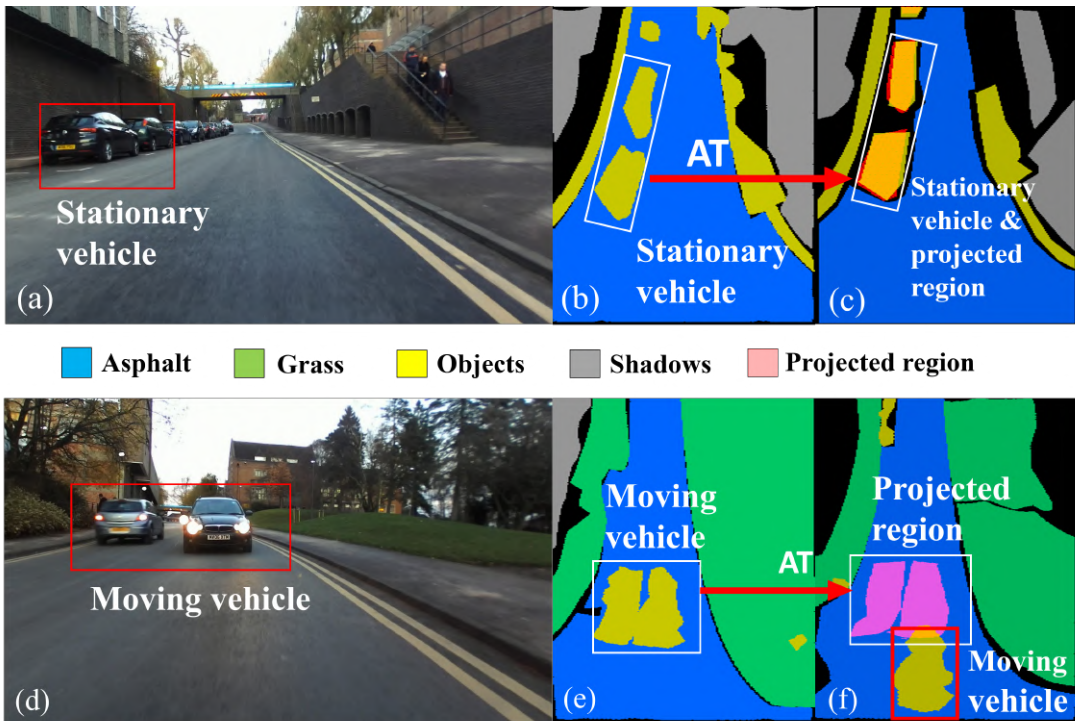


Fig. 6.14 (a) Optical imagery of (b); (b) Manually labeled CF with stationary vehicles; (c) Manually labeled PF with projected region; (d) Optical imagery of (e); (e) Manually labeled CF with moving vehicle; (f) Manually labeled PF with projected region.

In order to classify the moving and stationary objects, we need to determine the characteristic overlaps for them, and this is calculated by the ratio of overlap between the projected region and the manually labeled region in PFs as:

$$OL_{PFI} = \frac{P_i^{ml}}{P_i^{pr}} \quad (6.12)$$

where  $P_i^{pr}$  is the number of pixels of the projected region, and  $P_i^{ml}$  is the number of pixels of manually labeled object class in the projected region. The overlap ratio of moving and stationary objects in consecutive PFs are estimated using the manually labeled training dataset and are plotted as red and blue lines in Fig. 6.15. As expected, the overlap ratio of moving objects approaches zero, and the overlap ratio of stationary objects is higher over PFs. The decreased trend of stationary overlap ratio is due to two effects, the first being the position offset error introduced in the image registration process and the second being the various cross-range resolution over ranges that changes

the number of radar cells occupied by the specific object in different ranges. In principle, MTI can be achieved based on the differences in overlap ratios.

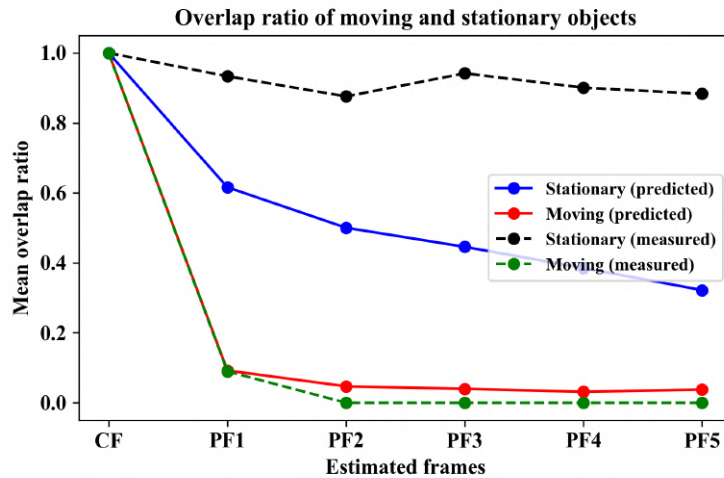


Fig. 6.15 The estimated and measured overlap ratios of moving and stationary objects over CF and PFs.

One discussion regarding the gap between predicted and measured values of stationary objects needs to be stressed here. This gap is because the predicted values are the average of various conditions which take into account the objects that are difficult to be projected using geometric transformation. E.g. the signpost in the cornering scenarios is difficult to track due to the small size. However, the presented example of measured overlap ratio is close to the ideal case (approaches to 1) as it is obtained by tracking a big vehicle target when the host vehicle is driving straightforwardly (the scenario will be discussed in the following in Fig. 6.16). This gap has no effect on the binary classification problem to distinguish moving and stationary objects. According to the method discussed below, the under-estimated stationary object can be correctly classified as stationary since it has a similar feature to "Stationary (predicted)" than "Moving (predicted)".

In the next, we will use a test dataset for the automatic assessment of overlaps and evaluate the similarity between estimated and measured overlaps. The classification of moving and stationary objects is achieved by comparing the measured overlap

ratio, which is obtained from consecutive segmented radar maps, and the estimated overlap ratios of  $OL_{mov} = [OL_{PF1}^{mov}, \dots, OL_{PFn}^{mov}]$  and  $OL_{sta} = [OL_{PF1}^{sta}, \dots, OL_{PFn}^{sta}]$ , which are obtained from manually labeled radar maps.

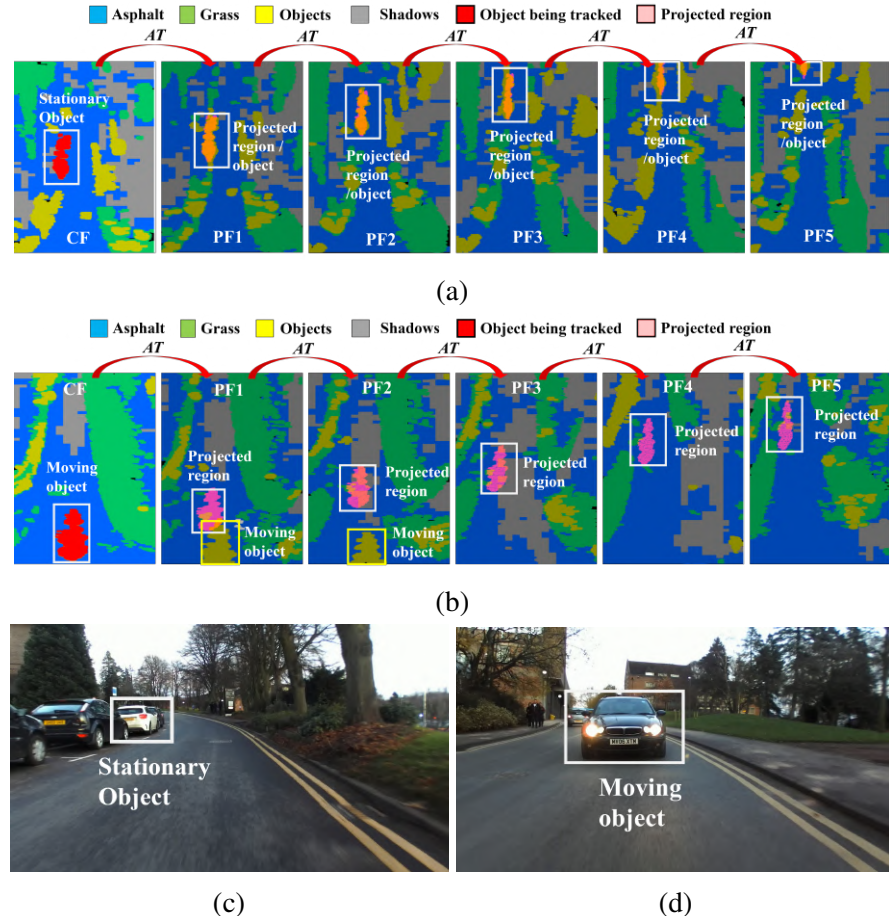


Fig. 6.16 (a) The projected regions utilized for the overlap ratio estimation of the stationary object. (b) The projected regions utilized for the overlap ratio estimation of moving objects. (c) The optical imagery of (a). (d) The optical imagery of (b).

Fig. 6.16 shows the snapshots of consecutive segmented radar frames with both moving and stationary objects. The object being tracked in the CF is labeled as solid red, and the projected regions are highlighted by a pink semi-transparent mask in the PFs. The projected region of the stationary object is consistent with the segmented stationary object as shown in Fig. 6.16(a), and the projected region in Fig. 6.16(b) displaces with the moving vehicle.

For each object being tracked, the measured overlap ratios between projected regions and segmented objects can be obtained as  $OL^{meas} = [OL_{PF1}^{meas}, \dots, OL_{PFn}^{meas}]$ , where  $n$  is the number of PFs utilized for estimating overlap ratios and each item can be calculated as:

$$OL_{PFi}^{meas} = \frac{P_i^{seg}}{P_i^{pr}} \quad (6.13)$$

Here  $P_i^{meas}$  is the number of pixels segmented as object in the projected region. Therefore, discrimination of moving and stationary object can be achieved by calculating the similarity between measured and estimated overlap ratios as follows:

$$Si_{mov} = \frac{1}{\sqrt{(OL^{meas} - OL_{mov})^2}}, Si_{sta} = \frac{1}{\sqrt{(OL^{meas} - OL_{sta})^2}} \quad (6.14)$$

where  $Si_{mov}$  and  $Si_{sta}$  are the overlap similarities of moving and stationary objects respectively. The class with a higher similarity value is indicated as the object class. The examples of  $OL^{meas}$  obtained from stationary and moving objects are plotted as dashed black and green lines in Fig. 6.15 to compare with the estimated values.

We would like to stress here that the number of considered PFs depends on the vehicle speed and frame rate. For the lowest urban speed of 5 m/s, detection range of 25 m, and frame rate of 1 f/s, we consider 3 frames as the lowest estimation and 5 frames as the highest estimation here.

### 6.4.3 Segmentation Promotion based on F2FA

The confidence of segmentation results may be improved by context-based information obtained from the F2FA process. F2FA is utilized to aid in determining the “unknown” class regions produced in single-frame segmentation. The block diagram of this procedure is presented in Fig. 6.17. The “unknown area” is the sloping grass area shown in the ground truth optical imagery, as the feature approaches both objects and grass. For each region assigned as “unknown” in the single frame segmentation, the region

is projected back into PFs. The overlap ratios of the projected region are calculated using a similar method to Eq. 6.13, and are represented as  $[r_a^i, r_g^i, r_o^i]^{i=1,\dots,5}$  in Fig. 6.17. Here the subscripts of  $a, g, o$  here represent the classes of asphalt, grass and objects, and the superscripts of  $i = 1, \dots, 5$  represent the number of PFs under tracked from 1 to 5. This is the information contributed by PFs to identify the ‘unknown’. Additionally, the contribution from CF is represented as  $r^0 = [r_a^0, r_g^0, r_o^0]$  in Fig. 6.17, which is obtained by assigning the area class with the highest possibility of MGD classifier [126] as “1” and the other areas as “0”. Both information contributed from CF and PFs are weighted equally for calculating the overall overlap ratio:  $[r_a, r_g, r_o] = \sum_{i=0}^5 [r_a^i, r_g^i, r_o^i]$ . The “unknown” area is identified as the area class with the biggest overlap.

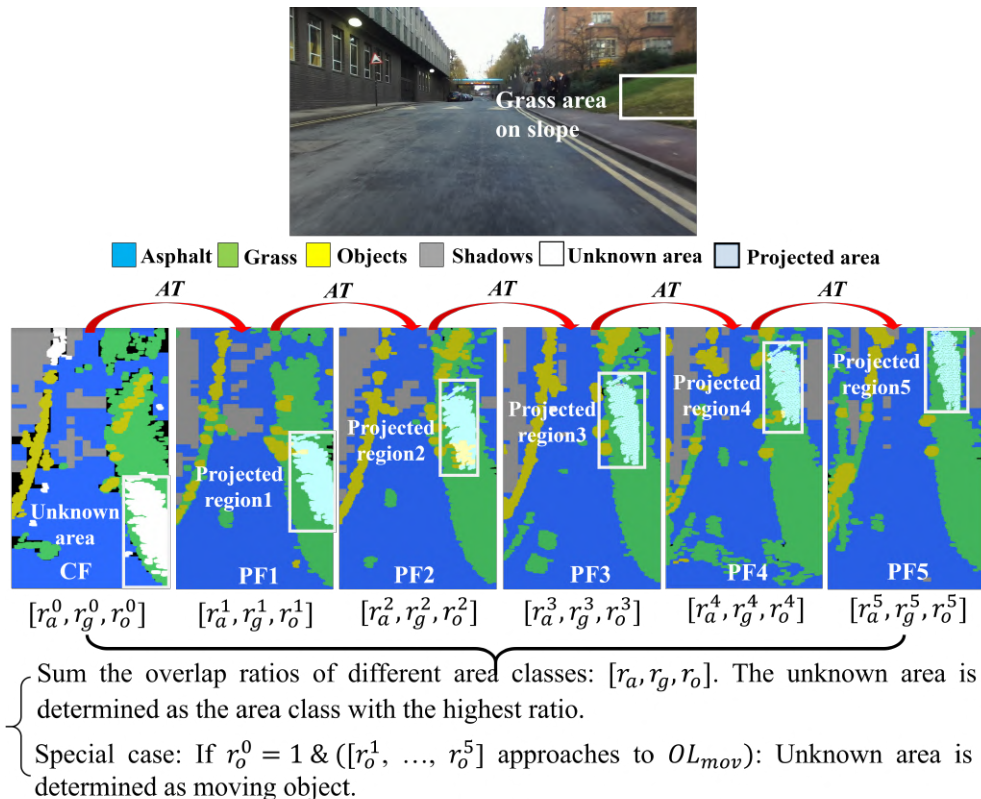


Fig. 6.17 The block diagram of improving segmentation performance by determining the “unknown area” based on F2FA and the corresponding optical imagery.

We would like to stress here that only the segmentation of stationary regions can be improved using F2FA. The moving objects are considered as the special case in this

stage as context-based information is meaningless to objects with changing positions. For the “unknown area” whose CF information is  $r^0 = [0, 0, 1]$  and the overlap ratio approaches to the estimated overlap ratio of  $OL_{moving}$ , they are determined as moving objects which is similar to the procedure stated in Section 6.4.2.

## 6.5 Results of the End-to-end Segmentation

In this section, we discuss the segmentation results obtained from the end-to-end segmentation algorithm. Both results of the end-to-end segmentation before and after MTI are analyzed and compared based on the ground truth optical imagery of the scene.

### 6.5.1 Improvement of Segmentation Performance after using the End-to-end Segmentation Algorithm.

Let us compare the Jaccard similarity coefficients (JSCs) of segmentation results obtained from the end-to-end segmentation discussed in this study, and the algorithm proposed in [126] to see the improvements. Both JSCs of segmentation results are given in Table 6.3. The definition of JSC estimation has been given in our previous publication [126] as:

$$JSC = \frac{A_{fs} \cap A_{label}}{A_{label}} \quad (6.15)$$

Here,  $A_{fs}$  is the number of correctly classified pixels overlapping with the labeled data regions of that class, and  $A_{label}$  is the total number of pixels of the corresponding class in the labeled data. As shown in Table 6.3, the JSC estimation of grass and objects has been significantly improved after the implementation of the E2E segmentation.

After understanding the improvement on performance mathematically, let us compare the segmentation results obtained from the two methods visually.

Table 6.3 Comparison between previously published JSCs and the updated JSCs of the E2E

Classes	Asphalt	Grass	Shadows	Objects
JSC in [126]	0.81	0.64	0.79	0.64
JSC of E2E	0.82	0.85	0.80	0.84

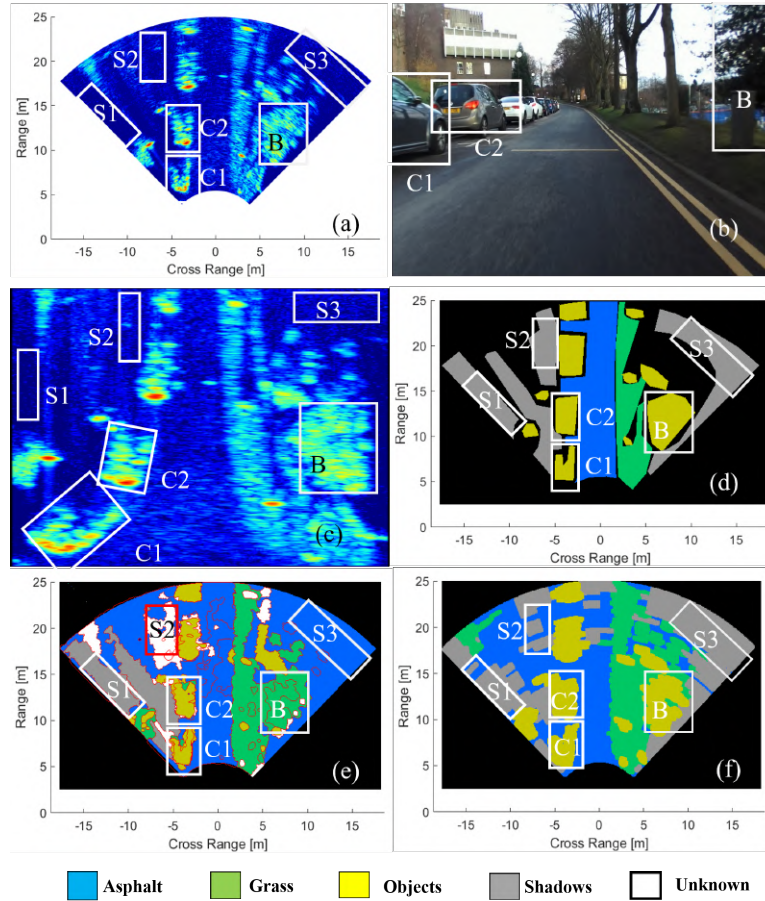


Fig. 6.18 First example of segmentation result of the end-to-end segmentation algorithm and comparison with the previous method in Chapter 5. (a) is the PPI radar map; (b) is the corresponding optical imagery. (c) is the input B-scope radar map; (d) is the manually labeled map; (e) is the segmented PPI map obtained from the method in Chapter 5; (f) is the segmented PPI map obtained by the end-to-end segmentation.

Two frames of segmented radar map obtained from the end-to-end segmentation and algorithm in [126] are presented in Fig. 6.18 and 6.19, respectively. The end-to-end segmentation is with the input of B-scope radar maps (as presented in Figs. 6.18(c) and 6.19(c)) and output of segmented B-scope radar maps which can improve the procedure of coordinate transformation as discussed in Section 6.2.1. To allow better visualization

and to compare with the previous segmentation results on PPI maps [126] (shown in Figs. 6.18(e) and 6.19(e)), the B-scope maps are transformed into PPI maps as presented in Figs. 6.18(f) and 6.19(f).

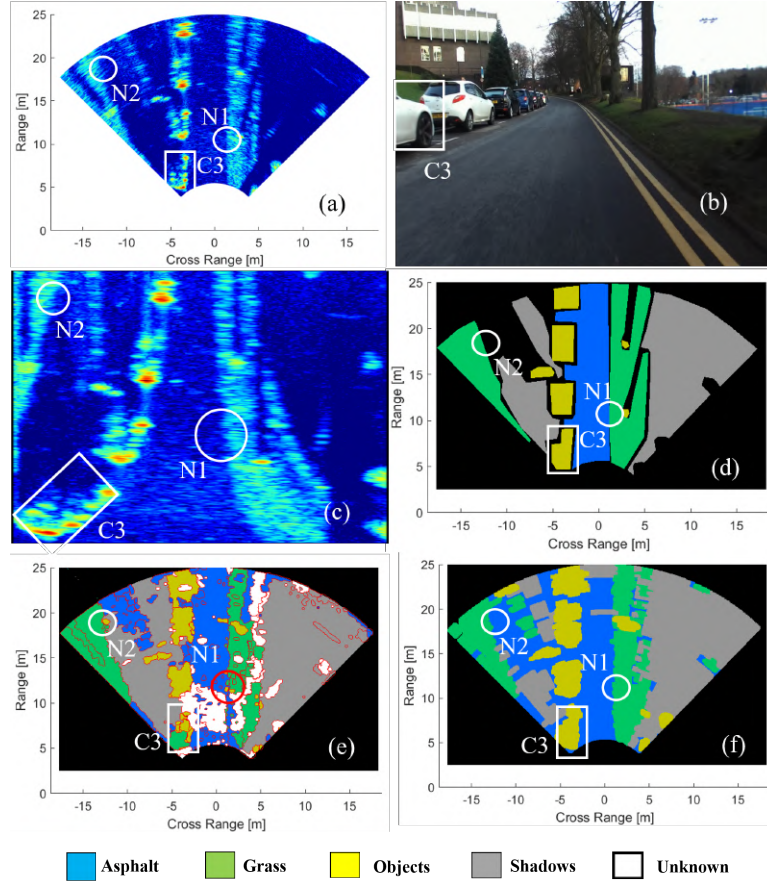


Fig. 6.19 Second example of segmentation results. (The caption representations are the same as Fig. 6.18).

White boxes in Figs. 6.18 and 6.19 show areas of visible improvement. Over-segmentation has been reduced by using two-step segmentation. E.g. the over-segmentation produced on object area might involve the confused grass area as shown in instances of C1 and C2 in Fig. 6.18(e) and C3 in Fig. 6.19(e). It has been improved in the results shown in Fig. 6.18(f) and Fig. 6.19(f) which are produced by the end-to-end segmentation. The ghost object areas of N1 and N2 in Fig. 6.19(e), which is produced by over-segmentation, have been improved. Additionally, the bush area of B is correctly

identified as objects in Fig. 6.18(f), which has been confused with the grass area in Fig. 6.18(e).

A more robust classification of shadows has been achieved after using the threshold sliding window to segment the remaining background in the second step of segmentation. For example, the shadow area of S3 in Fig. 6.18(f) has been properly separated in the end-to-end segmentation result, but wrongly classified as asphalt in the segmentation result shown in Fig. 6.18(e). This can be explained as: the areas of shadows and asphalt which have low contrast cannot be easily segmented by WT. The utilization of sliding windows has addressed this problem properly. The F2FA in the end-to-end segmentation algorithm has significantly improved the segmentation results that most of the “unknown areas” have been correctly identified in Fig. 6.18(f) and Fig. 6.19(f).

### 6.5.2 Analysis on the Results after MTI based on F2FA.

Here, we would like to discuss the MTI results by tracking the moving and stationary objects in six consecutive frames as shown in Fig. 6.20. All the sub-figures in the following discussion indicate Fig. 6.20 without special emphasis. Here, (a1)-(a6) are the ground truth optical imagery, (b1)-(b6) are the radar PPI radar maps, and (c1)-(c6) are the segmented PPI maps after MTI. The timeline of consecutive frames is from F6 to F1 that F1 in the first column is the last frame and all other frames with larger frame numbers can be considered as PFs which serve the MTI of F1.

The stationary objects we tracked in these six frames include region A which is the combined area of signposts and bushes, region C which is parking vehicles, and region  $O_1$  and  $O_2$  which are the signposts.

Let us see the trajectory of region A from (c1) to (c6): The stationary objects in region A are correctly classified as stationary targets in (c1)-(c3), but blocked by the moving vehicle of region D in (c4) in the radar detection. In (c5) and (c6), region A is not considered for MTI since the area at this longer range has out of our tracking

scope. Then, for the trajectory of object C, it has been correctly classified as stationary in (c4)-(c6) but confused as moving ones in (c2). This can also be explained as it has been blocked by a moving vehicle (region D) in (c3), and this will deliver the wrong information to the frames after (c2). The signposts of  $O_1$  and  $O_2$  are miss classified as moving which are super difficult to be tracked in image registration with such small physical size in radar maps, especially when the host vehicle is cornering.

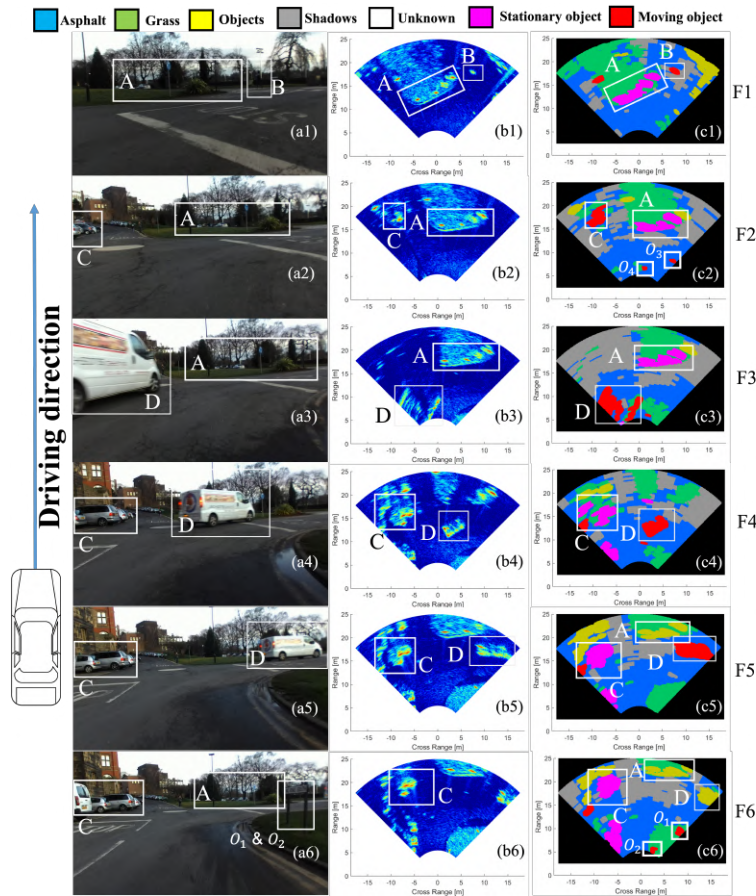


Fig. 6.20 The segmentation results after the implementation of MTI based on F2FA.

The moving objects that showed up in the six estimated frames include the moving pedestrian of region B and the moving vehicle of region D. Both have been correctly classified in consecutive frames from (c1) to (c5). Object D in (c6) is out of tracking scope again at this long range.

Additionally, the ghost moving objects of  $O_3$  and  $O_4$  are produced due to the over-segmentation in single frame segmentation of (c2).

Therefore, we could draw the following conclusions. Most of the objects can be correctly identified as moving or stationary in the MTI based on F2FA. The reasons for the confusion in MTI can be summarized as follow: 1) the confusion produced in image registration. This especially happened on objects with small area sizes and when the vehicle is cornering. It can be improved by conducting the region projection using real-time driving information and GPS position; 2) the confusion produced in single frame segmentation. This can be improved by reducing the over- and under-segmentation in the single frame segmentation; 3) the confusion caused by the showed-up moving targets. This might be improved by extending the detection range of radar maps, which can help involve more frames to mitigate the random error in MTI.

## 6.6 Conclusions

In this Chapter, we proposed the end-to-end segmentation on the automotive radar map, which is the extension work of in Chapter 5. The utilization of B-scope radar maps has simplified the complicated coordinate transformation procedure between ‘rixels’ of the PPI map and ‘cells’ of radar data, and has reduced the confusion due to unambiguous correspondence between radar cells and pixels. The noise floor hitting ranges of various areas are estimated to give reasonable range limitations for the implementation of image segmentation. The region classification procedure has been developed as a two-step segmentation which is robust and user parameter free. F2FA is proposed to achieve MTI and determination of the ‘unknown areas’ to improve the segmentation confidence.

The segmentation performance has been significantly improved by using the end-to-end segmentation. The JSC results of the end-to-end segmentation are estimated and compared with previously published JSC values in Chapter 5. The JSCs of areas of grass and objects are improved by more than 0.2 (from 0.64 to 0.84). The segmentation results obtained by MTI based on F2FA are evaluated based on six consecutive segmented frames. The reasons for the confusion in MTI based on F2FA are given as well to

understand the future work in this field: 1) continue working on improving the single frame segmentation performance; 2) collect location and real-time driving information of the host vehicle to improve the procedure of image registration in F2FA.

# Chapter 7

## Contributions of Part II

In Part II, the end-to-end (E2E) segmentation algorithm for high-resolution radar imagery is developed based on four main blocks: 1) feature extraction for each class of road actor/surface by assessing the statistical distribution parameters; 2) region classification based on the multi-variate Gaussian Distribution (MGD) classifier; 3) hybrid segmentation algorithm combined with pre-segmentation and region classification. 4) MTI using frame-to-frame association. Specific contributions related to each block are:

- 1) Feature extraction using statistical distributions parameters:

Contrary to traditional radar processing in which clutter is considered as an unwanted return, we consider an arbitrary radar image as the clutter map, where the contrast between power returns is defined by the physical nature of surfaces or objects within the scene, represented by different clusters of distribution parameters. It has been shown that while different specific PDFs can adequately describe returns from different classes, one distribution can be used to highlight the contrast between different classes and therefore be used to segment regions of different physical nature.

Indeed, various statistical distributions are widely used for estimating the features of radar returns such as Weibull, Rayleigh, and Rice distributions. However, instead of focusing on finding the best fit for each class, our study looked at finding the one providing the highest contrast among classes. The contrast between distribution feature

---

parameters is for the first time being considered as the input feature for achieving the region classification on automotive radar images.

2) Region classification based on the MGD classifier:

MGD is an algorithm used in unsupervised anomaly detection in machine learning. In this study, this algorithm has been adopted in a totally new application field for achieving the region classification of the radar image. The region classification is achieved based on the extracted feature parameters and the proposed novel MGD classifier with high accuracy performance.

3) The hybrid segmentation algorithm combined with pre-segmentation and region classification:

The hybrid segmentation method is developed in the remote sensing field for segmenting SAR imagery before. The traditional image processing methods cooperating with the proposed MGD classifier make the hybrid segmentation algorithm to be utilized in the new field of automotive image segmentation. The novel full scene E2E segmentation framework is developed on automotive radar images with accurate segmentation performance.

4) MTI using frame-to-frame association:

The typical method for achieving MTI is by tracking moving objects using Doppler information. However, this part of research considers the feature of the percentage of the overlap region between consecutive frames for classifying the moving and stationary objects. The image registration approach of affine transformation is utilized for mapping the corresponding regions between frames. The overlap percentage feature of objects is calculated based on the segmentation results of individual frames. This method provides an alternative solution for MTI, which fits the application scenario when Doppler information is not available in the specific high-resolution radar image data.

# **Chapter 8**

## **Future Work**

In this thesis, two parts of research toward the development of high-resolution automotive imaging radar are conducted: transmissivity of Low-THz signal through vehicle infrastructure, and full scene segmentation on automotive radar imagery. The conclusions have already been stated in the corresponding chapters, and the novelties have been outlined in the contributions for each part. Here, we would like to discuss the future works which are important for further development.

While transmissivity of vehicle infrastructures is well understood and modelled, reflectivity is also the key property that needs to be learned due to the following reasons: 1) Reflectivity from the vehicle infrastructures can increase the phase noise level of the receiver. 2) Scattering and the multiple reflections between the radar and the vehicle components may lead to an incorrect estimation of the direction of arrival of the return signal from a target. Chapter 2 shows the theoretical modeling of reflectivity of automotive bumpers and headlight covers in Sections 2.2.3 and 2.2.4, which are obtained based on the measured complex permittivity values of substrate materials of vehicle components and various automotive paints. However, the experimental verification of reflectivity has not been studied yet due to the limitation of the experimental setup. Further experimental measurement needs to be conducted to understand the influence of reflectivity on the performance of automotive radar systems.

In Part II, for the first time, the end-to-end segmentation on automotive radar imagery has been developed, which is a robust automatic method to achieve the full scene segmentation with the classification of road actors. Additionally, we achieved the effectively MTI based on frame-to-frame association of consecutive radar frames. The further challenges that need to be addressed are as follows.

- The performance of single frame segmentation needs to be improved, which depends on the results of pre-segmentation obtained from the image processing methods, as well as the performance of region classification. The pre-segmentation has been explored using methods of watershed transformation and Canny-edge detection in this thesis. However, the produced over- and under-segmented regions still need to be improved by involving promoted methods to obtain better segmentation results.
- The input features for region classification are currently statistical feature parameters of Weibull distribution obtained from both uncalibrated and calibrated radar data. The performance of region classification can be improved by increasing the number of features, such as involving parameters of other distributions and phase information of the radar data.

The objects class considered currently is a general class which includes all types of obstacles contained by the driving scene, such as buildings, vehicles, pedestrians, and signposts. The promoted classification strategy needs to be developed to identify different types of objects and to give better classification performance.

- The MTI of the automotive radar map is implemented based on the frame-to-frame association approach, which achieves region tracking between consecutive frames using image registration approach. For future work, utilizing the real-time driving information provided by IMU systems as well as the precise position

information given by the GPS systems are considered to be the straightforward way to complete the MTI without any human intervention.

- The proposed image segmentation algorithm is implemented and validated based on the dataset collected by the mechanical steered FMCW radar. The universality of the segmentation framework needs to be estimated in the future by implementing on the various high-resolution automotive radar maps produced by different beamforming strategies, such as the MIMO Doppler beam sharpening (DBS) maps.

# References

- [1] H. H. Meinel, “Evolving automotive radar — from the very beginnings into the future,” in *The 8th European Conference on Antennas and Propagation (EuCAP 2014)*, pp. 3107–3114, 2014.
- [2] C. Waldschmidt, J. Hasch, and W. Menzel, “Automotive radar—from first efforts to future systems,” *IEEE Journal of Microwaves*, vol. 1, no. 1, pp. 135–148, 2021.
- [3] S. M. Patole, M. Torlak, D. Wang, and M. Ali, “Automotive radars: A review of signal processing techniques,” *IEEE Signal Processing Magazine*, vol. 34, no. 2, pp. 22–35, 2017.
- [4] “Texas instruments application report.” [https://www.ti.com/lit/an/swra554a/swra554a.pdf?ts=1648398259176&ref\\_url](https://www.ti.com/lit/an/swra554a/swra554a.pdf?ts=1648398259176&ref_url).
- [5] F. Pfeiffer and E. M. Biebl, “Inductive compensation of high-permittivity coatings on automobile long-range radar radomes,” *IEEE transactions on microwave theory and techniques*, vol. 57, no. 11, pp. 2627–2632, 2009.
- [6] E. Emilsson, “Radar transparency and paint compatibility-a study of automobile bumper and bumper-skin complex permittivities for 77ghz microwaves,” Master’s thesis, 2017.
- [7] J. Eaves and E. Reedy, *Principles of modern radar*. Springer Science & Business Media, 2012.
- [8] M. A. Richards, J. Scheer, W. A. Holm, and W. L. Melvin, “Principles of modern radar,” 2010.

- [9] W. J. Fleming, “New automotive sensors—a review,” *IEEE Sensors Journal*, vol. 8, no. 11, pp. 1900–1921, 2008.
- [10] I. Ohya, A. Kosaka, and A. Kak, “Vision-based navigation by a mobile robot with obstacle avoidance using single-camera vision and ultrasonic sensing,” *IEEE transactions on robotics and automation*, vol. 14, no. 6, pp. 969–978, 1998.
- [11] M. Jaboyedoff, T. Oppikofer, A. Abellán, M.-H. Derron, A. Loyer, R. Metzger, and A. Pedrazzini, “Use of lidar in landslide investigations: a review,” *Natural hazards*, vol. 61, no. 1, pp. 5–28, 2012.
- [12] Y. Xiao, F. Norouzian, E. G. Hoare, E. Marchetti, M. Gashinova, and M. Chernikov, “Modeling and experiment verification of transmissivity of low-thz radar signal through vehicle infrastructure,” *IEEE Sensors Journal*, vol. 20, no. 15, pp. 8483–8496, 2020.
- [13] A. Merlo, “Automotive radar for the prevention of collisions,” *IEEE Transactions on Industrial Electronics and Control Instrumentation*, no. 1, pp. 1–6, 1964.
- [14] W. Harokopus, “Application of radar to automobile control and sensing,” in *1971 IEEE GMTT International Microwave Symposium Digest*, pp. 168–169, IEEE, 1971.
- [15] J. E. Stevens and L. L. Nagy, “A diplex doppler radar automotive obstacle detection system,” in *23rd IEEE Vehicular Technology Conference*, vol. 23, pp. 70–81, IEEE, 1972.
- [16] J. E. Stevens and L. L. Nagy, “Diplex doppler radar for automotive obstacle detection,” *IEEE Transactions on Vehicular Technology*, vol. 23, no. 2, pp. 34–44, 1974.
- [17] J. C. Reed, “Side zone automotive radar criteria for target classification,” in *Proceedings of the Intelligent Vehicles' 95. Symposium*, pp. 361–363, IEEE, 1995.

- [18] J. Woll, “Monopulse doppler radar for vehicle applications,” in *Proceedings of the Intelligent Vehicles '95. Symposium*, pp. 42–47, 1995.
- [19] M. Schneider, “Automotive radar-status and trends,” in *German microwave conference*, pp. 144–147, 2005.
- [20] R. Schneider, H.-L. Blocher, and K. M. Strohm, “Kokon-automotive high frequency technology at 77/79 ghz,” in *2007 European Microwave Conference*, pp. 1526–1529, IEEE, 2007.
- [21] W. J. Fleming, “New automotive sensors—a review,” *IEEE Sensors Journal*, vol. 8, no. 11, pp. 1900–1921, 2008.
- [22] M. Goppelt, H.-L. Blöcher, and W. Menzel, “Automotive radar—investigation of mutual interference mechanisms,” *Advances in Radio Science*, vol. 8, no. B. 3, pp. 55–60, 2010.
- [23] W. Menzel and A. Moebius, “Antenna concepts for millimeter-wave automotive radar sensors,” *Proceedings of the IEEE*, vol. 100, no. 7, pp. 2372–2379, 2012.
- [24] M. Gashinova, E. Hoare, and A. Stove, “Predicted sensitivity of a 300ghz fmcw radar to pedestrians,” in *2016 46th European Microwave Conference (EuMC)*, pp. 1497–1500, IEEE, 2016.
- [25] D. Jasteh, E. G. Hoare, M. Cherniakov, and M. Gashinova, “Experimental low-terahertz radar image analysis for automotive terrain sensing,” *IEEE Geoscience and Remote Sensing Letters*, vol. 13, no. 4, pp. 490–494, 2016.
- [26] F. Norouzian, R. Du, E. G. Hoare, P. Gardner, C. Constantinou, M. Cherniakov, and M. Gashinova, “Low-thz transmission through water-containing contaminants on antenna radome,” *IEEE Transactions on Terahertz Science and Technology*, vol. 8, no. 1, pp. 63–75, 2017.
- [27] K. Konstantinidis, A. P. Feresidis, C. C. Constantinou, E. Hoare, M. Gashinova, M. J. Lancaster, and P. Gardner, “Low-thz dielectric lens antenna with integrated

- waveguide feed,” *IEEE transactions on Terahertz Science and Technology*, vol. 7, no. 5, pp. 572–581, 2017.
- [28] D. R. Vizard, E. Hoare, M. Gashinova, and M. Cherniakov, “Applications of low thz frequency extenders for vector network analyzers,” in *2018 IEEE Radio and Antenna Days of the Indian Ocean (RADIO)*, pp. 1–2, IEEE, 2018.
- [29] D. R. Vizard, E. Hoare, M. Gashinova, and M. Cherniakov, “A novel 670 ghz hybrid frequency extender for portable automotive radar applications,” in *2017 18th International Radar Symposium (IRS)*, pp. 1–5, IEEE, 2017.
- [30] L. Daniel, A. Stove, E. Hoare, D. Phippen, M. Cherniakov, B. Mulgrew, and M. Gashinova, “Application of doppler beam sharpening for azimuth refinement in prospective low-thz automotive radars,” *IET Radar, Sonar & Navigation*, vol. 12, no. 10, pp. 1121–1130, 2018.
- [31] Y. Xiao, F. Norouzian, E. Marchetti, S. Cassidy, E. Hoare, M. Cherniakov, and M. Gashinova, “Transmissivity through automotive bumpers at mm-wave and low-thz frequencies,” in *2019 20th International Radar Symposium (IRS)*, pp. 1–6, IEEE, 2019.
- [32] E. Marchetti, R. Du, B. Willetts, F. Norouzian, E. G. Hoare, T. Y. Tran, N. Clarke, M. Cherniakov, and M. Gashinova, “Radar cross-section of pedestrians in the low-thz band,” *IET Radar, Sonar & Navigation*, vol. 12, no. 10, pp. 1104–1113, 2018.
- [33] F. Norouzian, R. Du, E. Marchetti, M. Gashinova, E. Hoare, C. Constantinou, P. Gardner, and M. Cherniakov, “Transmission through uniform layer of ice at low-thz frequencies,” in *2017 European Radar Conference (EURAD)*, pp. 211–214, IEEE, 2017.
- [34] S. Sabery, F. Norouzian, P. Gardner, E. Hoare, M. Cherniakov, and M. Gashinova, “Signal reduction by tree leaves in low-thz automotive radar,” in *2018 48th European Microwave Conference (EuMC)*, pp. 1445–1448, IEEE, 2018.

- [35] R. Du, F. Norouzian, E. Marchetti, B. Willetts, M. Gashinova, and M. Cherniakov, “Characterisation of attenuation by sand in low-thz band,” in *2017 IEEE Radar Conference (RadarConf)*, pp. 0294–0297, IEEE, 2017.
- [36] F. Norouziari, E. Marchetti, E. Hoare, M. Gashinova, C. Constantinou, P. Gardner, and M. Cherniakov, “Low-thz wave snow attenuation,” in *2018 International Conference on Radar (RADAR)*, pp. 1–4, IEEE, 2018.
- [37] F. Norouzian, E. Marchetti, M. Gashinova, E. Hoare, C. Constantinou, P. Gardner, and M. Cherniakov, “Rain attenuation at millimeter wave and low-thz frequencies,” *IEEE Transactions on Antennas and Propagation*, vol. 68, no. 1, pp. 421–431, 2019.
- [38] J. Dickmann, N. Appenrodt, J. Klappstein, H.-L. Bloecher, M. Muntzinger, A. Sailer, M. Hahn, and C. Brenk, “Making bertha see even more: Radar contribution,” *IEEE Access*, vol. 3, pp. 1233–1247, 2015.
- [39] H.-L. Bloecher, A. Sailer, G. Rollmann, and J. Dickmann, “79 ghz uwb automotive short range radar—spectrum allocation and technology trends,” *Advances in Radio Science*, vol. 7, no. B. 3, pp. 61–65, 2009.
- [40] M. Köhler, J. Hasch, H. L. Blöcher, and L.-P. Schmidt, “Feasibility of automotive radar at frequencies beyond 100 ghz,” *International Journal of Microwave and Wireless Technologies*, vol. 5, no. 1, pp. 49–54, 2013.
- [41] F. Norouzian, E. Marchetti, E. Hoare, M. Gashinova, C. Constantinou, P. Gardner, and M. Cherniakov, “Experimental study on low-thz automotive radar signal attenuation during snowfall,” *IET Radar, Sonar & Navigation*, vol. 13, no. 9, pp. 1421–1427, 2019.
- [42] F. Norouzian, E. Hoare, E. Marchetti, M. Cherniakov, and M. Gashinova, “Next generation, low-thz automotive radar—the potential for frequencies above 100 ghz,” in *2019 20th International Radar Symposium (IRS)*, pp. 1–7, IEEE, 2019.

- [43] F. Fitzek, Z. Abou-Chahine, R. H. Rasshofer, and E. M. Biebl, “Automotive radome design-fishnet structure for 79 ghz,” in *German Microwave Conference Digest of Papers*, pp. 146–149, IEEE, 2010.
- [44] F. Fitzek and R. H. Rasshofer, “Automotive radome design-reflection reduction of stratified media,” *IEEE Antennas and Wireless Propagation Letters*, vol. 8, pp. 1076–1079, 2009.
- [45] F. Fitzek, R. H. Raßhofer, and E. M. Biebl, “Broadband matching of high-permittivity coatings with frequency selective surfaces,” in *2011 German Microwave Conference*, pp. 1–4, IEEE, 2011.
- [46] N. Chen, R. Gourova, O. Krasnov, and A. Yarovoy, “The influence of the water-covered dielectric radome on 77ghz automotive radar signals,” in *2017 European Radar Conference (EURAD)*, pp. 139–142, IEEE, 2017.
- [47] A. Melzer, A. Onic, F. Starzer, and M. Huemer, “Short-range leakage cancelation in fmcw radar transceivers using an artificial on-chip target,” *IEEE Journal of selected topics in signal processing*, vol. 9, no. 8, pp. 1650–1660, 2015.
- [48] C. Vasanelli, F. Bögelsack, and C. Waldschmidt, “Reducing the radar cross section of microstrip arrays using amc structures for the vehicle integration of automotive radars,” *IEEE Transactions on Antennas and Propagation*, vol. 66, no. 3, pp. 1456–1464, 2018.
- [49] M. Venkatesh and G. Raghavan, “An overview of dielectric properties measuring techniques,” *Canadian biosystems engineering*, vol. 47, no. 7, pp. 15–30, 2005.
- [50] T. Chang, X. Zhang, X. Zhang, and H.-L. Cui, “Accurate determination of dielectric permittivity of polymers from 75 ghz to 1.6 thz using both s-parameters and transmission spectroscopy,” *Applied optics*, vol. 56, no. 12, pp. 3287–3292, 2017.
- [51] T. Tosaka, K. Fujii, K. Fukunaga, and A. Kasamatsu, “Development of complex relative permittivity measurement system based on free-space in 220–330-ghz

- range,” *IEEE Transactions on Terahertz science and Technology*, vol. 5, no. 1, pp. 102–109, 2014.
- [52] M. Naftaly, N. Shoaib, D. Stokes, and N. M. Ridler, “Intercomparison of terahertz dielectric measurements using vector network analyzer and time-domain spectrometer,” *Journal of Infrared, Millimeter, and Terahertz Waves*, vol. 37, no. 7, pp. 691–702, 2016.
- [53] T. Chang, X. Zhang, C. Yang, Z. Sun, and H.-L. Cui, “Measurement of complex terahertz dielectric properties of polymers using an improved free-space technique,” *Measurement Science and Technology*, vol. 28, no. 4, p. 045002, 2017.
- [54] L. Daniel, D. Phippen, E. Hoare, M. Cherniakov, and M. Gashinova, “Image segmentation in real aperture low-thz radar images,” in *2019 20th International Radar Symposium (IRS)*, pp. 1–8, IEEE, 2019.
- [55] D. J. Kozakoff, *Analysis of radome-enclosed antennas*. Artech House, 2010.
- [56] M. N. Sadiku *et al.*, *Elements of electromagnetics*, vol. 428. Oxford university press New York, 2001.
- [57] Y.-S. Jin, G.-J. Kim, and S.-G. Jeon, “Terahertz dielectric properties of polymers,” *Journal of the Korean Physical Society*, vol. 49, no. 2, pp. 513–517, 2006.
- [58] M. Naftaly and R. E. Miles, “Terahertz time-domain spectroscopy for material characterization,” *Proceedings of the IEEE*, vol. 95, no. 8, pp. 1658–1665, 2007.
- [59] R. Piesiewicz, C. Jansen, S. Wietzke, D. Mittleman, M. Koch, and T. Kürner, “Properties of building and plastic materials in the thz range,” *International Journal of Infrared and Millimeter Waves*, vol. 28, no. 5, pp. 363–371, 2007.
- [60] M. Davoodi, S. Sapuan, D. Ahmad, A. Aidy, A. Khalina, and M. Jonoobi, “Concept selection of car bumper beam with developed hybrid bio-composite material,” *Materials & Design*, vol. 32, no. 10, pp. 4857–4865, 2011.

- [61] J. Marzbanrad, M. Alijanpour, and M. S. Kiasat, “Design and analysis of an automotive bumper beam in low-speed frontal crashes,” *Thin-walled structures*, vol. 47, no. 8-9, pp. 902–911, 2009.
- [62] “Radar Transparency and Paint Compatibility.” <https://www.diva-portal.org/smash/get/diva2:1136102/FULLTEXT01.pdf>.
- [63] T. D. Dorney, R. G. Baraniuk, and D. M. Mittleman, “Material parameter estimation with terahertz time-domain spectroscopy,” *JOSA A*, vol. 18, no. 7, pp. 1562–1571, 2001.
- [64] L. Duvillaret, F. Garet, and J.-L. Coutaz, “A reliable method for extraction of material parameters in terahertz time-domain spectroscopy,” *IEEE Journal of selected topics in quantum electronics*, vol. 2, no. 3, pp. 739–746, 1996.
- [65] F. Norouzian, R. Du, M. Gashinova, E. Hoare, C. Constantinou, P. Gardner, and M. Cherniakov, “Monostatic and bistatic reflectivity measurements of radar absorbers at low-thz frequency,” in *2016 European Radar Conference (EuRAD)*, pp. 117–120, IEEE, 2016.
- [66] F. Norouzian, R. Du, M. Gashinova, E. Hoare, C. Constantinou, M. Lancaster, P. Gardner, and M. Cherniakov, “Signal reduction due to radome contamination in low-thz automotive radar,” in *2016 IEEE Radar Conference (RadarConf)*, pp. 1–4, IEEE, 2016.
- [67] “ELVA-1.” <http://www.elva-1.com>. Accessed: 2022-03-27.
- [68] J. Hammel, A. J. Gallant, and C. Balocco, “Free-space permittivity measurement at terahertz frequencies with a vector network analyzer,” *IEEE Transactions on Terahertz Science and Technology*, vol. 6, no. 6, pp. 817–823, 2016.
- [69] S. Krimi, J. Klier, J. Jonuscheit, G. von Freymann, R. Urbansky, and R. Beigang, “Highly accurate thickness measurement of multi-layered automotive paints using terahertz technology,” *Applied Physics Letters*, vol. 109, no. 2, p. 021105, 2016.

- [70] L.-F. Chen, C. Ong, C. Neo, V. Varadan, and V. K. Varadan, *Microwave electronics: measurement and materials characterization*. John Wiley & Sons, 2004.
- [71] Y. Dong, S. Lawman, Y. Zheng, D. Williams, J. Zhang, and Y.-C. Shen, “Nondestructive analysis of automotive paints with spectral domain optical coherence tomography,” *Applied optics*, vol. 55, no. 13, pp. 3695–3700, 2016.
- [72] I. Pupeza, R. Wilk, and M. Koch, “Highly accurate optical material parameter determination with thz time-domain spectroscopy,” *Optics express*, vol. 15, no. 7, pp. 4335–4350, 2007.
- [73] “TDS menlosystems.” <http://menlosystems.com/>. Accessed: 2021-10-24.
- [74] S. M. Sabery, A. Bystrov, M. Navarro-Cía, P. Gardner, and M. Gashinova, “Study of low terahertz radar signal backscattering for surface identification,” *Sensors*, vol. 21, no. 9, p. 2954, 2021.
- [75] B. B. S. Bandaranayake, *Terahertz time domain spectroscopy (THz-TDS) for solid state analysis*. The University of Iowa, 2016.
- [76] “TDS lytera.” <http://www.lytera.com/>. Accessed: 2021-10-24.
- [77] M. Scheller, C. Jansen, and M. Koch, “Analyzing sub-100- $\mu\text{m}$  samples with transmission terahertz time domain spectroscopy,” *Optics Communications*, vol. 282, no. 7, pp. 1304–1306, 2009.
- [78] “Keysight analyzers.” <https://www.keysight.com/nl/en/products/network-analyzers.html>. Accessed: 2021-10-25.
- [79] B. Scheuchl, D. Flett, R. Caves, and I. Cumming, “Potential of radarsat-2 data for operational sea ice monitoring,” *Canadian Journal of Remote Sensing*, vol. 30, no. 3, pp. 448–461, 2004.
- [80] N.-W. Park and K.-H. Chi, “Integration of multitemporal/polarization c-band sar data sets for land-cover classification,” *International Journal of Remote Sensing*, vol. 29, no. 16, pp. 4667–4688, 2008.

- [81] S. C. Steele-Dunne, H. McNairn, A. Monsivais-Huertero, J. Judge, P.-W. Liu, and K. Papathanassiou, “Radar remote sensing of agricultural canopies: A review,” *IEEE Journal of Selected Topics in Applied Earth Observations and Remote Sensing*, vol. 10, no. 5, pp. 2249–2273, 2017.
- [82] M. M. Trivedi and J. C. Bezdek, “Low-level segmentation of aerial images with fuzzy clustering,” *IEEE Transactions on Systems, Man, and Cybernetics*, vol. 16, no. 4, pp. 589–598, 1986.
- [83] R. Krishnapuram and J. M. Keller, “The possibilistic c-means algorithm: insights and recommendations,” *IEEE transactions on Fuzzy Systems*, vol. 4, no. 3, pp. 385–393, 1996.
- [84] H. Caillol, A. Hillion, and W. Pieczynski, “Fuzzy random fields and unsupervised image segmentation,” *IEEE transactions on geoscience and remote sensing*, vol. 31, no. 4, pp. 801–810, 1993.
- [85] J. Fan, M. Han, and J. Wang, “Single point iterative weighted fuzzy c-means clustering algorithm for remote sensing image segmentation,” *Pattern Recognition*, vol. 42, no. 11, pp. 2527–2540, 2009.
- [86] T. Zuva, O. O. Olugbara, S. O. Ojo, and S. M. Ngwira, “Image segmentation, available techniques, developments and open issues,” *Canadian Journal on Image Processing and Computer Vision*, vol. 2, no. 3, pp. 20–29, 2011.
- [87] P. Yu, A. K. Qin, and D. A. Clausi, “Unsupervised polarimetric sar image segmentation and classification using region growing with edge penalty,” *IEEE Transactions on Geoscience and Remote Sensing*, vol. 50, no. 4, pp. 1302–1317, 2011.
- [88] F. Cheevasuvit, H. Maitre, and D. Vidal-Madjar, “A robust method for picture segmentation based on a split-and-merge procedure,” *Computer vision, graphics, and image processing*, vol. 34, no. 3, pp. 268–281, 1986.

- [89] F. Galland, J.-M. Nicolas, H. Sportouche, M. Roche, F. Tupin, and P. Réfrégier, “Unsupervised synthetic aperture radar image segmentation using fisher distributions,” *IEEE Transactions on Geoscience and Remote Sensing*, vol. 47, no. 8, pp. 2966–2972, 2009.
- [90] J. Chen, M. Deng, X. Mei, T. Chen, Q. Shao, and L. Hong, “Optimal segmentation of a high-resolution remote-sensing image guided by area and boundary,” *International Journal of Remote Sensing*, vol. 35, no. 19, pp. 6914–6939, 2014.
- [91] M. D. Hossain and D. Chen, “Segmentation for object-based image analysis (obia): A review of algorithms and challenges from remote sensing perspective,” *ISPRS Journal of Photogrammetry and Remote Sensing*, vol. 150, pp. 115–134, 2019.
- [92] M. N. Kurnaz, Z. Dokur, and T. Ölmez, “Segmentation of remote-sensing images by incremental neural network,” *Pattern recognition letters*, vol. 26, no. 8, pp. 1096–1104, 2005.
- [93] P. Mitra, B. U. Shankar, and S. K. Pal, “Segmentation of multispectral remote sensing images using active support vector machines,” *Pattern recognition letters*, vol. 25, no. 9, pp. 1067–1074, 2004.
- [94] M. Siam, S. Elkerdawy, M. Jagersand, and S. Yogamani, “Deep semantic segmentation for automated driving: Taxonomy, roadmap and challenges,” in *2017 IEEE 20th international conference on intelligent transportation systems (ITSC)*, pp. 1–8, IEEE, 2017.
- [95] Y. Xiao, L. Daniel, and M. Gashinova, “Feature-based classification for image segmentation in automotive radar based on statistical distribution analysis,” in *2020 IEEE Radar Conference (RadarConf20)*, pp. 1–6, IEEE, 2020.
- [96] M. G. e. a. Yand Xiao, Scott Cassidy, “Universal image segmentation framework on high- resolution automotive radar map,” in *Radar 2022 IET*, IET, 2022.

- [97] “UoB automotive radar dataset.” <https://doi.org/10.25500/edata.bham.00000329>. Accessed: 2021-10-06.
- [98] F. T. Ulaby, D. G. Long, W. J. Blackwell, C. Elachi, A. K. Fung, C. Ruf, K. Sarabandi, H. A. Zebker, and J. Van Zyl, *Microwave radar and radiometric remote sensing*, vol. 4. University of Michigan Press Ann Arbor, 2014.
- [99] T. Kurita, N. Otsu, and N. Abdelmalek, “Maximum likelihood thresholding based on population mixture models,” *Pattern recognition*, vol. 25, no. 10, pp. 1231–1240, 1992.
- [100] F. E. Nathanson, J. P. Reilly, and M. N. Cohen, “Radar design principles-signal processing and the environment,” *NASA STI/Recon Technical Report A*, vol. 91, p. 46747, 1991.
- [101] A. K. Fung, “Microwave scattering and emission models and their applications,” *Norwood, MA: Artech House, 1994.*, 1994.
- [102] E. S. Li and K. Sarabandi, “Low grazing incidence millimeter-wave scattering models and measurements for various road surfaces,” *IEEE Transactions on Antennas and Propagation*, vol. 47, no. 5, pp. 851–861, 1999.
- [103] A. Geiger, M. Lauer, C. Wojek, C. Stiller, and R. Urtasun, “3d traffic scene understanding from movable platforms,” *IEEE transactions on pattern analysis and machine intelligence*, vol. 36, no. 5, pp. 1012–1025, 2013.
- [104] “LIBLABEL: Lightweight Semantic/Instance Annotation Tool.” <http://www.cvlabs.net/software/liblabel/>. Accessed: 2021-09-29.
- [105] M. Sekine, S. Ohtani, T. Musha, T. Irabu, E. Kiuchi, T. Hagisawa, and Y. Tomita, “Weibull-distributed ground clutter,” *IEEE Transactions on Aerospace and Electronic Systems*, no. 4, pp. 596–598, 1981.
- [106] R. Vicen-Bueno, M. Rosa-Zurera, M. Jarabo-Amores, and R. Gil-Pita, “Automatic target detection in simulated ground clutter (weibull distributed) by

- multilayer perceptrons in a low-resolution coherent radar,” *IET radar, sonar & navigation*, vol. 4, no. 2, pp. 315–328, 2010.
- [107] S. Matteoli, M. Diani, and J. Theiler, “An overview of background modeling for detection of targets and anomalies in hyperspectral remotely sensed imagery,” *IEEE Journal of Selected Topics in Applied Earth Observations and Remote Sensing*, vol. 7, no. 6, pp. 2317–2336, 2014.
- [108] M. Kampffmeyer, A.-B. Salberg, and R. Jenssen, “Semantic segmentation of small objects and modeling of uncertainty in urban remote sensing images using deep convolutional neural networks,” in *Proceedings of the IEEE conference on computer vision and pattern recognition workshops*, pp. 1–9, 2016.
- [109] J. Canny, “A computational approach to edge detection,” *IEEE Transactions on pattern analysis and machine intelligence*, no. 6, pp. 679–698, 1986.
- [110] A. Tremeau and N. Borel, “A region growing and merging algorithm to color segmentation,” *Pattern recognition*, vol. 30, no. 7, pp. 1191–1203, 1997.
- [111] G. Hamarneh and X. Li, “Watershed segmentation using prior shape and appearance knowledge,” *Image and Vision Computing*, vol. 27, no. 1-2, pp. 59–68, 2009.
- [112] Y. Dong, B. Forster, and A. Milne, “Comparison of radar image segmentation by gaussian-and gamma-markov random field models,” *International Journal of Remote Sensing*, vol. 24, no. 4, pp. 711–722, 2003.
- [113] G. Sheng, W. Yang, X. Deng, C. He, Y. Cao, and H. Sun, “Coastline detection in synthetic aperture radar (sar) images by integrating watershed transformation and controllable gradient vector flow (gvf) snake model,” *IEEE Journal of Oceanic Engineering*, vol. 37, no. 3, pp. 375–383, 2012.
- [114] T. B. Ijitona, J. Ren, and P. B. Hwang, “Sar sea ice image segmentation using watershed with intensity-based region merging,” in *2014 IEEE International Conference on Computer and Information Technology*, pp. 168–172, IEEE, 2014.

- [115] S. Niwattanakul, J. Singthongchai, E. Naenudorn, and S. Wanapu, “Using of jaccard coefficient for keywords similarity,” in *Proceedings of the international multiconference of engineers and computer scientists*, vol. 1, pp. 380–384, 2013.
- [116] D. Li, G. Zhang, Z. Wu, and L. Yi, “An edge embedded marker-based watershed algorithm for high spatial resolution remote sensing image segmentation,” *IEEE Transactions on Image Processing*, vol. 19, no. 10, pp. 2781–2787, 2010.
- [117] M. Ash, M. Ritchie, and K. Chetty, “On the application of digital moving target indication techniques to short-range fmcw radar data,” *IEEE Sensors Journal*, vol. 18, no. 10, pp. 4167–4175, 2018.
- [118] A. Macaveiu and A. Câmpeanu, “Automotive radar target tracking by kalman filtering,” in *2013 11th International Conference on Telecommunications in Modern Satellite, Cable and Broadcasting Services (TELSIKS)*, vol. 2, pp. 553–556, IEEE, 2013.
- [119] A. Eltrass and M. Khalil, “Automotive radar system for multiple-vehicle detection and tracking in urban environments,” *IET Intelligent Transport Systems*, vol. 12, no. 8, pp. 783–792, 2018.
- [120] R. Klemm, “Adaptive airborne mti: an auxiliary channel approach,” in *IEE Proceedings F (Communications, Radar and Signal Processing)*, vol. 134, pp. 269–276, IET, 1987.
- [121] A. F. Martone, K. Ranney, and C. Le, “Noncoherent approach for through-the-wall moving target indication,” *IEEE Transactions on Aerospace and Electronic Systems*, vol. 50, no. 1, pp. 193–206, 2014.
- [122] F. Adib, Z. Kabelac, D. Katabi, and R. C. Miller, “3d tracking via body radio reflections,” in *11th {USENIX} Symposium on Networked Systems Design and Implementation ({NSDI} 14)*, pp. 317–329, 2014.
- [123] A. Meta and P. Hoogeboom, “Signal processing algorithms for fmcw moving target indicator synthetic aperture radar,” in *Proceedings. 2005 IEEE Interna-*

- tional Geoscience and Remote Sensing Symposium, 2005. IGARSS'05.*, vol. 1, pp. 4–pp, IEEE, 2005.
- [124] M. Mallick and S. Arulampalam, “Comparison of nonlinear filtering algorithms in ground moving target indicator (gmti) tracking,” in *Signal and Data Processing of Small Targets 2003*, vol. 5204, pp. 630–647, International Society for Optics and Photonics, 2004.
- [125] R. Jinan and T. Raveendran, “Particle filters for multiple target tracking,” *Procedia Technology*, vol. 24, pp. 980–987, 2016.
- [126] Y. Xiao, L. Daniel, and M. Gashinova, “Image segmentation and region classification in automotive high-resolution radar imagery,” *IEEE Sensors Journal*, vol. 21, no. 5, pp. 6698–6711, 2020.
- [127] K. Sarabandi, E. S. Li, and A. Nashashibi, “Modeling and measurements of scattering from road surfaces at millimeter-wave frequencies,” *IEEE Transactions on Antennas and Propagation*, vol. 45, no. 11, pp. 1679–1688, 1997.
- [128] M. Series, “Systems characteristics of automotive radars operating in the frequency band 76–81 ghz for intelligent transport. systems applications,” *Recommendation ITU-R, M*, pp. 2057–1, 2018.
- [129] S. Murali, K. Subburaj, B. Ginsburg, and K. Ramasubramanian, “Interference detection in fmcw radar using a complex baseband oversampled receiver,” in *2018 IEEE Radar Conference (RadarConf18)*, pp. 1567–1572, IEEE, 2018.
- [130] H. Han and X. Han, “Application of morphology and otsu method in the canny edge detection operator,” *Microelectronics & Computer*, vol. 29, no. 2, pp. 146–149, 2012.
- [131] “INRAS dataset.” <http://www.inras.at/en/products/modular-radar-system.html>. Accessed: 2021-12-20.
- [132] M. G. e. a. Yand Xiao, Liam Daniel, “Automotive radar image segmentation with frame fusion,” in *Radar 2022 IET*, IET, 2022.

- [133] H. Lin, P. Du, W. Zhao, L. Zhang, and H. Sun, “Image registration based on corner detection and affine transformation,” in *2010 3rd International Congress on Image and Signal Processing*, vol. 5, pp. 2184–2188, IEEE, 2010.
- [134] D. G. Lowe, “Distinctive image features from scale-invariant keypoints,” *International journal of computer vision*, vol. 60, no. 2, pp. 91–110, 2004.